

MODELING, DESIGN AND OPTIMIZATION OF ELECTRODYNAMIC ZERO-NET MASS-
FLUX (ZNMFL) ACTUATORS

By

JANHAVI S. AGASHE

A DISSERTATION PRESENTED TO THE GRADUATE SCHOOL
OF THE UNIVERSITY OF FLORIDA IN PARTIAL FULFILLMENT
OF THE REQUIREMENTS FOR THE DEGREE OF
DOCTOR OF PHILOSOPHY

UNIVERSITY OF FLORIDA

2009

© 2009 Janhavi Agashe

To my parents Mr. S.H. Agashe and Mrs. Padmaja S. Agashe

ACKNOWLEDGEMENTS

This work was supported in part by NASA NRA # NNX07AD94A monitored by Dr. Brian Allan.

This work would not have been possible without constant guidance and input from my committee members – Dr. David P. Arnold, Dr. Louis N. Cattafesta, Dr. Mark Sheplak and Dr. Henry Zmuda. Their time and effort have not only made this work better but also made me an improved researcher.

The lessons of patience, attention to detail and perseverance that I have learnt from Dr. Arnold will serve me for a long time to come. His encouragement and motivation have helped me survive this emotional roller-coaster. I would like to thank Dr. Cattafesta for making me a very careful and meticulous experimentalist. As much I have hated repeating every experiment several times, I have learnt the value of cautiousness in taking and interpreting experimental data. Dr. Sheplak has taught me the importance of keeping the big picture always in sight without sacrificing the details. I have really enjoyed several non-academic discussions with him and I am going to miss them sorely. I also have to thank him for getting the espresso machine in the lab without which lot of long nights would have been impossible.

I would like to thank all my Interdisciplinary Microsystems Group (IMG) colleagues – past and present, who made the three and half years I spent here a lot of fun. I have learnt more from my interactions with my colleagues than any textbook or class could have taught me. I would like to extend my gratitude towards ex-IMG colleagues – Dr. Ryan Holman, Dr. David Martin, Dr. Karthik Kadirvel and Dr. Steven Horowitz who were there to hold my hand when I was starting out. My colleagues – Dr. Brian Homeijer, Matthew Williams, Benjamin Griffin, Brandon Bertolucci, Vijay Chandrasekharan, Christopher Bahr, Christopher Meyer, Matias Oyarzun, Justin Zito and Miguel Palavaccini – who have been sounding board for all my

research ideas. In addition, I would like to thank other colleagues who have become friends. Tailgating and talking football, summer barbeques would not have been the same without Drew Wetzel, Jessica Meloy, Jessica Sockwell, Erin Patrick, Alex Phipps and Jeremy Sells. I am glad that I started out in IMG with a lot of colleagues and coworkers but I am leaving with so many friends. I would like to also thank my friends Dr. Madhura Bandhyopadhyay and Ms. Ankita Datta for the fun time I have spent with them.

Lastly I would like to thank my family for their incessant and unconditional love and support for this long process. My parents Mr. Shrinivas Agashe and Mrs. Padmaja Agashe have always been there for me. They have taught me everything I know and given me every possible freedom and opportunity. I would not have been here without them. I would like to thank my sister Ms. Ashwini Agashe for always reminding me what the important things in life were. My father-in-law Dr. O.P. Katyal has always been a source of inspiration and his dedication to his work will always motivate me. My mother-in-law Mrs. Manju Katyal and my sisters-in-law Dr. Vasuda Bhatia and Mrs. Bhavana Katyal-Sarin have been extremely supportive and understanding through the years. I would also like to thank my cousin and brother-in-law Dr. Jayashree Mahajan and Dr. Asoo Vakharia. They have been my family here and I will always cherish the time spent with them and my nephews Rohan and Ajit. Last, but not the least, I thank my husband Dr. Vipul Katyal who has been my rock. He has stood by me through some of my most vulnerable moments and ensured that I have emerged out of them a better stronger person. I love him dearly and am looking forward to many happy years with him.

TABLE OF CONTENTS

	<u>page</u>
ACKNOWLEDGEMENTS.....	4
LIST OF TABLES.....	9
LIST OF FIGURES.....	11
ABSTRACT.....	16
CHAPTER	
1 INTRODUCTION.....	18
1.1 Background.....	19
1.2 Research Objectives.....	25
1.3 Thesis Outline.....	26
2 BACKGROUND.....	27
2.1 Transduction Mechanisms.....	27
2.2 Basics of Magnetic Transduction.....	32
2.2.1 Magnetic Field Generated by Current Distributions.....	33
2.2.2 Magnetic Field due to Intrinsic Material Properties.....	35
2.2.3 Equivalence between Current Distributions and Magnetic Materials.....	40
2.3 Magnetic Field Based Actuators.....	41
2.3.1 Fixed-Field Actuators (Electrodynamic).....	42
2.3.2 Variable-Field Actuators (Variable-Reluctance).....	44
2.4 Scaling of Magnetic Actuators.....	46
2.5 Magnetic Actuators.....	49
2.5.1 Reported Zero-Net Mass-Flux Actuators.....	50
2.5.2 Modeling of Zero-Net Mass-Flux Actuators.....	56
3 LUMPED ELEMENT MODELING.....	58
3.1 Lumped Element Modeling Basics.....	58
3.1.1 Passive Lumped Elements.....	59
3.1.2 Two-Port Elements.....	61
3.2 Lumped Element Model of Electrodynamic ZNMF Actuator.....	64
3.3 Electrodynamic Transduction.....	67
3.3.1 Calculation of the Transduction Coefficient using 1-D Magnetic Circuit Model.....	72
3.3.2 Calculation of the Transduction Coefficient using Finite Element Analysis.....	76
3.4 Diaphragm Model.....	79
3.4.1 Coupling between Mechanical and Acoustic Domains.....	79
3.4.2 Acoustic Model of the Diaphragm.....	81

3.5	Models of the Acoustic/Fluidic Components	84
3.5.1	Cavity Model	84
3.5.2	Orifice Model	85
3.5.3	Acoustic Radiation Impedance	87
3.6	Transfer Function for Electrodynamic ZNMF Actuator	89
4	FABRICATION AND MODEL VALIDATION OF PROTOTYPE ELECTRODYNAMIC ZNMF ACTUATORS	93
4.1	Speaker-Driven Electrodynamic ZNMF Actuator	93
4.1.1	Lumped Parameter Extraction	94
4.1.1.1	Electrical impedance (R_{ec} and L_{ec})	95
4.1.1.2	Mechanical compliance (C_{mD})	96
4.1.1.3	Electromechanical transduction coefficient (BL_{coil})	98
4.1.1.4	Diaphragm acoustic resistance (R_{aD}) and equivalent acoustic mass (M_{aD})	100
4.1.2	Hotwire Measurements – Overall Model Verification	105
4.2	Fabrication of Custom ZNMF Actuators	108
4.2.1	Magnetic Assembly	109
4.2.2	Diaphragm Assembly	111
4.3	Model Validation	114
4.3.1	Electrical Impedance Measurements	115
4.3.2	Static Displacement Tests	116
4.3.4	Hotwire Measurements	121
4.3.5	Summary	125
5	DESIGN AND OPTIMIZATION STRATEGIES FOR ELECTRODYNAMIC ZNMF ACTUATORS	127
5.1	Challenges in Design and Optimization of Electrodynamic ZNMF Actuators	127
5.2	Frequency Dependence of Actuator Performance	132
5.3	Design Tradeoffs for Composite Diaphragm Electrodynamic ZNMF Actuators	136
5.3.1	Magnetic Assembly Design Tradeoffs	136
5.3.2	Composite Diaphragm Design Tradeoffs	144
5.3.2.1	Effective area (S)	145
5.3.2.2	Acoustic compliance (C_{aD})	146
5.3.2.3	Acoustic mass (M_{aD})	148
5.3.2.4	Resonant frequency (f_{res})	149
5.3.3	System-level Design Tradeoffs	150
5.3.4	Power Considerations	153
5.4	Optimization of Composite Diaphragm Electrodynamic ZNMF Actuators	155
5.4.1	Choice of the Objective Function	158
5.4.2	Parameter Variation	164
5.5	Characterization of the Optimized Electrodynamic Actuator	165
6	SUMMARY AND FUTURE WORK	169

6.1 Summary.....	169
6.2 Suggested Future Work	171
APPENDIX	
A MAGNETIC CIRCUIT MODEL	173
A.1 Non-idealities in the Soft Magnet.....	176
A.2 Magnetic Assembly for the Optimized Actuator	178
A.3 Force Non-linearities	180
B DERIVATION OF LUMPED MODEL PARAMETERS OF A CLAMPED ANNULAR PLATE.....	182
C OPTIMIZATION DETAILS	186
LIST OF REFERENCES.....	188
BIOGRAPHICAL SKETCH	193

LIST OF TABLES

<u>Table</u>	<u>page</u>
2-1 Relative permeability of soft magnetic materials.....	39
2-2 Magnetic properties of hard magnet materials	40
2-3 Summary of ZNMF actuators reviewed.....	55
3-1 Effort and flow variables in various energy domains.....	60
3-2 Passive lumped element components in various energy domains.....	61
3-3 Dimensions of the magnetic assembly for 1-D circuit model and finite element modeling comparisons	77
3-4 Lumped parameters for electrodynamic ZNMF actuator.....	89
4-1 Geometrical parameters for speaker-driven ZNMF actuator	94
4-2 Linear curve fit results for compliance measurements.....	97
4-3 Linear curve fit results for transduction factor measurements	100
4-4 Extracted parameters for the speaker-driven ZNMF actuator.....	104
4-5 Diaphragm material properties and geometry	115
4-6 Model parameters for PDMS diaphragm corresponding to actuator A1.....	115
4-7 Electrical and magnetic parameters.....	118
4-8 PDMS diaphragm parameters for actuator A1	120
4-9 Device configuration for hotwire tests	121
4-10 Various components of the damping.....	124
5-1 Output velocity in different frequency ranges and desired actuator characteristics.....	135
5-2 Lower and upper bounds on the magnetic assembly design variables.....	141
5-3 Constants used in the optimization formulation.....	141
5-4 Optimized designs for maximum blocked force for various power constraints and no mass constraint (active constraints indicated in bold)	143
5-5 Diaphragm material properties and geometry	148

5-6	Parameters for the magnetic assembly	153
5-7	Lower and upper bounds on design variables	157
5-8	Baseline actuator and optimized designs for objective functions 1-3 (active constraints indicated in bold)	160
5-9	Optimized designs for objective function 1 (maximum integrated velocity) for various power constraints (active constraints indicated in bold).....	160
C-1	Optimized magnetic assembly designs for maximum blocked force for power constraint and mass constraint of 150 g.....	186
C-2	Optimized magnetic assembly designs for maximum blocked force for power constraint and mass constraint of 120 g.....	186
C-3	Optimized designs for objective function 1 with various weight constraints.....	187

LIST OF FIGURES

<u>Figure</u>	<u>page</u>
1-1 Actuation stress vs. actuation stress for various transduction mechanisms	22
1-2 Frequency dependence of performance of various transduction mechanisms	23
2-1 Two port model of a transducer.....	28
2-2 Free body diagram of the all the forces acting on an actuator.....	31
2-3 Operating characteristics of a typical actuator	32
2-4 Magnetic field generated by a current element	34
2-5 Magnetic field generated by a solenoidal coil.....	35
2-6 Soft magnetic material.....	38
2-7 Hard magnetic material	39
2-8 Hard magnet representation as an equivalent current density	41
2-9 Electrodynamics transduction	43
2-10 Typical mesoscale voice-coil actuator.....	44
2-11 Typical configuration of mesoscale solenoid actuator	45
2-12 Scaling of various magnetic interactions.....	46
2-13 Cross-section of a typical moving coil speaker.....	50
2-14 Integrated micromachined electrostatic ZNMF actuator adapter from Coe et al.....	51
2-15 Mesoscale piezoelectric ZNMF actuator adapted from Smith et al.	51
2-16 Fixed field (electrodynamics) ZNMF actuator adapted from McCormick.....	52
2-17 Integrated micromachined electrostatic ZNMF actuator demonstrated by Parviz et al.	53
2-18 FSMA based ZNMF actuator reported by Liang et al.....	53
2-19 On chip electrodynamic ZNMF actuator for cooling reported by Yong et al.	54
2-20 IPMC driven ZNMF actuator adapted from Lee et al.	54
3-1 Passive lumped element.....	60

3-2	Ideal transformer and gyrator two-port circuit elements	62
3-3	Impedance and source transformation using a transformer	63
3-4	Impedance and source transformations using a gyrator	64
3-5	Schematic of electrodynamic ZNMF actuator.....	64
3-6	Lumped element model of the electrodynamic ZNMF actuator	66
3-7	Lorentz force on a current carrying coil in a magnetic field	68
3-8	Voltage induced on a moving coil in a magnetic field.....	69
3-9	Two-port gyrator model of electrodynamic transduction.....	71
3-10	1-D magnetic circuit approach	72
3-11	Fringing fields in the air gap.....	74
3-12	Axissymmetric COMSOL model.....	77
3-13	Results from the COMSOL model – radial magnetic flux density (Tesla) and streamlines of total magnetic flux density	78
3-14	Comparison of the magnetic flux density in the air gap between the 1-D circuit model predictions and FEM results (averaged over entire gap volume)	79
3-15	Equivalent circuit representation of coupling between the mechanical and acoustic domains.....	80
3-16	Composite diaphragm model as an annular plate.....	81
3-17	Short closed cavity and its lumped model.....	84
3-18	Narrow circular orifice and its lumped model.....	86
3-19	Lumped model of a piston in an infinite baffle	88
3-20	Lumped element model of the electrodynamic ZNMF actuator referred to the acoustic domain.....	90
4-1	Schematic of the speaker-driven electrodynamic ZNMF actuator.....	94
4-2	Photograph of the speaker-driver, the cavity and the slot	94
4-3	Electrical impedance of the speaker-driver	95
4-4	Experimental setup for compliance measurement.....	96

4-5	Results from compliance measurement.....	97
4-6	Experimental setup for transduction factor measurement.....	99
4-7	Results from the transduction factor measurement.....	99
4-8	Setup for the impulse response test.....	101
4-9	Results from the impulse response test.....	101
4-10	Step response of the diaphragm and the curve fit.....	103
4-11	Equivalent circuit for the impulse response test.....	105
4-12	Typical hotwire calibration curve.....	106
4-13	Model predicted and experimentally measured output velocity of the speaker-driven ZNMF actuator for 3V pp voltage input.....	107
4-14	Schematic of Polydimethylsiloxane (PDMS) composite diaphragm actuator.....	109
4-15	Magnetic assembly schematic and photograph.....	110
4-16	Two-flange design for the rigid central boss.....	111
4-17	Diaphragm components.....	112
4-18	Centering ring for the central boss.....	113
4-19	Mold for the PDMS diaphragm fabrication and released PDMS diaphragm with the rigid center boss.....	113
4-20	Fully assembled device.....	114
4-21	Impedance measurements of 150-turn 40 AWG copper coil without the magnetic assembly.....	116
4-22	Setup for dc displacement test and the step response test.....	117
4-23	DC displacement test results.....	118
4-24	Displacement measurement under pressure load.....	119
4-25	Displacement measurements under uniform pressure load.....	120
4-26	Hotwire results and model comparisons for device A1.....	123
4-27	Hotwire results and model comparisons for device A2.....	123

4-28	Hotwire results and model predictions for device A3	124
4-29	Relative magnitudes of the slot damping and the total damping for device A1	125
5-1	Loaded electrodynamic actuator	128
5-2	Electrodynamic actuator circuit referred to the acoustic domain	128
5-3	Typical velocity frequency response of a second-order system	129
5-4	Comparison of the cavity and slot impedances for actuator A2	136
5-5	Magnetic assembly	137
5-6	Coil configuration using a multiple layers of bondable copper wire	138
5-7	Optimization results for maximizing blocked force for various power and mass constraints	144
5-8	Normalized effective area as a function of the solidity ratio	146
5-9	Acoustic compliance variation with the solidity ratio ($h/a = 0.08$)	147
5-10	Acoustic mass variation with the solidity ratio ($h/a = 0.08$)	149
5-11	Resonant frequency of the diaphragm ($h/a = 0.08$)	150
5-12	Variation of electroacoustic transduction coefficient G with solidity ratio ($h/a = 0.08$) ..	151
5-13	Variation of predicted output velocity with solidity ratio ($h/a = 0.08$)	153
5-14	Input and output as a function of frequency for actuator A2	154
5-15	Efficiency of actuator A2	155
5-16	Frequency response of actuator A1 for different diaphragm damping	157
5-17	Comparison of the frequency response of the baseline device and optimized designs for the three objective functions	159
5-18	Maximum output velocity as a function of maximum allowable input power for objective function 1	161
5-19	Maximum output velocity as a function of maximum allowable input mass for objective function 1	161
5-20	Comparison of the frequency response of the baseline device and optimized designs for the objective functions with a resonant frequency constraint	163

5-21	Variation of the average velocity from 0 – 300 Hz with the change in the design variables	164
5-22	Impedance measurement results for the optimized actuator	166
5-23	Damping measurement results for the optimized actuator	167
5-24	Optimized and baseline actuator hotwire and LEM comparisons	167
A-1	Magnetic assembly and the 1-D circuit model	173
A-2	Arrow plot of magnetic flux density in the magnetic assembly	174
A-3	Reluctance components of the magnetic assembly	174
A-4	Relative values of the reluctances of the magnet, core and air gap	176
A-5	B-H curve for an ideal and typical soft magnetic material	177
A-6	Results from the COMSOL model – total magnetic flux density (Tesla)	177
A-7	Radial magnetic flux density in the magnetic assembly of the optimized actuator	179
A-8	Total magnetic flux density	180
A-9	Non-linearity due to spatial variation of the flux density	181
B-1	Schematic for the mechanical driver an the simplified annular plate model	182
B-2	Transverse displacement – Model & FEM results ($b/a = 0.5$, $h/a = 0.08$, $a = 12.7 \times 10^{-3}$, $E_2 = 360$ kPa, $\nu_2 = 0.33$)	184

Abstract of Dissertation Presented to the Graduate School
of the University of Florida in Partial Fulfillment of the
Requirements for the Degree of Doctor of Philosophy

MODELING, DESIGN AND OPTIMIZATION OF ELECTRODYNAMIC ZNMF
ACTUATORS

By

Janhavi Agashe

May 2009

Chair: David P. Arnold
Major: Electrical and Computer Engineering

Zero-net mass-flux (ZNMF) actuators have been used for flow control applications such as separation control, thermal management. Electrodynamic transduction has been employed implementing these actuators in the past. However, a systematic design and modeling approach has been absent. This work presents a first-principles-based low order model for electrodynamic zero-net mass-flux (ZNMF) actuators. The lumped element modeling approach is used to model the multi-energy domain coupled system.

The model developed was validated using prototype ZNMF actuators. A low cost, flexible, repeatable hybrid manufacturing technique was developed to realize these prototype actuators. Based on this model, the parameters that have the most impact on the actuator were identified. The model predicted the performance of several actuator configurations with less than 10 % error.

Several design trends and tradeoffs were presented to enable intelligent design of these actuators. The model was also used to formulate a constrained optimization of the electrodynamic actuator. The optimized actuator was fabricated and characterized. The optimized actuator demonstrated at least 50 % higher output velocities as compared to the

baseline actuator. The optimized actuator achieved nearly 35 m/s maximum output velocity. The optimized actuator had volume of 15 cm³, overall mass of 90 g and maximum input power of 900 mW.

CHAPTER 1 INTRODUCTION

Small, light and low power electromechanical actuators are desired for various consumer, biomedical, and industrial applications. Zero-net mass-flux (ZNMF) actuators (also called synthetic jets) have been studied recently for applications in flow control, thermal management, fluidic mixing, etc [1],[2],[3],[4]. This dissertation focuses on mesoscale magnetic ZNMF actuators for flow control applications. Flow control—particularly separation control—has been studied for automotive and aerodynamic applications to reduce drag and improve lift and fuel efficiency.

The typical structure of a ZNMF actuator consists of an electromechanical transducer—e.g. piezoelectric, electrostatic, magnetic, etc.—that drives an oscillatory flow through a small orifice or slot in an attached cavity. The periodic expulsion and ingestion of fluid constitutes the “synthetic” jet, so named because it requires only the ambient fluid to produce a jet like structure rather than hoses, tubes, pumps, etc. Since no additional fluid mass is added to the flow during the operation, these actuators are also called zero-net mass-flux actuators. The device affects the flow field by addition of momentum to the flow. The device geometry and material properties decide the device performance. However, the actuation scheme also has a large impact on the device performance, and different approaches offer certain advantages and disadvantages.

For almost all applications of ZNMF actuators, large centerline velocities over a large range of frequencies are desired. To obtain high centerline velocities, large actuator volume displacements are required, implying large area, large stroke, or both. Of all possible electromechanical actuation schemes, magnetic-field based actuators are well-suited due to their high energy densities, large stroke and low operating frequencies. Magnetic actuators are commonplace in many macroscale systems and are well known for their performance and

reliability. Moreover, scaling analyses of these actuators indicate their applicability at smaller scales. Thus compact, efficient magnetic ZNMF actuators should be designable to meet performance requirements for emerging ZNMF applications [5],[6].

This thesis presents detailed modeling, design, characterization, and optimization approach for magnetic ZNMF actuators. Lumped element and finite element modeling techniques are used for the modeling of these actuators. Detailed characterization of various electrodynamic ZNMF actuators is also presented in order to validate the developed models and design guidelines. Various tradeoffs involved in the design of the actuators to meet target specifications are discussed, such as mass and power consumption vs. actuation force. Based on these tradeoffs, a design strategy is presented to obtain the desired actuator performance while meeting the necessary constraints. A preliminary constrained optimization was also performed and the optimized actuator was fabricated and characterized.

1.1 Background

A transducer is defined as any device that converts energy from one form to another[7]. Thus a transducer is a two port device that couples two different energy domains. Electromechanical transducers, which couple electrical and mechanical energy domains, are divided into two types—sensors and actuators. Sensors produce an electrical output proportional to some mechanical quantity, while actuators convert electrical energy into mechanical energy and thus produce mechanical motion. There are various transduction mechanisms by which this energy conversion can occur: magnetic, electrostatic, piezoelectric, etc.

Actuators are used in a wide variety of applications to achieve some mechanical function in response to an electrical drive or control signal. The performance requirements of an actuator—force, displacement, bandwidth, response time, power consumption, etc.—differ greatly depending on the specific application, and different tradeoffs in performance can be achieved by

careful design of the transduction mechanism, actuator geometry and materials. Device and system models are necessary to correlate these design parameters with performance specifications.

Magnetic-field-based actuators rely on the interaction between electrical input and magnetic fields to produce a mechanical force leading to rotational or linear motion. Rotary actuators such as electric motors have complete 360° range of motion for continuous rotation. On the other hand, linear actuators have restricted range of motion and generate finite in-plane or out-of-plane displacements. Typical applications of linear actuators include valves, fuel injectors, head positioners for disk drives, switches, relays, etc.

The remainder of this section discusses various performance characteristics of actuators. A brief comparison of magnetic-field-based actuators and other actuation schemes is presented. This comparison shows that the transduction scheme is an important factor that affects the performance of an actuator. Thus for a given application, the selection of a particular transduction scheme is crucial.

The various performance parameters for actuators are now discussed. Two of the most commonly specified parameters are “blocked force” and “free deflection”. Blocked force, F_b , refers to the force exerted at a given input excitation level when the actuator is not allowed to move. Free deflection, X_f , refers to the maximum displacement at a given input excitation without the actuator working against any external load. A detailed discussion of these parameters is included in section 2.1 where the two-port model for electromechanical transducers is presented.

Huber et. al. [8] discuss various performance indices of mechanical actuators that are important in choosing an actuator for a particular application, including actuator stress, actuator

strain, power density and bandwidth. Actuation stress σ is defined as the force per unit area produced by the actuator and thus is a measure of the force available from the actuator. The actuation strain ϵ is defined as the nominal change in length produced by the actuator and is a measure of displacement/stroke. The power density of the actuator is defined as the output mechanical power per unit volume of the actuator. The maximum power density can thus be defined as $\frac{\omega F_b X_f}{(2Vol)}$, where ω is the frequency of operation and Vol is the volume of the actuator.

Figure 1-1 shows the variation of actuation stress with actuation strain for various actuation schemes [8]. The solid lines show the maximum limits for each type of the actuator. Note two different types of magnetic-field-based actuators are listed: “moving-coil” and “solenoid.” In this thesis, these will be defined as “fixed-field-actuators” and “variable-field-actuators,” respectively, and the differences will be fully described in Section 2.3. It can be seen that although both moving-coil and solenoid type actuators have relatively small actuation stress (force); they produce large strain (displacements), which is a desirable for ZNMF actuators. Moreover, in the figure, the diagonal lines represent curves of maximum available work per unit volume or energy density. It can be seen that the magnetic actuation schemes offer higher available work output per unit volume as compared to most piezoelectric devices. It should be noted however that these plots only consider direct actuation and do not account for more complex flexure-based or kinematic amplification schemes.

Figure 1-2 shows the output power of various types of actuators as a function of frequency [8]. For ZNMF actuators, the frequency of operation is usually fairly low (~ 100 Hz) in order to affect the flow conditions. Although magnetostrictive actuators have larger power density, they have very small stroke and are not suitable for ZNMF applications. Piezoelectric actuators have

higher power density, attributed to their higher operating frequencies (recall piezoelectrics had lower energy densities).

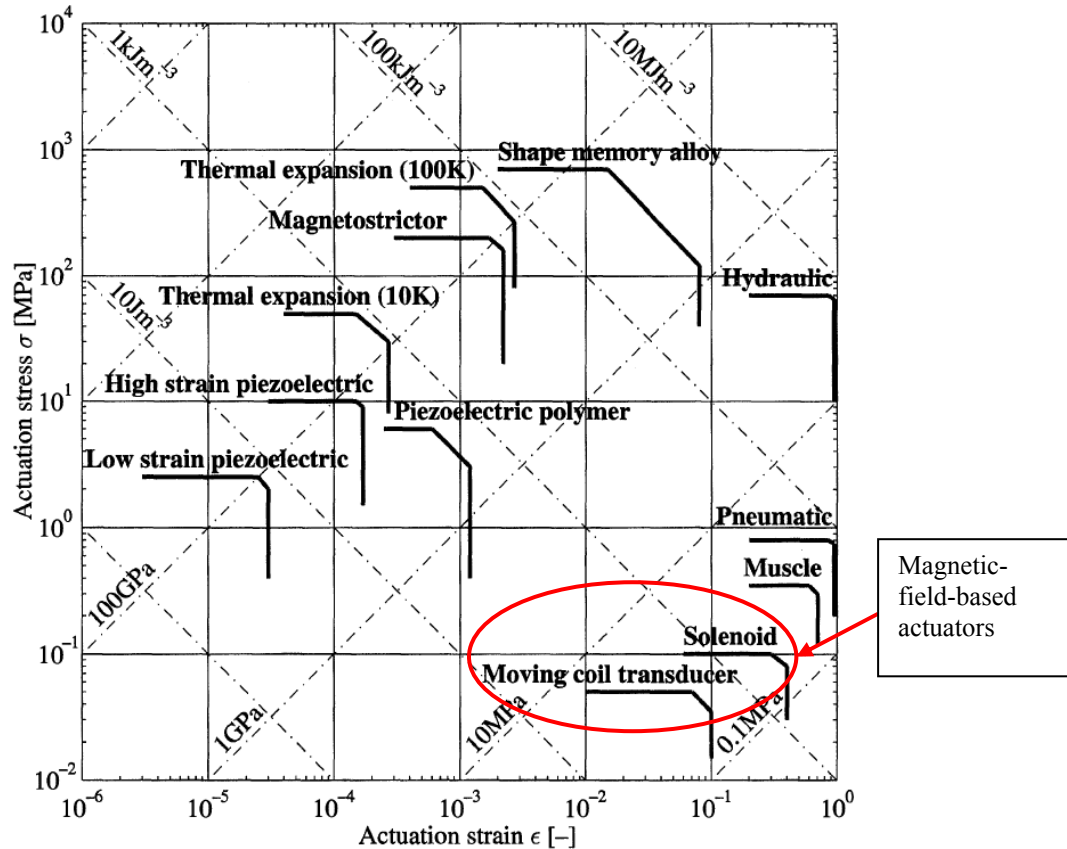


Figure 1-1. Actuation stress vs. actuation stress for various transduction mechanisms [8] (used with permission)

Moreover, the total bandwidth for moving-coil type actuators is also larger as compared to most piezoelectric actuators. This is important when “broadband” type actuators are desired where a large output displacement is desired over a large range of frequencies.

The comparisons discussed above incorporate only mesoscale devices. In most cases (particularly for ZNMF actuators), the weight, power consumption and even the overall size of actuators are important criteria in design and selection of actuators. Usually these parameters scale with the size, and it is important to know the scaling behavior of various actuators in order to determine their effectiveness at smaller scales.

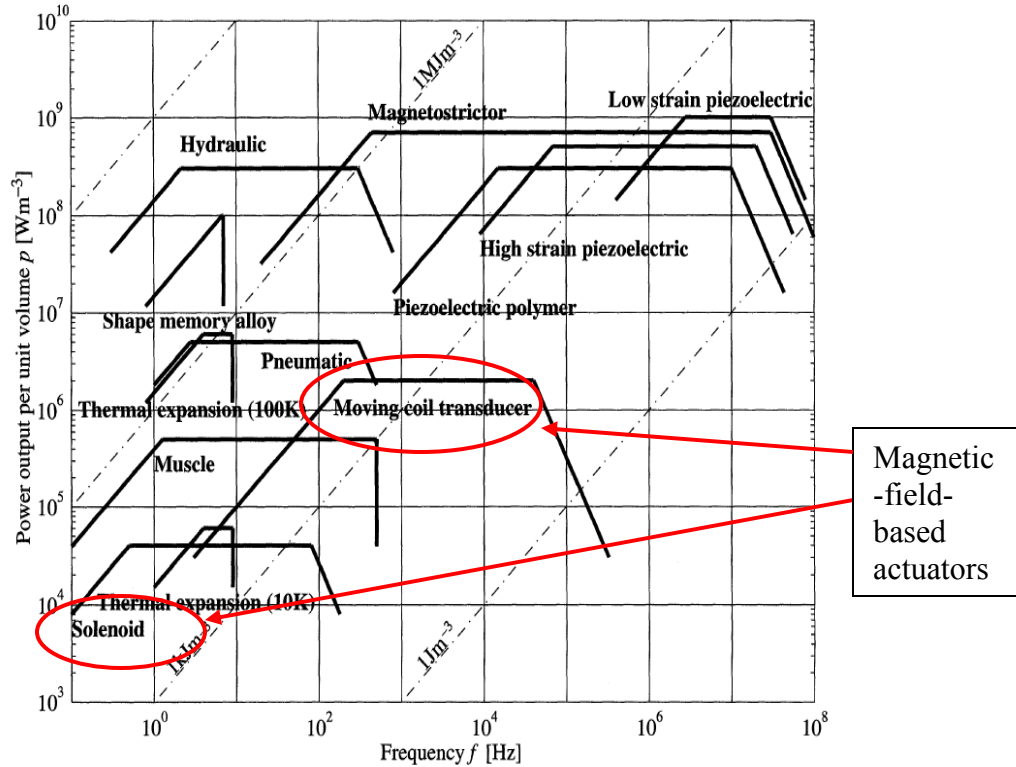


Figure 1-2. Frequency dependence of performance of various transduction mechanisms [8] (used with permission)

The favorable scaling of magnetic-field-based actuators has been discussed by [9], [10], [11]. However, the focus has been only on the scaling of the transduction scheme itself. The overall scaling of a functional actuator depends not only on the scaling of the transduction scheme but also on the scaling of the structures (beams, springs, coils, etc.) of the complete actuation system. Moreover, the manufacturing challenges presented at smaller scales may require different material selections, fabrication methods, geometries, etc. This work presents a detailed investigation of overall scaling of magnetic ZNMF actuators.

In order to design ZNMF actuators best-suited for a given application, accurate models of the transduction scheme and overall actuators are necessary. Both computational techniques (such as finite element modeling) and low-order analytical models have been developed for ZNMF actuators. Analytical models provide better physical insight into device operation and

hence provide excellent design tools. However, analytical models usually are first-order approximations, and finite element models are necessary in order to study the higher order and nonlinear effects present in the device.

ZNMF actuators are coupled systems with various energy domains—electrical, mechanical and fluidic/acoustic—interacting with each other. Lumped element modeling (LEM) is one of the low-order analytical approaches used to model such systems since the 1920s, particularly in the field of electroacoustics [7, 12, 13]. McCormick [3] developed a coupled model of a magnetic speaker-driven ZNMF actuator. A transfer function for the output velocity as a function of input voltage was presented. Although an equivalent circuit was presented for the overall actuator, no details were described for the individual model parameters for the magnetic assembly and the mechanical driver. Gallas [14] presented coupled equivalent circuit based model for a piezoelectric ZNMF actor using the lumped element modeling technique. The model was successfully used to study the impact of various geometry parameters and material properties on the device performance. In addition to LEM, various numerical techniques have also been used to model ZNMF actuators. However, these methods are time- and computationally-intensive and provide little insight into the operation of the device [15-17].

Thus the goal of this work is to use the lumped element modeling technique to develop and experimentally validate an equivalent circuit model for magnetic ZNMF actuators, paralleling the work Gallas [14] performed for the piezoelectric ZNMF devices. Finite element modeling will also be used to validate some aspects of the lumped model. The validated model will provide various physical insights into the actuator physics, and design and optimization strategies will be developed based on these insights.

1.2 Research Objectives

The primary goal of this research is a multi-faceted investigation of the modeling, design, scalability and optimization of magnetic-field-based ZNMF actuators. The models developed are validated by a detailed characterization experiments. These models are then used to design ZNMF actuators that meet necessary target specifications of centerline velocity, frequency of operation, power consumption, etc. The various tradeoffs that affect the actuator performance are investigated, and a systematic approach is presented for design of magnetic ZNMF actuators to meet performance metrics.

The thesis also presents a systematic scaling analysis of magnetic-field-based actuators using a lumped element modeling framework to develop coupled, multi-domain models of magnetic actuators that account for the magnetic, mechanical as well as acoustic/fluidic components of the device[7, 12]. These models will be used for scaling analysis and for design and optimization of magnetic-field-based ZNMF actuators. Although, several scaling analyses just for the magnetic transduction scheme are found in the literature, scaling analysis of the entire actuator has been lacking. Overall scaling analysis of the devices provides important physical insight into the biggest factors that influence the performance of the device.

The research contributions of this work are as follows

- Development and validation of coupled, multi-energy domain low-order (lumped-element) system models for magnetic ZNMF actuators. The models are validated experimentally and using finite element analysis.
- Development of fabrication methods for mesoscale ZNMF actuators using hybrid manufacturing techniques. The fabrications methods, challenges, limitations etc. for all the actuator components are detailed.
- Development of an overall design approach to achieve desired target specifications from a magnetic ZNMF actuator. A systematic discussion of tradeoffs and trends involved in the design of magnetic ZNMF actuators is presented.
- Demonstration and characterization of an optimized magnetic ZNMF actuator.

1.3 Thesis Outline

This dissertation is divided into 5 chapters and 3 appendices. Chapter 1 detailed the motivation for this work and the proposed research goals as well the contributions of this work. Chapter 2 provides detailed background information and literature review relevant to this work. Chapter 2 introduces the basics of magnetics and magnetic-field-based actuators. Scaling analysis of magnetic-field-based actuators is also included. The literature review is divided into two different sections: a review of previously reported ZNMF actuators and a brief review of modeling techniques used to analyze ZNMF actuators. Chapter 3 discusses modeling of electrodynamic ZNMF actuators. Chapter 4 discusses the verification of the lumped element model for a speaker-driven electrodynamic ZNMF actuator. The fabrication and characterization of custom-built mesoscale electrodynamic ZNMF actuators is also presented Chapter 4. Chapter 5 discusses optimization strategy and various tradeoffs encountered in the design of magnetic ZNMF actuators. The characterization of optimized magnetic ZNMF actuators is also presented in Chapter 5. Chapter 6 discusses the conclusions and the some future directions for this work. The feasibility of scaling these actuators at small scales is investigated. The fabrication, material choices and the geometry that are viable for smaller sizes are discussed.

CHAPTER 2 BACKGROUND

A brief overview of the basics of electromechanical transduction is presented in Chapter 2 with an emphasis on magnetic actuators. For the purpose of this dissertation, “magnetic actuators” or more explicitly “magnetic-field-based actuators” are those devices that use quasi-static magnetic fields as the primary fields for energy conversion and whose operation are governed by the magnetostatic Maxwell equations [18]. There are numerous configurations using coils and magnets that can be employed for magnetic actuators, but these can be generally divided into two distinct types, defined in this thesis as: fixed-field actuators and variable-field actuators. In fixed-field actuators (FFAs), the magnetic field distribution does not significantly change during the device operation, whereas in variable-field actuators (VFAs) the device operation relies on a large change in the magnetic field distribution. Magnetostrictive actuators, which use materials that develop strain in the presence of an external magnetic field, are not discussed in this work.

In Chapter 2, the origin of magnetic fields from both material magnetization and current carrying conductors is first discussed. Then, the functional operation of the magnetic-field-based actuators is described, and scaling analysis for the two types of magnetic actuation schemes is presented. A detailed summary of various ZNMF actuators reported in the literature is presented, and an overview of some modeling approaches used for ZNMF actuators is also discussed.

2.1 Transduction Mechanisms

A transducer is any device that converts energy from one domain to another. Transducers can be also classified into various categories depending on their energy conversion behavior. Energy-conserving transducers convert all energy in one domain to the other. Typical examples of this type are magnetic transducers (both FFA and VFA), electrostatic transducers, and

piezoelectric transducers. Conversely, piezoresistive and thermoelastic transducers are non-energy conserving. In non-energy-conserving transducers, some energy is dissipated in various losses inherent to the transduction mechanism. For example in piezoresistive transducers, some energy is needed to maintain a current through the resistors in order to measure the change in resistance due to the incident mechanical energy.

Any energy-conserving transducer can be represented as a generic two-port network as shown in Figure 2-1 [13]. Here E_1 and F_1 represent the generalized effort and flow variables in the first energy domain. The product of the effort and flow variables is power.

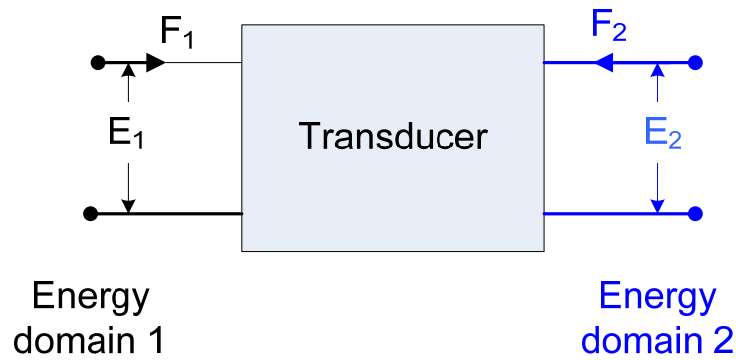


Figure 2-1. Two port model of a transducer

The relationship between the effort and flow variables can be expressed in matrix form as

$$\begin{bmatrix} E_1 \\ E_2 \end{bmatrix} = \begin{bmatrix} A & B \\ C & D \end{bmatrix} \begin{bmatrix} F_1 \\ F_2 \end{bmatrix}. \quad (2.1)$$

Note that this form is called the impedance representation as the effort variables (E_1 and E_2) are expressed as the functions of the flow variables (F_1 and F_2). B and C are the coupling terms between the two energy domains. Thus for electromechanical transducers, the two-port model is shown below

$$\begin{bmatrix} F \\ V \end{bmatrix} = \begin{bmatrix} Z_m & T_{me} \\ T_{em} & Z_e \end{bmatrix} \begin{bmatrix} U \\ I \end{bmatrix}, \quad (2.2)$$

where F and V are the force and voltage, respectively. T_{me} and T_{em} are transduction coefficients [7]. The term Z_e is the blocked electrical impedance, i.e. the input electrical impedance when the mechanical motion is blocked such that the velocity is zero. Similarly, Z_m is the open-circuit mechanical impedance, i.e. the mechanical impedance when the electrical terminals are open-circuited and no current is allowed to flow.

Energy-conserving transducers can be classified further into various categories. A reciprocal transducer is the one where the transduction coefficients are the same in both directions i.e. $T_{me} = T_{em} = T$. Reciprocal transducers thus have the same transduction coefficients operating in either direction (electrical to mechanical or mechanical to electrical). Non-reciprocal transducers, on the other hand, have different transduction coefficients dependent on the direction [7]. For example, piezoelectric and electrostatic transduction schemes are reciprocal, whereas piezoresistive sensing and electrothermal actuation are not. When the transduction coefficients between the two domains is equal in magnitude but opposite in sign ($T_{me} = -T_{em}$), the transduction mechanism is called “anti-reciprocal”. This usually arises due to the choice of the sign convention [7]. Fixed-field or electrodynamic transduction scheme is anti-reciprocal.

When the transduction coefficients (T_{me} and T_{em}) between the two energy domains are constant, i.e. the effort variable in the second energy domain is directly proportional to the effort (or flow) variable in the first domain, the transducer is referred to as a linear transducer. In non-linear transducers, the coupling between the energy domains is non-linear. Fixed-field magnetic transducers are linear, energy-conserving and anti-reciprocal. Variable-field magnetic transducers are also energy-conserving and anti-reciprocal, but they are in general, non-linear.

Based on the two-port network model above, the blocked force produced by actuator is defined as

$$F_b = T_{me} I . \quad (2.3)$$

The internal impedance or the open-circuit mechanical impedance of the actuator Z_m is defined as

$$Z_m = F/U \Big|_{I=0} . \quad (2.4)$$

Thus if the actuator is not working against any other external force, the blocked force is balanced by the restoring force due to the internal stiffness. In other words, for a given current, a force will be generated, resulting in a displacement that is limited by the internal stiffness of the actuator.

This resulting displacement is called the free displacement, where “free” indicates the actuator is not working against any external mechanical load. The relationship between the blocked force and the free displacement can be given by

$$X_f = -F_b / j\omega Z_m . \quad (2.5)$$

Here, harmonic motion of the actuator is assumed. Note that the negative sign indicates that the restoring force is created by the actuator internal impedance, which opposes the “useful” output force generated by the actuator. Moreover, the blocked force and the free displacement represent the maximum force and displacement bounds, respectively, that the actuator can achieve. The open-circuit mechanical impedance Z_m of the actuator is usually a function of the frequency and thus the free displacement is also a function of the frequency.

The total available output force, F , (the force available to perform useful work) can be expressed as[19]

$$F = F_b - j\omega Z_m x \quad (2.6)$$

where x is the displacement. Figure 2-2 shows all the forces acting within an actuator pictorially in the form of a free body diagram. It can be seen that the total “useful” force produced by the actuator is limited by its blocked force as well as internal stiffness.

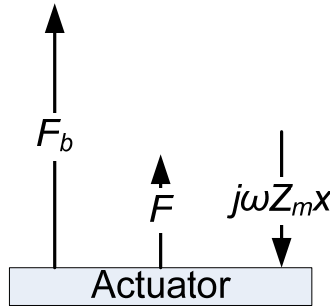


Figure 2-2. Free body diagram of the all the forces acting on an actuator

Figure 2-3 shows typical operating characteristics of a general actuator where the available force F is shown as a function of the displacement x . For a linear actuator, the operating characteristics of the actuator will be a straight line connecting the free displacement and the blocked force points. The blocked force (and hence the free displacement) is a function of the electrical input to the actuator. For example, in the case of a fixed-field magnetic actuator, the blocked force is the Lorentz force produced given by $F_b = BLI$, where B is the magnetic flux density, L is the length of the coil and I is the input current. In the case of piezoelectric actuators, the blocked force is given by $F_b = dV$, where d is the piezoelectric charge modulus and V is the applied input voltage. Thus as the input to the actuator is increased, the blocked force and the free displacement both increase. This is indicated by the parallel lines in Figure 2-3. The slope of the operating characteristics always remains the same. If the actuator is operating at frequency ω , the maximum power it can supply is given by $\frac{\omega F_b X_f}{2}$. It should also be noted that the free displacement of an actuator is also the function of the frequency. This is because the moving structure of the actuator has a finite mass in addition to the compliance and hence behaves as a standard second-order system.

For ZNMF type applications, large displacements are required. Thus actuators with large blocked force and small internal stiffness are ideal for ZNMF applications as can be seen from

(2.6). However, the resonant frequency and bandwidth are directly proportional to the internal stiffness. Thus there is an inherent tradeoff between maximum achievable free displacement and maximum bandwidth. Other considerations such as power consumption, quality factor, etc. may also be important.

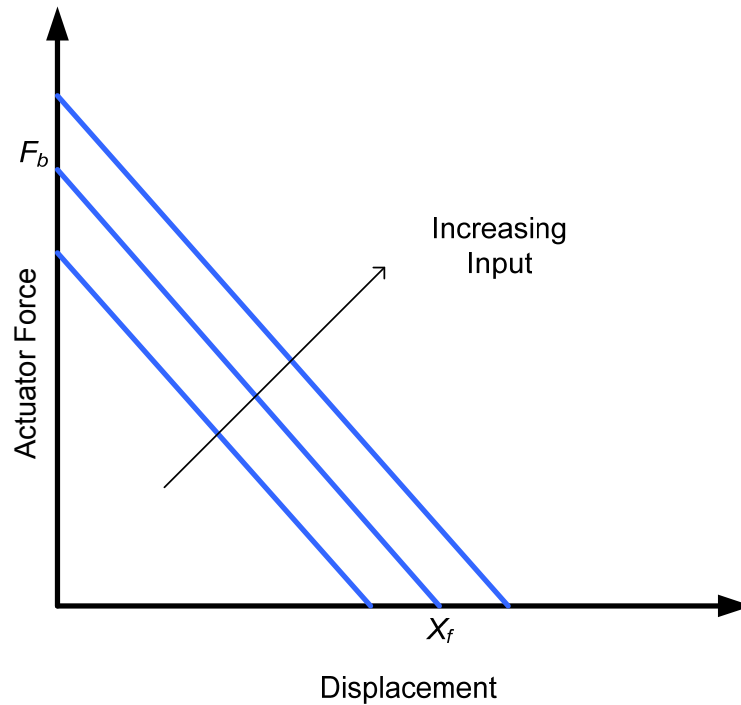


Figure 2-3. Operating characteristics of a typical actuator

2.2 Basics of Magnetic Transduction

Magnetic and electric fields are usually described in terms of the force they produce on charges. A charge q moving with a velocity \vec{v} , experiences a force \vec{F} given by

$$\vec{F} = \underbrace{q\vec{E}}_{\text{Electric force}} + \underbrace{q\vec{v} \times \vec{B}}_{\text{Magnetic force}}, \quad (2.7)$$

where \vec{E} is the *electric field intensity* and \vec{B} is the *magnetic flux density*. The magnetic flux density is the most important parameter in the analysis of magnetic systems. The unit of magnetic flux density is thus Newton/(Ampere-meter). However, the most commonly used unit is the tesla (T) or equivalently weber/m² (Wb/m²). Magnetic flux arises from two fundamental

sources: electric currents (sometimes called *free currents*) and intrinsic atomic moments in materials due to orbital motion of electrons and spin moments (sometimes called *bound currents*) [20]. The total magnetic flux density at any point in space is given by the constitutive equation

$$\vec{B} = \mu_0 (\vec{H} + \vec{M}), \quad (2.8)$$

where μ_0 is the permeability of free space ($4\pi \times 10^{-7}$ H/m), and the two summed terms indicate the two origins of the magnetic flux density. The first term \vec{H} is the *magnetic field intensity* or simply *magnetic field* and represents the contribution from free electric currents. The SI unit of magnetic field intensity is Ampere/meter (A/m). The second term \vec{M} is the *magnetization* and represents the contribution from the atomistic magnetic moments induced inside the material under consideration. Magnetization has the same units as magnetic field intensity (A/m) and may be a function of the applied magnetic field. In free space there is no induced magnetization; thus $\vec{M} = 0$, and the relationship between \vec{B} and H simplifies to $B = \mu_0 H$. In contrast, in any real material, the material magnetization $M \neq 0$ and the full expression must be used. Moreover, for ferromagnetic materials, the material magnetization is usually a strong nonlinear function of the magnetic field, leading to complex magnetic field relationships as will be described later. The following sections describe the magnetic fields produced by electric currents and induced magnetic fields inside various magnetic materials.

2.2.1 Magnetic Field Generated by Current Distributions

The incremental magnetic field $d\vec{H}$ generated at a point P by a differential current element of length dL carrying current I is given by the Biot-Savart law [21],

$$d\vec{H} = \frac{Id\vec{L} \times \hat{r}}{4\pi r^2}. \quad (2.9)$$

Here, r is the distance between point P the current element, and \hat{r} is the unit vector along the line connecting P and the current element as shown in Figure 2-4. The magnetic field is inversely

proportional to the square of the distance and directly proportional to current. The total magnetic field is calculated by integrating the contribution of the individual elements over the length of the current carrying filament,

$$\vec{H} = \oint_L \frac{Id\vec{L} \times \hat{r}}{4\pi r^2}. \quad (2.10)$$

The differential current element $Id\vec{L}$ can also be expressed in terms of a surface current density K (units A/m) or a volume current density J (units A/m²). Thus the magnetic field can be calculated as

$$\vec{H} = \int_s \frac{\vec{K} \times \hat{r}}{4\pi r^2} dS. \quad (2.11)$$

$$\vec{H} = \int_v \frac{\vec{J} \times \hat{r}}{4\pi r^2} dV \quad (2.12)$$

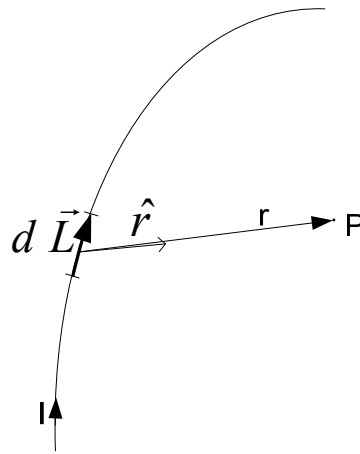


Figure 2-4. Magnetic field generated by a current element

An electromagnet refers to a setup that uses an electric current to generate a desired magnetic field. One of the most commonly used electromagnet configurations is a solenoidal coil. Figure 2-5 shows a long solenoidal coil of length L that carries current I . The magnetic flux density H established inside the coil is fairly uniform everywhere and approximated by [21]

$$H = \frac{NI}{L}, \quad (2.13)$$

where N is the number of turns in the coil. The direction of the magnetic field is given by the “right-hand rule.” The magnitude and direction of the magnetic field can be modified by changing the current in the coil. Moreover, if the current is sinusoidal, sinusoidal fields can be established.

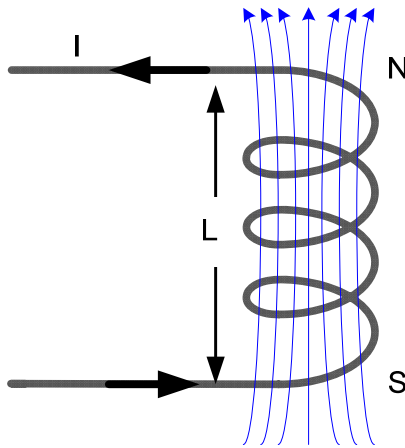


Figure 2-5. Magnetic field generated by a solenoidal coil

2.2.2 Magnetic Field due to Intrinsic Material Properties

The previous section described the magnetic field \vec{H} arising from free currents. This section describes the origin of material magnetization \vec{M} . Every atom consists of a central nucleus and electrons revolving around it. These moving charges act like current loops that generate tiny magnetic moments, similar to the solenoidal coil described above. In addition to the electron orbital magnetic moments, *electron spin* and *nuclear spin* magnetic moments arise due to quantum effects [21]. The net *internal moment* is thus the sum of the contributions from the electron orbital moments and the electron and nuclear spin moments. All materials can be magnetically classified based on the distribution of these atomic moments and their response in the presence of an externally applied field. While details of the origins of material magnetization

is beyond the scope of this thesis, a brief summary of different classes of magnetic materials is included below [22].

In *diamagnetic materials* the magnetic moments due to orbital motion of the electrons and the spin moments effectively cancel each other, and hence the net magnetic moment of each atom is zero. In the presence of an external field, however, the magnetic force on the orbital electrons changes the orbital velocity (the orbital radius cannot change due to quantization) in such a way that the total internal moment is decreased. As a result, diamagnetic materials are repelled from a magnet, although this force is very weak at moderate fields. Water, bismuth and noble gases (helium, neon, etc.) are examples of diamagnetic materials.

In *paramagnetic materials*, the orbital moment and spin moments do not cancel each other completely. Each atom exhibits a small moment, but the orientation of these atomic moments is randomly distributed, and as a result the material as a whole does not exhibit a net magnetic moment. When an external magnetic field is applied, a torque on the individual atomic moments tends to align them and increase the net magnetic moment inside the material. When the external field is removed, the atoms return to their randomly aligned distribution and the net magnetic moment is again zero. Typical examples of paramagnetic magnetic materials are oxygen, tungsten, potassium, etc.

Ferromagnetic materials are the most important type in the context of magnetic actuators. These are materials that have large net moments even in the absence of an external field. The atomic moments in large areas of the material are aligned in the same direction due to interatomic forces. These regions are called domains. Although individual domains have large moments, they are initially randomly distributed inside the material. Thus, the material has near zero net magnetic moment. When an external magnetic field is applied, however, the domains

aligned in the direction of the field grow in size while the other domains grow smaller through a process called domain wall motion. When the field is removed, all the domains do not return to their initial random state. This results in a non-zero magnetic moment even when the external field is zero. This phenomenon is called magnetic hysteresis.

The magnetization \vec{M} of a magnetic material is the net magnetic moment per unit volume of the material. The magnetization of an ideal ferromagnetic material M_{int} is given by [21]

$$M_{int} = \chi H_{ext} + M_r, \quad (2.14)$$

where H_{ext} is the external applied field, χ is the susceptibility of the ferromagnetic material and

M_r is the remnant magnetization. Note that this equation does not describe the hysteresis and saturation behavior present in all ferromagnetic materials. The impact of these effects is

discussed in later sections. The susceptibility χ is the measure of induced magnetization in the

material, and M_r is the magnetization that remains when the external field is zero. Another

parameter, the intrinsic coercivity H_{ci} , is the field required to reduce the internal magnetization to

zero. From (2.4), the coercivity can be defined as

$$H_{ci} = \frac{M_r}{\chi}. \quad (2.15)$$

Ferromagnetic materials can be further classified into “soft” and “hard” on the basis of their intrinsic coercivity and remnant magnetization.

Soft magnetic materials have small values of remnant magnetization M_r and intrinsic coercivity H_{ci} . Figure 2-6 shows the magnetization induced inside a soft magnetic material and the M-H relationship for the same. The M-H loop of a soft magnetic material shows some hysteresis behavior where the internal magnetization is not zero when the external field is removed. Ideally, however, the remnant magnetization is zero and the hysteresis is small, i.e. the coercivity is zero.

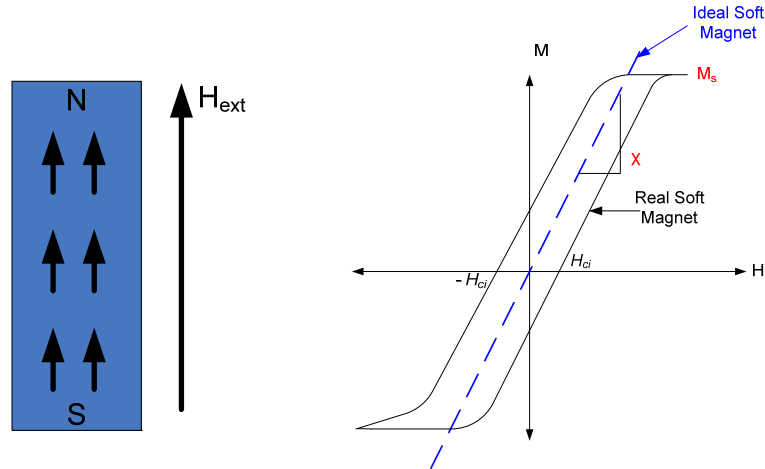


Figure 2-6. Soft magnetic material

Under this assumption, the relationship between the magnetic flux density B and applied field for an ideal soft magnetic material can be described as

$$B = \mu_0(H_{ext} + M_{int}) \approx \mu_0(1 + \chi)H_{ext} = \mu_0\mu_r H_{ext}. \quad (2.16)$$

Here $\mu_r = 1 + \chi$ is the relative permeability of the soft magnetic material. Thus the magnetic flux density created in a soft magnetic material is directly proportional to the external applied field and the relative permeability. This can also be seen from the blue curve in Figure 2-6 for the ideal soft magnet. At some point, however, all of the domains in the soft magnetic material are aligned to the external magnetic field, and any increase in the external field does not lead to an increase in the magnetization. This maximum magnetization achievable in the soft magnetic material is called the saturation magnetization M_s .

Examples of soft magnetic materials are iron, nickel, permalloy (nickel-iron alloy) and other alloys of these metals that develop strong internal magnetization only in the presence of an external magnetic field. In many applications, soft magnets are used to concentrate and guide the magnetic field in certain regions, and usually high relative permeability is desired. Typical values of relative permeability of commonly used soft magnetic materials are shown in Table 2-

1.

Table 2-1. Relative permeability of soft magnetic materials [23]

Material	Relative permeability μ_r
Mu metal (Nickel ~ 75 % – Iron ~ 25 % Alloy, Copper and Molybdenum)	~25000
Carbon Steel	~700
Permalloy (Nickel-Iron)	~8000
Soft Ferrites (Iron oxide alloys)	~5000

In contrast to soft ferromagnetic materials, hard ferromagnetic materials have a substantial remnant magnetization M_r , and their coercivity is also large. When an external field is applied, the total magnetic flux density is the sum of the remnant magnetization and the external field and is given by

$$B = \mu_0(H_{ext} + M_{int}) = \mu_0(1 + \chi)H_{ext} + \mu_0M_r = \mu_0\mu_rH_{ext} + \mu_0M_r. \quad (2.17)$$

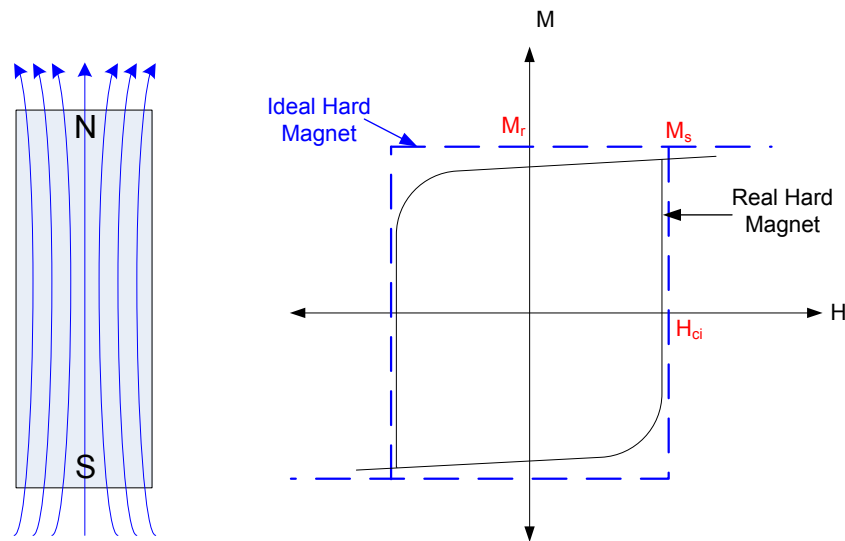


Figure 2-7. Hard magnetic material

The magnetic field produced by a hard magnet and the typical M-H loop is shown in Figure 2-7. Ideal hard magnetic materials have a “square” M-H loop as shown. This means that the remnant magnetization M_r and the saturation magnetization (M_s) are equal. In other words, the magnetization of the material changes very little in the presence of the applied field. An important figure of merit for a hard magnetic material is the “squareness ratio,” defined as the

ratio of the remnant magnetization to the saturation magnetization. The squareness ratio of an ideal hard magnetic material is unity.

Some of the most commonly used hard magnetic materials are neodymium-iron-boron (Nd-Fe-B), samarium-cobalt (Sm-Co) and alnico (Al-Ni-Co) metal alloys as well as ferrites. For all applications, a large remnance and squareness ratio of 1 are desired. Typical values of remnance for commonly used hard magnet materials are shown in Table 2-2.

Table 2-2. Magnetic properties of hard magnet materials [22]

Material	Remnance (T)
Neodymium-Iron-Boron (Nd-Fe-B)	1.2 – 1.3
Samarium-Cobalt (Sm-Co)	0.87 – 1
Aluminum-Nickel-Cobalt (Al-Ni-Co)	0.74 – 1.2
Hard Ferrites (Barium or Strontium Ferrite)	~ 0.1 – 0.35

2.2.3 Equivalence between Current Distributions and Magnetic Materials

Two very distinct origins of magnetic fields are discussed in the previous sections namely electric currents and intrinsic magnetizations in magnetic materials. However, the magnetization of a material can be represented as a current distribution and vice versa. The relationship between equivalent current densities and the magnetization are

$$\begin{aligned}\vec{J} &= \nabla \times \vec{M} \\ \vec{K} &= \vec{M} \times \hat{n}\end{aligned}\tag{2.18}$$

Here \vec{M} is the magnetization, \vec{J} is the volume current density, \vec{K} is the surface current density and \hat{n} is the unit normal to the surface of the material. Thus for a hard magnetic material, where the magnetization can be assumed uniform and constant, the volume current density is zero and there exists a constant surface current density equal to the remnant magnetization of the magnet. This is shown schematically in Figure 2-8 [20]. In the case of a soft magnetic material, there is no magnetization present without an external magnetic field, but (2.18) still can be applied by letting the magnetization be a function of the spatially-varying externally applied field.

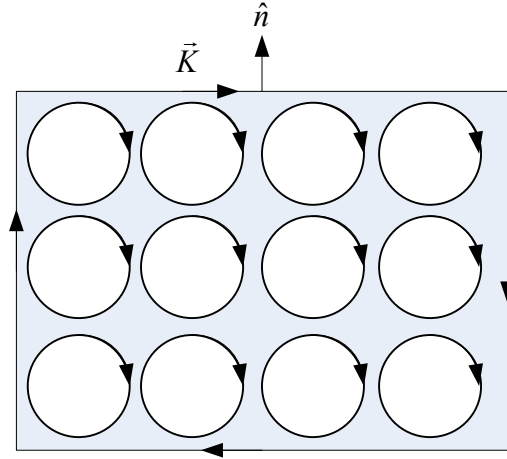


Figure 2-8. Hard magnet representation as an equivalent current density

2.3 Magnetic Field Based Actuators

A steady magnetic field is capable of producing a force on moving charges. The force \vec{F} on a charge q moving with a velocity \vec{v} in the presence of external magnetic flux density \vec{B} is given by the Lorentz force equation [21],

$$\vec{F} = q\vec{v} \times \vec{B} . \quad (2.19)$$

It can be seen that the force is in a direction perpendicular to both the velocity and the magnetic field. Thus the force on a current distribution, composed of a large number of moving electrons, can be calculated by integrating the force all the electrons that constitute the current distribution. Thus, the force, $d\vec{F}$, acting on a differential surface element dS with surface current density of \vec{K} is given by

$$d\vec{F} = (\vec{K} \times \vec{B}) dS . \quad (2.20)$$

The total force is calculated by integrating the differential force over the entire surface. The force acting on a volume element dV due to a volume current density \vec{J} is also calculated in a similar fashion.

$$d\vec{F} = (\vec{J} \times \vec{B}) dV. \quad (2.21)$$

Thus forces due to interactions between current distributions and magnetic fields are known. The forces on magnetic materials due to external magnetic fields can also be calculated by representing the magnetic materials as equivalent surface and volume current densities as described in section 2.2.3.

Magnetic actuators, where a specified force is produced in response to an electrical current or voltage, can be created in many different configurations. Most generally, these different configurations can be classified into two different categories based on the magnetic field distributions in the actuators. Fixed-field actuators (FFAs) are actuators where the mechanical motion of the device does not result in substantial change in the magnetic field distribution.

The most common configuration used for FFA is the interaction between a current coil and a magnetic field generated by a hard magnet. These actuators are called voice-coil actuators, moving-coil actuators or electrodynamic actuators in the literature [7, 12]. In contrast, in variable-field actuators (VFAs), the magnetic field distribution changes when the components of the device move with respect to each other. These actuators usually include a combination of current carrying coils, soft magnets and/or hard magnets. In the literature, VFAs are typically called variable-reluctance actuators or sometimes just electromagnetic actuators.

2.3.1 Fixed-Field Actuators (Electrodynamic)

These actuators involve interaction between magnetic fields, such that the overall field distribution does not change substantially during the device operation. In most cases, a hard magnet creates a fixed magnetic field on a current carrying coil. Soft magnetic materials may be included in the magnetic circuit in order to increase the magnetic flux density acting on the coil.

The force \vec{F} produced on a current carrying wire as shown in Figure 2-9 is given by

$$\vec{F} = I\vec{L} \times \vec{B}, \quad (2.22)$$

where \vec{B} is the magnetic flux density, \vec{L} is the vector along the length of the coil and I is the current through the coil. Note that force generated on the current carrying coil is just a 1-D solution of the Lorentz force on a moving charge, e.g. see (2.19). The force is directly proportional to the input current and is in the direction perpendicular to both the current and the magnetic field. The direction of the force is given by “right-hand-rule” [21]. Note that the direction of the current indicated here is the conventional direction of current and hence the electron velocity (\vec{v}) is actually opposite to that of the current direction. However, as the electron has negative charge, the force expressions (2.19) and (2.22) are equivalent. The electrodynamic transduction scheme will be further discussed in Chapter 3.

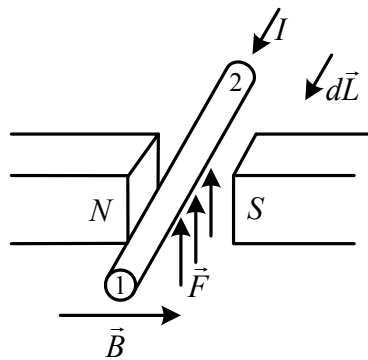


Figure 2-9. Electrodynamic transduction

A typical configuration of an axisymmetric mesoscale voice-coil actuator is shown in Figure 2-10. The magnetic circuit consists of a hard magnet and soft magnetic core used to direct the field in the radial direction. A solenoid coil is attached to a movable piston that is mounted to a rigid support via a spring. The hard magnet is magnetized in the z-direction as shown, but the soft magnet directs the field so that it is in the radial (r) direction in the air gap. The current is in the θ -direction (in and out of the page). The current entering into the coil is indicated by a cross, and current leaving the coil is shown by a dot. Thus the force produced in the z-direction. This

results in transverse motion of the piston. The dynamics of the actuator are determined by the mechanical components (the piston and the spring) of the actuator.

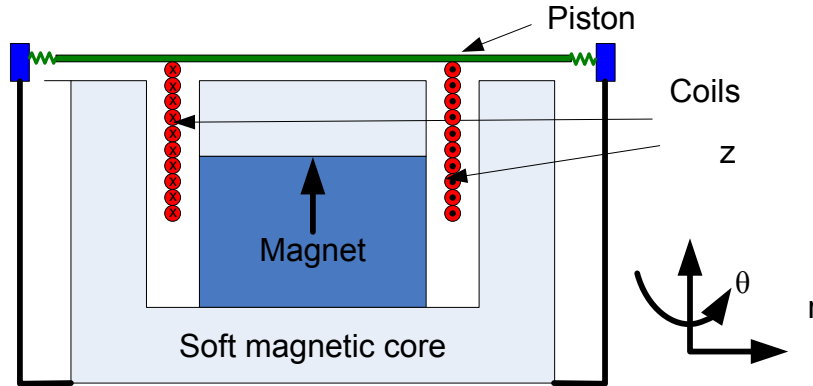


Figure 2-10. Typical mesoscale voice-coil actuator

2.3.2 Variable-Field Actuators (Variable-Reluctance)

Variable-field actuators generate a mechanical force using the interaction between a magnetic field produced by an electromagnet and the induced field in a soft magnetic material. Reluctance of a magnetic circuit is analogous to resistance in an electrical circuit and depends on the geometry and material properties of the magnetic path. The magnetic interactions in these devices always tend to reduce the reluctance seen by the magnetic field, and hence they are sometimes also called variable-reluctance actuators.

The typical configuration of these actuators is shown in Figure 2-11 [13], commonly used in magnetic relays, magnetic plungers, etc. The flux in the gap is set up by the electromagnet (current-carrying coil). The soft magnetic core is used to direct and concentrate the flux. The equilibrium position of the moving soft iron slab is achieved when the magnetic force balances the mechanical restoring force exerted by the spring. The magnetic force is given by [24], [13]

$$F_{mag} = \nabla W_{mag} \quad (2.23)$$

where W_{mag} is the magnetic energy,

$$W_{mag} = \frac{1}{2} \frac{MMF^2}{\mathfrak{R}} = \frac{1}{2} \frac{(NI)^2}{\mathfrak{R}}. \quad (2.24)$$

where MMF is the magnetomotive force (the product of the current I through the coil and N is the number of turns on the coil) and \mathfrak{R} is the reluctance of the circuit. The reluctance of the magnetic circuit is directly proportional to the length of the magnetic circuit and inversely proportional to both the cross-sectional area and the magnetic permeability of the magnetic path.

The reluctance of a magnetic path of length l and cross-sectional area A is given by

$$\mathfrak{R} = \frac{l}{\mu A} \quad (2.25)$$

where μ is the magnetic permeability of the material.

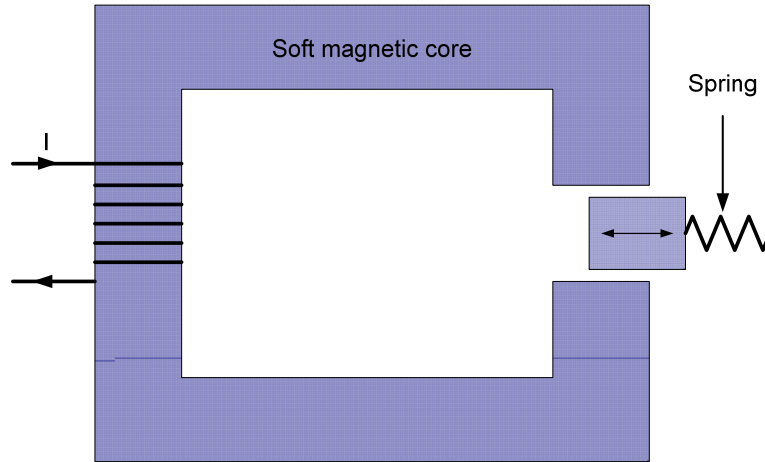


Figure 2-11. Typical configuration of mesoscale solenoid actuator

It can be seen from (2.23) and (2.24) that force is not linear with respect to the input current. Moreover, the force is unidirectional and always tries to close the gap and reduce the gap. The specific expressions for the force can be calculated based on the geometry of the device. The total magnetic force for the topology shown in Figure 2-11 is given by [13]

$$F = \frac{(NI)^2}{2x_0} \left(\frac{\mu_0 A}{x_g + \frac{\mu_0 L_m}{\mu}} \right) \quad (2.26)$$

where x_0 is the fraction of the gap area affected by the moveable portion, x_g is the length of the air gap and L_m is the length of the magnetic path and μ is the magnetic permeability of the core material.

2.4 Scaling of Magnetic Actuators

The previous section describes the differences in operation and geometry of the two types of magnetic-field based actuators. These are important considerations when choosing an actuator for a given application. In addition to these, the scaling of these two actuators is also significant particularly when compact actuators are desired.

Several studies have compared scaling of magnetic actuators with other types of actuation schemes [10], [9], [25]. Cugat et. al. [11] discuss the scaling of the two types of magnetic actuators. The effect of improved current density in microcoils due to better heat dissipation is discussed. As the coils are scaled down by a factor k , the volume and the Joule heating reduce as k^3 , while the surface area and heat dissipation scale as k^2 . Thus current density up to 10,000 A/mm² can be tolerated in microscale coils, while mesoscale coils can tolerate only up to 10 A/mm². The scaling of magnetic actuators, taking into consideration the increased current densities, is shown in Figure 2-12.

Reduction factor $1/k$	magnet 	current 	iron 	induction $E = d\Phi / dt$ 	
magnet 	$\times k$ 	$\times k_1$ 	$\times k$ 	$/k$ \times frequency 	FFAs
current 	$\times k_1$ 	$\times k_{i1} \times k_{i2} / k$ 	$\times k_1 / k$ 	$\times k_1 / k^2$ \times frequency 	VFAs

Figure 2-12. Scaling of various magnetic interactions (used with permission) [5]

Here k is the scale factor by which the device is reduced and k_i is the factor by which the current density is increased at smaller scales. It can be seen that at smaller scales, electrodynamic transduction is advantageous.

To illustrate these effects, consider if all the dimensions of a fixed-field actuator are scaled by some factor s . The length scales by s . (Note k , described in Figure 2-12 is the “scale down” factor i.e. the device dimensions are divided by $k, s = \frac{1}{k}$). The current through the coil is the product of the volume current density (J) and the cross-section area (A). Thus if the current density is held constant, the total current scales as s^2 . As the gap and magnetic components both scale by the same factor, the flux density remains constant. Thus the force per unit volume of the device will stay constant as the device is scaled as shown below

$$\begin{aligned}
 F &= BLI = BL(JA) \\
 B, J &\rightarrow \text{constant} \\
 L \propto s, A \propto s^2, V \propto s^3 &. \\
 \frac{F}{V} &\rightarrow \text{constant}
 \end{aligned} \tag{2.27}$$

If the current density is assumed to increase by a factor of k_i ($k_i > 1$) as the device is scaled down, the force scaling changes slightly as shown below

$$\begin{aligned}
 F &= BLI = BL(JA) \\
 B &\rightarrow \text{constant} \\
 J \propto k_i &. \\
 L \propto s, A \propto s^2, V \propto s^3 &. \\
 \frac{F}{V} &\rightarrow k_i
 \end{aligned} \tag{2.28}$$

Thus force per unit volume increases by the same factor as the increase in the current density.

The force generated by a variable-field actuator is given by (2.23). Scaling analysis by assuming constant volume current density (J), is shown below

$$\begin{aligned}
F &= \nabla W_{mag} = \nabla \frac{(NI)^2}{\mathfrak{R}} = \nabla \frac{(NJA)^2}{\mathfrak{R}} \\
N, J &\rightarrow \text{constant} \\
\mathfrak{R} &\propto \frac{l}{A} \propto \frac{1}{s} \\
F &\propto s^4 \\
\frac{F}{V} &\rightarrow s
\end{aligned} \tag{2.29}$$

It is seen that the when variable-field actuators are scaled down ($s < 1$), the force per unit volume reduces. Thus, the scaling of these actuators with constant current density does not provide any performance improvement. If the current density is assumed to be increased, an improvement in force per unit volume can be expected as shown

$$\begin{aligned}
F &= \nabla W_{mag} = \nabla \frac{(NI)^2}{R} = \nabla \frac{(NJA_c)^2}{R} \\
N &\rightarrow \text{constant} \\
J &\propto k_i \\
R &\propto \frac{l}{A} \propto \frac{1}{s} \\
F &\propto s^4 \\
\frac{F}{V} &\rightarrow s * k_i
\end{aligned} \tag{2.30}$$

Thus, it may be possible to achieve improved force per unit volume in ($s * k_i > 1$).

In summary, qualitative scaling laws in the literature indicate that fixed-field actuators (interactions between a magnet and a coil) scale the best amongst all the magnetic interactions, and furthermore magnetic actuators may offer advantages over other actuation schemes. Variable-field actuators using the interaction between soft magnet and current do not scale well as the devices are made smaller.

These scaling analyses only account for the scaling of the transduction scheme itself. The overall scaling of the actuator including the mechanical components is also necessary to understand the physics of the entire device. In order to study the effects of scaling of the entire

actuator, accurate models of various components are required. Chapter 3 develops the lumped element models for all the components of an electrodynamic ZNMF actuator and some design trends and tradeoffs are discussed in Chapter 5.

2.5 Magnetic Actuators

This section presents an overview of magnetic actuators in general followed by a review of several ZNMF actuators reported in the literature so far. Section 2.5.2 discusses several modeling efforts related to ZNMF actuators including low-order analytical techniques as well as numerical approaches.

Magnetic actuators have been around for over a hundred years. The most common applications of magnetic actuators are loudspeakers, magnetic relays, switches, and solenoids. A typical design for an electrodynamic ZNMF actuator is essentially a loudspeaker with a cavity on the front and a slot (or orifice) through which the jet is formed. The purpose of an acoustic loudspeaker is to effectively radiate sound over the audio-range of frequencies (20 Hz – 20 kHz). In contrast, the purpose of a ZNMF actuator is to achieve large volume velocity displacements to form a strong jet through the slot (or orifice). The frequency of interest is also usually much lower, from 10 Hz – 500 Hz. Although these are slightly different requirements, both the actuators need to produce large displacement of the mechanical component.

A basic moving-coil (fixed-field) loudspeaker is shown in Figure 2-13. The major components of the loudspeaker are magnet assembly and voice coil, speaker cone and the spider. The soft magnet and the annular hard magnet generate a radial field in the air gap. The interaction between the current in the voice-coil and the magnetic field produces a force. The coil is attached to the speaker cone by means of the corrugated membrane and the spider. These two components determine the mechanical compliance of the device.

The magnetic assembly and the voice-coil that form the driving mechanism of the loudspeaker shown here, use an annular hard magnet. However, other magnetic circuit topologies can be used to achieve the radial field in the gap. An alternative magnetic circuit is shown in Figure 2-10 where a cylindrical hard magnet is used in the central leg of the magnetic circuit. An annular soft magnet forms the return path. The choice of the magnetic topology is based on various considerations – magnet performance, weight, ease of manufacturing, cost, etc.

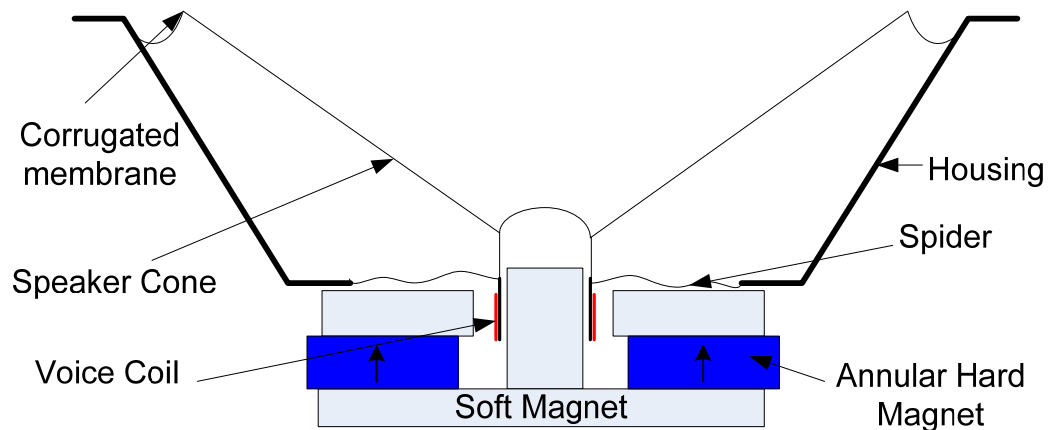


Figure 2-13. Cross-section of a typical moving coil speaker

2.5.1 Reported Zero-Net Mass-Flux Actuators

ZNMF actuators have been studied for various applications such as flow control, mixing enhancement and thermal management. Various transduction schemes—piezoelectric, electrostatic and magnetic—have been used to implement ZNMF actuators over a wide size ranges. Most efforts in the fluids community have focused on the modeling of the jets and studying their impacts on various flow situations. There are numerous studies that have concentrated on the visualization, and/or measurements of ZNMF actuators as well. This section discusses some of the mesoscale as well as microscale ZNMF actuators reported in the literature.

Coe et al. [26] reported a micromachined electrostatic ZNMF actuator array (Figure 2-14). The membrane consisted of metalized polyimide released using anisotropic potassium hydroxide

etch and sacrificial nickel layer. The membrane was 4 mm wide while the orifice opening was 50–800 μm . Voltage could be applied to individual membranes to actuate them. Typical velocity of 20 m/s was obtained from these jets.

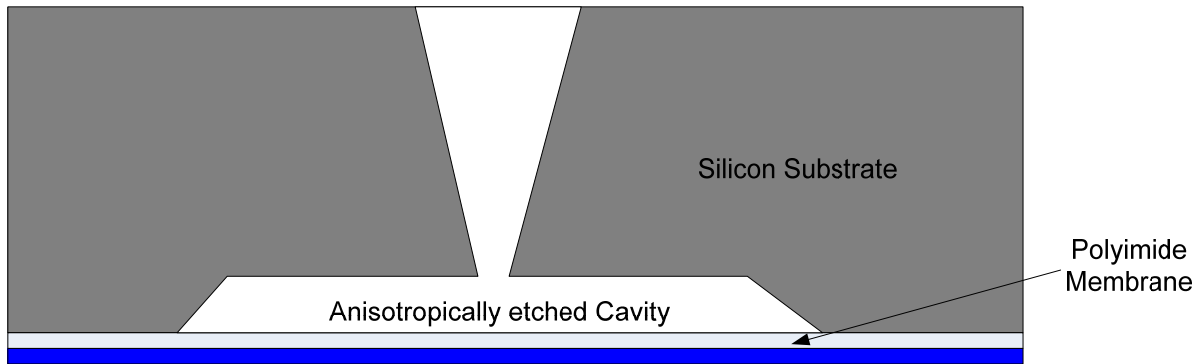


Figure 2-14. Integrated micromachined electrostatic ZNMF actuator adapter from Coe et al. [26]

Smith et al. [2] tested a mesoscale piezoelectric ZNMF actuator resulting in a two dimensional jet through a slot 75 mm long and 0.5 mm wide slot (Figure 2-15). Typical velocities up to 20 m/s were obtained. The frequency range of operation of this particular ZNMF actuator was 10 Hz – 100 Hz.

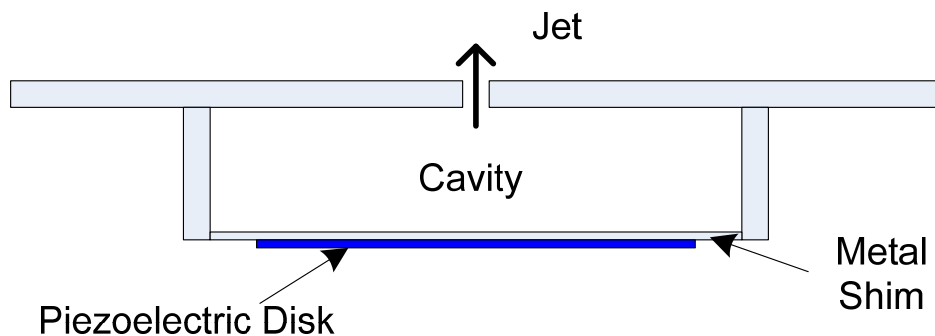


Figure 2-15. Mesoscale piezoelectric ZNMF actuator adapted from Smith et al. [2]

There have been very few magnetic-field-based ZNMF actuators reported in the literature so far. McCormick [3] demonstrated a mesoscale fixed-field ZNMF actuator and developed a lumped element model of the device to predict its performance (Figure 2-16). The model

predicted the cavity pressure as well as the output velocity accurately. The peak performance of the actuator was observed at about 100 Hz and the maximum frequency of operation was 400 Hz.

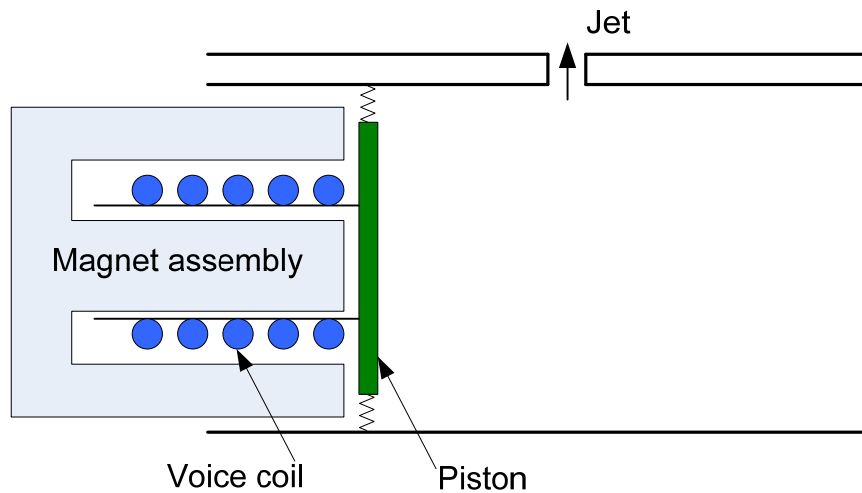


Figure 2-16. Fixed field (electrodynamics) ZNMF actuator adapted from McCormick [3]

Gallas et al. [14] reported a mesoscale piezoelectric ZNMF actuator. The structure of the device is similar to the one shown in Figure 2-15. The major focus of the work was to develop detailed coupled equivalent circuit model for the actuator based on lumped element modeling technique. The overall diameter of the actuators was less than 50 mm and maximum velocities of about 60 m/s was obtained at resonant frequency of 800 Hz.

Mossi et al. [27] investigated three different piezoelectric ZNMF actuators – a unimorph disc, a bimorph disc and a radial field disk. The overall diameter of the actuator in case was about 10 mm. Maximum velocities of 30 m/s were achieved for bimorph actuators. Typical operating frequency was about 500 Hz.

Parviz et al. [28] demonstrated the use of micromachined electrostatic ZNMF actuators as a propulsion mechanism for micro air vehicles (Figure 2-17). The overall width of the diaphragm was 1.2 mm and the predicted output velocity was 16 m/s at about 60 kHz.

Liang et al. [29] used ferromagnetic shape memory alloy composite (FSMA) diaphragm and an electromagnet to implement a ZNMF actuator for active flow control applications (Figure 2-18). A maximum velocity of 190 m/s was achieved at 220 Hz.

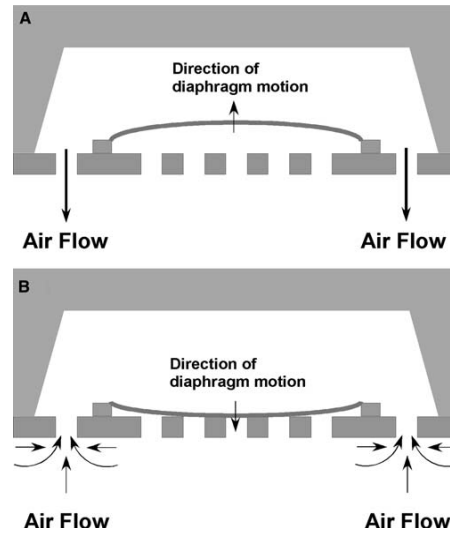


Figure 2-17. Integrated micromachined electrostatic ZNMF actuator demonstrated by Parviz et al. [28] (used with permission)

Yong et al. [4] used a microscale electrodynamic ZNMF actuator on printed circuit boards to achieve better cooling (Figure 2-19). The device is fabricated in the back side of the substrate using a lamination process for the fluidic components. The diaphragm is made out a fluoroelastomer. A bulk samarium-cobalt magnet and a copper coil form the actuation mechanism. A peak jet velocity of 14 m/s was achieved for input power of 60 mW.

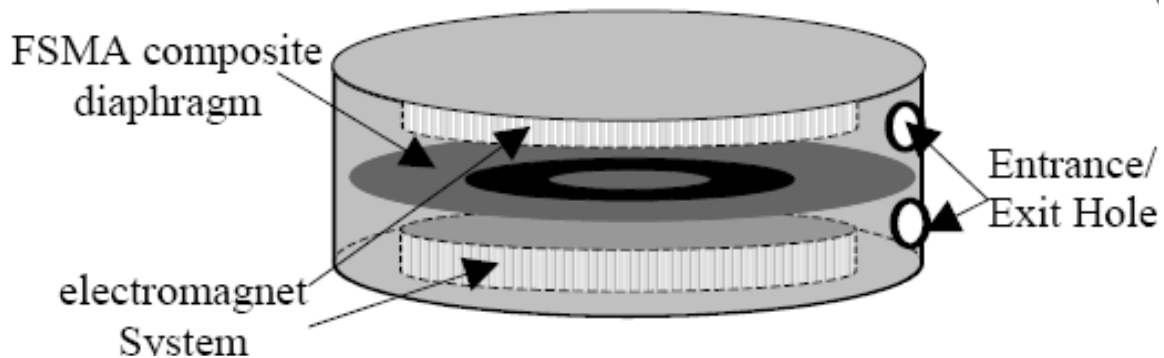


Figure 2-18. FSMA based ZNMF actuator reported by Liang et al. [30] (used with permission)

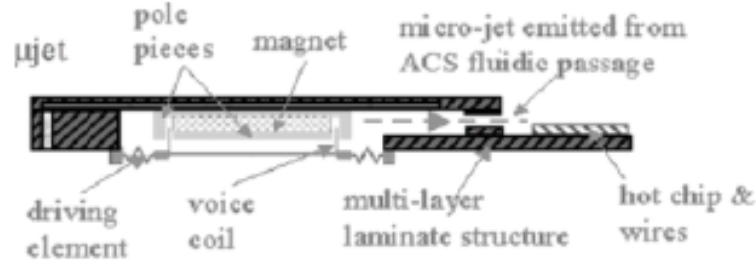


Figure 2-19. On chip electrodynamic ZNMF actuator for cooling reported by Yong et al.[4] (used with permission)

Lee et al. [31] reported an ionic-polymer metal composite driven ZNMF pump for a MAV application. The device was 10 mm diameter diaphragm and achieved 0.96 mm center displacement and 8 – 12 m/s output velocity for 2V input. The resonant frequency of the actuator was about 100 Hz.

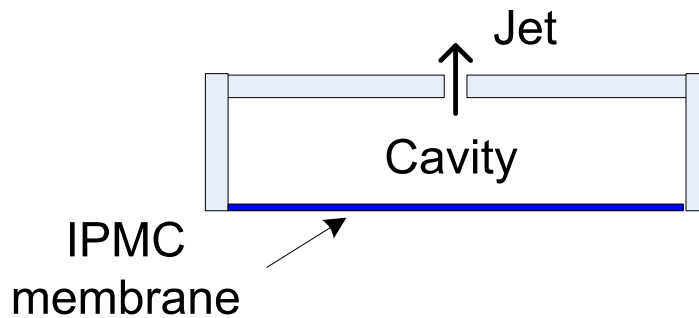


Figure 2-20. IPMC driven ZNMF actuator adapted from Lee et al. [31]

A summary of various ZNMF actuators discussed here is provided in Table 2-3.

Several other ZNMF actuators have been reported on the literature for various applications. Gordon et al. [32] studied the effects use of an electrodynamic ZNMF actuator on the surrounding flow. The actuator was a modified commercial electrodynamic speaker. Campbell et al. [33] used electrodynamic ZNMF actuators to achieve cooling of electronic components. They report lowering of the temperature of processor chip 22 % for a test case. However, no details of the actuator are provided.

Hong et al. [34] used a piezoceramic based ZNMF actuator for laminar flow separation. A similar device was also used by Lee et al. [35] for boundary layer flow control. Several other piezoelectric ZNMF actuators have been reported for full flight applications as well. [36, 37]. Tian et al. [38] used piezoelectric ZNMF actuators in conjunction with pressure transducers to implement closed-loop control for separation control over an air-foil.

Table 2-3. Summary of ZNMF actuators reviewed

Year	Author	Transduction Mechanism	Notes
1995	Coe et al.[26]	Electrostatic	Micromachined device, typical velocity ~ 20 m/s
1998	Smith et al. [2]	Piezoelectric	Mesoscale device, typical velocity ~ 20 m/s, Bandwidth 10 Hz – 100 Hz
2000	McCormick et al. [3]	Fixed-field actuator (Electrodynamic)	Up to 30 m/s velocity for 5 W input power, Bandwidth 100 Hz – 400 Hz
2003	Gallas et al. [14]	Piezoelectric	Mesoscale device (~ 50 mm), typical velocity 60 m/s at 800 Hz
2004	Mossi et al. [27]	Piezoelectric	Different types of piezoelectric drivers studied. Maximum velocity ~ 30 m/s
2005	Parviz et al. [28]	Electrostatic	Micromachined device, typical velocity ~ 16 m/s @ 60 kHz
2005	Liang et al. [29]	Variable-field actuator	Mesoscale device, typical velocity 190 m/s @ 220 Hz
2005	Yong et al. [4]	Fixed-field actuator	On chip cooling device, velocity of 14 m/s, Resonant frequency 100 Hz
2006	Lee et al. [31]	IPMC driven	Micro-air vehicle application, ~ 12 m/s velocity, Resonant frequency ~ 100 Hz

In spite of several efforts on applications and effects of ZNMF actuators on the surrounding flow detailed discussion of design and fabrication of the actuators themselves has been missing. This work presents a systematic approach to design an electrodynamic ZNMF actuators to meet the necessary target specifications of the application such as output velocity, bandwidth, maximum power consumption.

2.5.2 Modeling of Zero-Net Mass-Flux Actuators

In order to design and optimize ZNMF actuators, accurate models are necessary. Surprisingly, very few analytical models for ZNMF actuators have been reported. McCormick et al. [3] modeled the coupling between the electrical and mechanical domain as an ideal gyrator. The diaphragm is modeled as a mass-spring-damper system. The cavity and orifice are modeled using the lumped element modeling approach as will be discussed in Chapter 3. The model was verified by comparing the predicted cavity pressure with experimental results at several different input levels and frequencies. There was very good agreement between the model and experimental results.

Gallas et al. [14] also used a similar approach to model piezoelectric ZNMF actuator. The coupling between the electrical and the mechanical domain was modeled as an ideal transformer. The piezoelectric disc was modeled as a clamped composite circular plate. The cavity and orifice models used were similar to the ones used by McCormick et al. [3]. The model for the composite plate and the acoustic cavity were verified individually. The output velocity generated by the jet was measured using hotwire anemometer and compared with the model predictions. The model predicted the output velocity very well over the entire range of frequencies of interest.

Most other modeling approaches have used numerical techniques to model the flow physics of a ZNMF actuator. Several reduced-order models have been developed to reduce the computational requirements. Kral et al. [15] simulated a single ZNMF actuator for a two-dimensional, incompressible case. Instead of simulating the actuator and the cavity, they used a sinusoidal velocity profile as a boundary condition at the entrance of the orifice. The results of the simulations indicated that some of the experimentally observed phenomena were not entirely captured by using just the sinusoidal velocity boundary condition. Rizetta et al. [16] used a decoupling approach to solve the compressible Navier-Stokes equations inside and outside the

cavity. For the cavity simulations, oscillating boundary conditions was used on one of the cavity surfaces. The external flow field was calculated using recorded exit velocity profiles from the jet as the boundary. Thus simultaneous simulations of the flow field inside and outside the cavity were not necessary.

Several other modeling efforts have also focused on detailed modeling of the cavity and the slot that form important components of the actuator. This work will focus on lumped element modeling based approach similar to that used by McCormick et al. [3]. Detailed models of individual components – electrodynamic coupling, diaphragm, cavity and the orifice – are developed in Chapter 3.

CHAPTER 3 LUMPED ELEMENT MODELING

Chapter 3 discusses the low-order, lumped element modeling of a fixed-field (electrodynamic) zero-net mass-flux (ZNMF) actuator. This modeling approach is useful for design and optimization of the device. The basic assumptions involved in the lumped element approach are described in section 3.1, followed by an overview of conjugate power variables. The overall structure of the ZNMF actuator and the lumped element model is discussed in section 3.2. The subsequent sections present each component of the lumped element model in detail. Section 3.3 develops the model for the electrodynamic transduction scheme. The model for the moving coil/diaphragm assembly is presented in section 3.4. Finally, the acoustic models for the cavity and the slot (or orifice) are discussed in section 3.5. The transfer function relating the input electrical excitation and output average velocity is derived in section 3.6.

3.1 Lumped Element Modeling Basics

The inherent assumption of lumped element modeling (LEM) is that the length scale of the device (d) is much smaller than wavelength (λ) of the physical phenomenon governing the device [12], [13]. In such a case, the governing partial differential equations of the system may be simplified to ordinary differential equations. For example, the wave equation governs various physical phenomenon such as acoustic, electromagnetic (EM), and mechanical membrane/string vibration phenomena. Consider the wave equation with h as the independent variable,

$$\frac{1}{c^2} \frac{\partial^2 h}{\partial t^2} = \nabla^2 h, \quad (0.31)$$

where c is the speed of propagation of the wave. For harmonic motion at frequency ω , the left hand side of (0.31) scales as

$$\frac{1}{c^2} \frac{\partial^2 h}{\partial t^2} \propto \frac{h\omega^2}{c^2} = h \left(\frac{2\pi}{\lambda} \right)^2. \quad (3.32)$$

If the largest length scale of interest is d , the spatial derivative on the right hand side scales as

$$\nabla^2 h \propto \frac{h}{d^2}. \quad (3.33)$$

The spatial variation and the time variations can be decoupled if

$$\frac{1}{c^2} \frac{\partial^2 h}{\partial t^2} \ll \nabla^2 h. \quad (3.34)$$

Substituting by the relevant scaling parameters, (3.4) can be represented

$$h \left(\frac{2\pi}{\lambda} \right)^2 \ll \frac{h}{d^2}. \quad (3.35)$$

Thus, when the wavelength of the governing physical phenomenon is much greater than the length scale of interest ($\lambda \gg d$), the spatial variations can be analyzed independent of the time harmonic temporal variations. The distributed spatial quantities of interest can then be “lumped” at a reference location, and the time-dependence of these quantities can be studied independently. In the case of an electrodynamic ZNMF actuator, the maximum frequency of interest is about 500 Hz, and the acoustic wavelength at this frequency is about 0.7 m. Thus, if the size of devices considered is much smaller than 0.1 m, the lumped assumption is valid. Note that the electrical wavelength is much larger than the acoustic wavelength and hence the acoustic wavelength is the more limiting factor. The lumped assumption is also valid for the diffusion equation and the bending wave equation.

3.1.1 Passive Lumped Elements

Lumped element modeling is used to capture the energy behavior of various components of any system and represent it as electrical circuit. The overall behavior of the system can then be predicted by using standard circuit analysis techniques. Within such a circuit model, a passive *lumped element* is used to represent each individual energy storage/dissipation mechanism in the device. Every lumped element has an “effort” (e) and a “flow” (f) variable associated with it (Figure 3-1) [13]. The product of the effort and flow variables in each of the domains is power, with units of Watts. The effort and flow variables are hence called conjugate power variables.

Note the sign convention used is such that the terminal through which the flow variable f enters is defined as the positive terminal and vice versa. Thus by convention, the power absorbed by the lumped element (power going into the element) is defined to be positive. The effort and flow variables in various energy domains of interest are shown in Table 3-1.

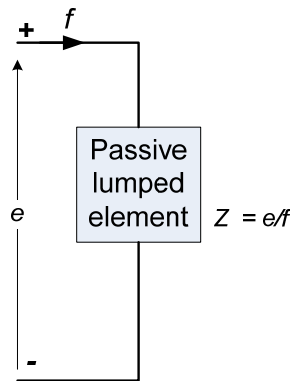


Figure 3-1. Passive lumped element

Table 3-1. Effort and flow variables in various energy domains

Domain	Effort E	Flow f
Electrical	Voltage (V)	Current (I)
Mechanical	Force (F)	Velocity (U)
Acoustic/Fluidic	Pressure (P)	Volume velocity (Q)

To build a lumped element model for a dynamic system, the energy storage and dissipation mechanisms of the system must be identified and modeled using three different passive lumped elements. A generalized resistance (resistor) represents dissipation of energy in the form of heat. Kinetic energy storage is represented as a generalized inertance (inductor), while potential energy storage is represented as a generalized compliance (capacitor). The impedance Z of a passive element is defined as

$$Z = \frac{e}{f}. \quad (3.36)$$

Thus electrical impedance is the ratio of voltage and current with units of V/A or Ω . Mechanical impedance is defined as the ratio of force to velocity and has units of $(N\cdot s)/m$. Acoustic

impedance, the ratio of pressure to volume velocity, has the units of $N\cdot s/m^5$. Table 3-2 summarizes the lumped parameters in different energy domains.

Table 3-2. Passive lumped element components in various energy domains

Domain	Generalized resistance	Generalized inertance	Generalized compliance
Energy behavior	Dissipation	Kinetic energy Storage	Potential energy storage
Electrical	Resistance (Ω)	Inductance (H)	Capacitance (F)
Mechanical	Damping Factor ($N\cdot s/m$)	Mass (kg)	Compliance (m/N)
Acoustic	Acoustic resistance ($N\cdot s/m^5$)	Acoustic mass (kg/m^4)	Acoustic compliance (m^5/N)

3.1.2 Two-Port Elements

In addition to the one-port lumped elements, two-port elements may be used to represent the energy coupling between different energy domains or to represent impedance transformations within a single domain. The two most common two-port circuit elements used for transducer modeling are transformers and gyrators. Ideal transformers and gyrators do not store or dissipate energy; they just convert energy from one energy domain to another. A transformer is used when the effort variables in the two energy domains are proportional to each other, while a gyrator is used when the effort variable in one domain is proportional to the flow variable in the other. Figure 3-2 shows the two circuit elements with standard conventions. The transformer equations are given as

$$\begin{pmatrix} E_2 \\ F_2 \end{pmatrix} = \begin{pmatrix} T & 0 \\ 0 & \frac{1}{T} \end{pmatrix} \begin{pmatrix} E_1 \\ F_1 \end{pmatrix}. \quad (3.37)$$

Similarly gyrator equations are given as

$$\begin{pmatrix} E_2 \\ F_2 \end{pmatrix} = \begin{pmatrix} 0 & G \\ \frac{1}{G} & 0 \end{pmatrix} \begin{pmatrix} E_1 \\ F_1 \end{pmatrix}, \quad (3.38)$$

where T and G are transduction coefficients that represent the coupling between the two energy domains. It can be seen that the power in both the domains is equal, that is $E_1F_1 = E_2F_2$.

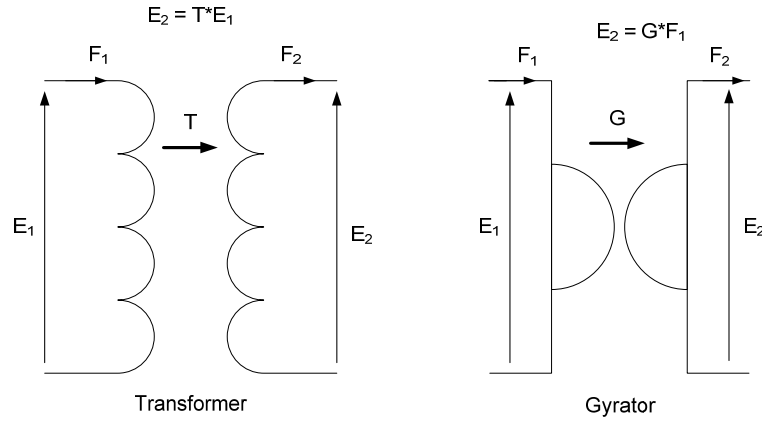


Figure 3-2. Ideal transformer and gyrator two-port circuit elements

For circuit analysis, it is often convenient to simplify a circuit by eliminating the transformer or gyrator; this is accomplished by reflecting circuit elements from one side of the transformer or gyrator to the other, as described below. Consider the transformer with impedance Z_2 connected to the second energy domain as shown in Figure 3-3. The effort variable E_2 in the second domain is given by

$$E_2 = TE_1 = Z_2F_2. \quad (3.39)$$

The relationship between the effort and flow variable in the first domain is thus given by

$$E_1 = \frac{Z_2}{T^2} F_1. \quad (3.40)$$

Thus Z_2/T^2 is the equivalent or “referred” impedance in the first domain as shown in the figure.

The impedance transformation for a transformer is reciprocal. In other words, if an impedance Z_1 is connected in the first domain the equivalent impedance in the second domain is Z_1/T^2 .

Moreover, an effort source V_2 connected in the second energy domain, can be replaced by an equivalent effort source V_2' in the first energy domain given by

$$V_2' = \frac{V_2}{T}. \quad (3.41)$$

Note that the source transformation is also reciprocal. Thus an effort source V_1 in the first energy domain, is equivalent to an effort source $V_2' = TV_1$ in the second energy domain. A flow source transformation can be performed in a similar manner.

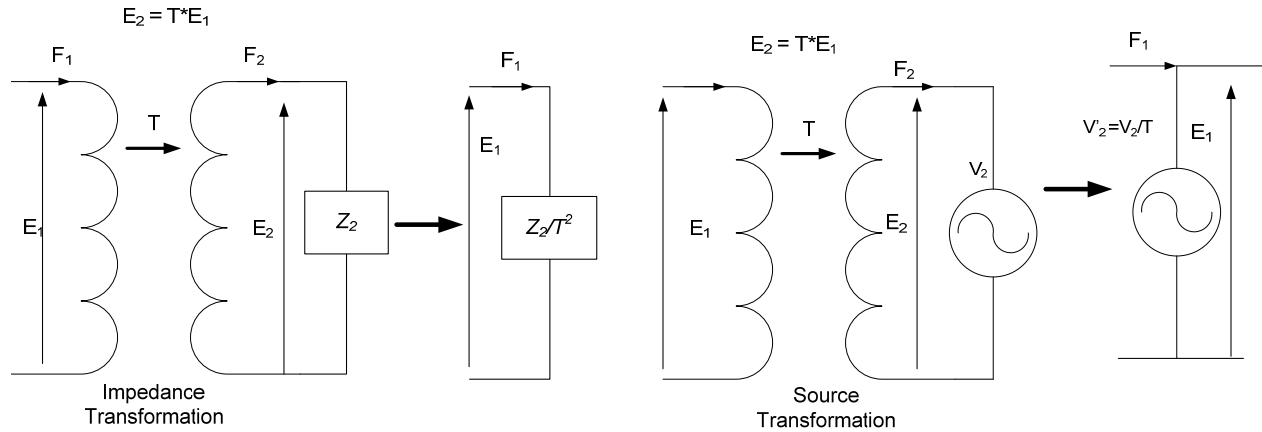


Figure 3-3. Impedance and source transformation using a transformer

Impedance transformation from one energy domain to the other when a gyrator is used is now discussed. Consider impedance Z_2 connected in the second energy domain as shown in Figure 3-4.

The effort variable E_2 in the second energy domain is given by

$$E_2 = F_2 Z_2 = G F_1. \quad (3.42)$$

The effort variable E_1 in the first domain is given by

$$E_1 = G F_2 = G \frac{G F_1}{Z_2} = \frac{G^2}{Z_2} F_1. \quad (3.43)$$

Thus it can be seen that the equivalent impedance in the first domain is $Z_2' = G^2/Z_2$. Note that the

original impedance is in the denominator; thus if a capacitive load is connected in the second energy domain, the equivalent impedance “seen” by the first energy domain is inductive, and

vice versa. As gyrator represents relationship between an effort variable in one domain to a flow variable in the other domain, when an effort source is connected on one side establishes a flow

on the other side or vice versa. Thus, an effort source V_2 connected in the second energy domain is equivalent to a flow source given by $I_1' = V_2/G$ as shown in Figure 3-4. Note that, as in the case of a transformer, the impedance and source transformations due to a gyrator are also reciprocal.

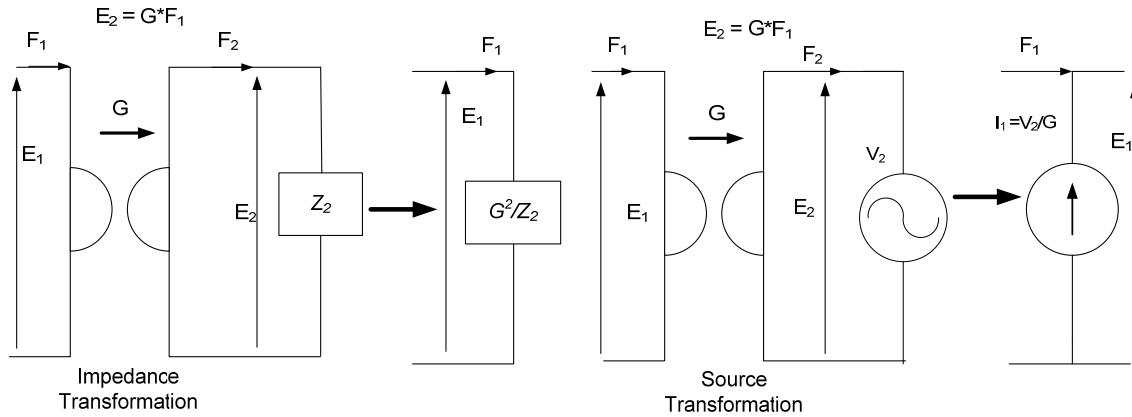


Figure 3-4. Impedance and source transformations using a gyrator

3.2 Lumped Element Model of Electrodynamics ZNMF Actuator

A schematic drawing of an electrodynamic ZNMF actuator is shown in Figure 3-5. A circular diaphragm of radius a is attached to a current carrying coil. The circular diaphragm forms the bottom portion of a cavity. The top of the cavity is bound by a rigid plate containing a slot or a circular orifice (an axisymmetric orifice is shown in the schematic).

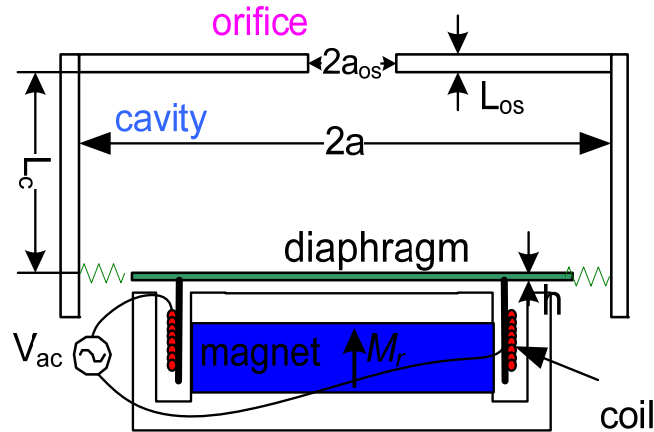


Figure 3-5. Schematic of electrodynamic ZNMF actuator.

The magnetic assembly generates a uniform radial magnetic flux density B in the annular air gap. A solenoidal coil of total length L_{coil} resides in the magnetic gap and is rigidly attached to the diaphragm. The diaphragm is driven into motion due to the Lorentz force acting on the coil when a current is passed through it. The oscillatory motion of the diaphragm causes the fluid in the cavity to be expelled or injected, forming the synthetic jet. Thus it can be seen that, large displacement of the diaphragm will result in large volume of fluid being moved and large output velocity (ignoring compressibility effects in the cavity).

The electrodynamic ZNMF actuator has two different energy domains – electrical (magnet, coil) and acoustic (diaphragm, cavity and slot/orifice). Note that the magnetic energy domain is not represented as a separate domain explicitly within the system-level LEM. The magnetic domain is modeled separately to predict the magnetic fields necessary for the electrodynamic coupling between the electrical and acoustic domain.

Figure 3-6 shows the complete lumped element model of the ZNMF actuator, which will be developed in detail throughout Chapter 3, but introduced briefly here first. In the circuit model nomenclature, the first subscript denotes the domain (“ a ” for acoustic and “ e ” for electric), and the second subscript describes the component (“ C ” for coil, “ D ” for diaphragm, “ Cav ” for cavity, and “ OS ” for the orifice or slot). Beginning on the left side of the circuit, the electrical impedance of the coil is represented as a resistor R_{eC} and inductor L_{eC} in series ($Z_{eC} = R_{eC} + j\omega L_{eC}$). A gyrator is used to represent the electrodynamic coupling between the electrical and acoustic domains. Everything to the right of the gyrator is in the acoustic domain, where the effort variable is pressure, and the flow variable is volume velocity. The potential and kinetic energy storage in the diaphragm is represented as an acoustic compliance C_{aD} , and an acoustic mass M_{aD} respectively. All the energy losses in the diaphragm – support losses, viscous

losses due to the diaphragm motion, structural losses etc. are represented as an acoustic damping resistance R_{aD} . The compression or expansion of fluid in the cavity results in storage of potential energy and this is denoted as an acoustic compliance C_{aCav} . Note that the back cavity formed by the housing, annular gap in the magnetic assembly also adds an additional compliance. However, for all the devices considered in this work, the back cavity volume is much larger and hence the corresponding impedance is much smaller than the impedance of the front cavity. This assumption will be validated in Chapter 4 where the characterization of these actuators is discussed.

The losses in the slot (or the orifice) are modeled as a combination of linear (R_{aOS} and R_{aRad}) and nonlinear (R_{aO}) resistors. R_{aOS} and R_{aO} represent the viscous losses along the walls and the corners of the slot (or orifice) and R_{aRad} represents the losses due to radiation of sound from the slot (or orifice) into the semi-infinite medium. The kinetic energy storage in the slot (or orifice) due to the physical motion of the fluid is represented by acoustic masses M_{aOS} and M_{aRad} .

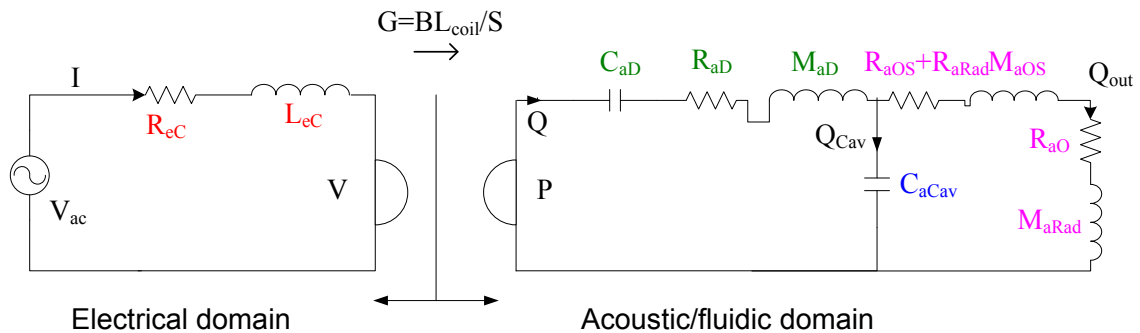


Figure 3-6. Lumped element model of the electrodynamic ZNMF actuator

The interconnections (series/parallel) of the lumped elements are determined by their energy sharing behavior. Elements that share common flow through their terminals (current or volume velocity) are connected in series, whereas elements that share common effort across their terminals (voltage or pressure) are connected in parallel. In operation, the equivalent acoustic

pressure acts on the diaphragm and causes its motion. The motion of the diaphragm results in compression (or expansion) of the fluid in the cavity and expulsion (or suction) of fluid through the slot or the orifice. Thus the cavity and slot share the same effort variable (pressure) and are connected in parallel as shown.

Once the equivalent circuit model is established many relevant system performance parameters can be determined. The following sections will present the models for each individual components of the lumped circuit model.

3.3 Electrodynamic Transduction

Electrodynamic or fixed-field transduction usually involves the interaction between a current carrying coil and the field from a hard magnet as discussed in section 2.3.1. One primary assumption is that the overall magnetic field distribution in the device does not change significantly during the device operation. Specifically, this implies (i) the magnetic fields arising from current flow in the coil are small compared to the static magnetic field from the magnetic assembly and (ii) the motion of the coil/diaphragm assembly does not alter the magnetic field. Note, this does not imply the magnetic field is uniform, but this assumption is often required to ensure a constant transduction factor and thus linear operation.

In the most general case, the differential Lorentz force $d\vec{F}$ on a small volume element dV of a conductor is given by

$$d\vec{F} = \vec{J} \times \vec{B} \quad (3.44)$$

where \vec{J} is the current density in A/m^2 and \vec{B} is the magnetic flux density. The total force is calculated by integrating $d\vec{F}$ over the volume of the conductor.

The model for electrodynamic transduction scheme developed here is an idealized case where it is assumed that the current density J and the magnetic flux density B are constant and that the coil is perpendicular to the direction of the magnetic field. The cross-sectional area of the

coil is A_{coil} and overall length of the coil is L_{coil} . Thus Lorentz force F acting on the coil, subjected to constant magnetic flux density B is [21]

$$F = \int_V (\vec{J} \times \vec{B}) dV = JBA_{coil}L_{coil} = BL_{coil}I. \quad (3.45)$$

The force produced is in the direction normal to both the current and the field according to the right-hand rule as shown in Figure 3-7. The electromechanical transduction coefficient BL_{coil} is a measure of the coupling between the two energy domains. For an actuator, it should be as large as possible to achieve maximum force for a given input current.

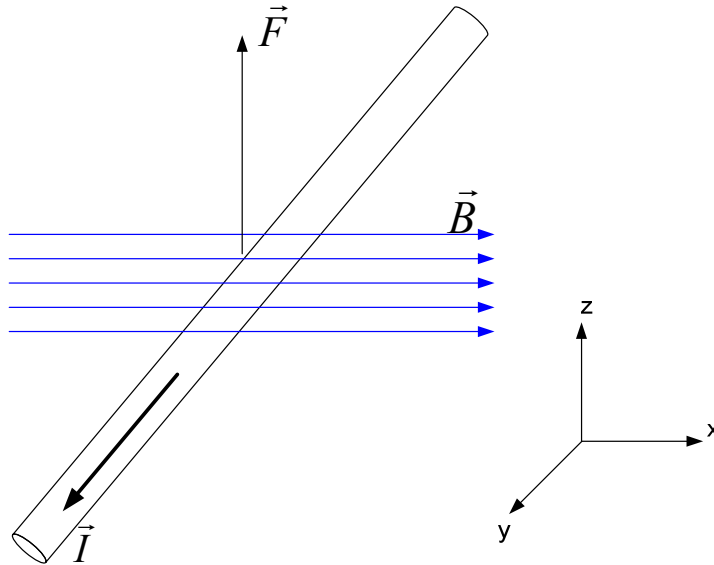


Figure 3-7. Lorentz force on a current carrying coil in a magnetic field

The electrodynamic coupling is anti-reciprocal. In other words, a conductor moving in the presence of a magnetic field will have a voltage induced across it [21]. But the direction of voltage induced is negative as per the standard sign conventions. This can be deduced from the Faraday's law given by

$$V = -\frac{\partial \phi}{\partial t} = -\frac{\partial (BA)}{\partial t} \quad (3.46)$$

where V is the induced voltage and Φ is the magnetic flux given by the product of the magnetic flux density and the area of coil loop (note not the cross-section area of the coil). Consider a coil

loop of length L_{coil} , moving with velocity U in a homogenous magnetic flux density B as shown in Figure 3-8. The free electrons in the coil as given by the Lorentz force equation

($F = q(\vec{U} \times \vec{B})$), where q is the charge of the electron. This “magnetic force” can be represented as that exerted by an electric field

$$\vec{E} = \vec{U} \times \vec{B}. \quad (3.47)$$

This electric field is called “motional electric field” [39] and the direction of this field is perpendicular to both the velocity and the magnetic flux density. This electric field induces a voltage called the “motional emf” across the two terminals of the wire given by the line integral of the electric field as shown below

$$V = \int_2^1 (\vec{U} \times \vec{B}) \cdot d\vec{l}, \quad (3.48)$$

where 1 and 2 indicate the two terminals of the wire. For the case shown in the figure, the velocity and the magnetic flux density are perpendicular to each other, thus the induced voltage is

$$V = -BL_{coil}U. \quad (3.49)$$

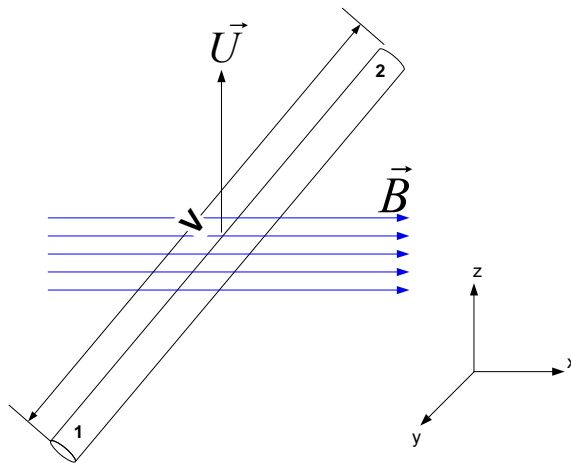


Figure 3-8. Voltage induced on a moving coil in a magnetic field

This combined interaction between the electrical and mechanical domains is represented in the matrix form as shown below (section 2.1)

$$\begin{bmatrix} F \\ V \end{bmatrix} = \begin{bmatrix} 0 & BL_{coil} \\ BL_{coil} & 0 \end{bmatrix} \begin{bmatrix} U \\ I \end{bmatrix}. \quad (3.50)$$

Note that the induced voltage is indicated as positive here. The implications of choosing this sign convention is discussed shortly.

In the overall lumped element model for the ZNMF actuator shown in Figure 3-6, the diaphragm, cavity and the slot (or orifice) are modeled in the acoustic domain. The Lorentz force acting on the coil can be converted to an equivalent pressure given by $P = F/S$, where S is the effective area of the diaphragm to which the coil is attached. Note that the effective area is used instead of the overall area of the diaphragm because the diaphragm displacement is not necessarily constant over the entire diaphragm. If the diaphragm displacement is constant over the entire diaphragm, then S is the overall area of the diaphragm. The combined interaction between the electrical and acoustic domains is shown below

$$\begin{bmatrix} P \\ V \end{bmatrix} = \begin{bmatrix} 0 & BL_{coil}/S \\ BL_{coil}/S & 0 \end{bmatrix} \begin{bmatrix} Q \\ I \end{bmatrix} \quad (3.51)$$

As discussed in section 2.1, it can be seen that the diagonal elements of the matrix are zero, and the electrodynamic transduction is a direct transduction scheme. However, it should be noted that the coil is always attached to a mechanical component (e.g. a diaphragm in the case of ZNMF actuator). Thus free displacement of the actuator as defined by (2.4) in Chapter 2 is not infinite. The free displacement is bounded by the impedance of the mechanical structure, which is completely independent of the electrodynamic transduction.

The two-port model for electrodynamic transduction using the gyrator representation is shown in Figure 3-9. The force produced in the mechanical domain (or the pressure in the acoustic domain) is directly proportional to the input current in the electrical domain, and the voltage produced in the electrical domain is directly proportional to the velocity in the mechanical domain (or the volume velocity in the acoustic domain). Thus electrodynamic transduction is linear (under the assumption that the transduction coefficient is constant with respect to displacement). Note that the gyrator representation is chosen throughout this thesis in order to use the impedance analogy [7]. A transformer representation can also be used. However, this will require the use of admittance analogy in one of the energy domains.

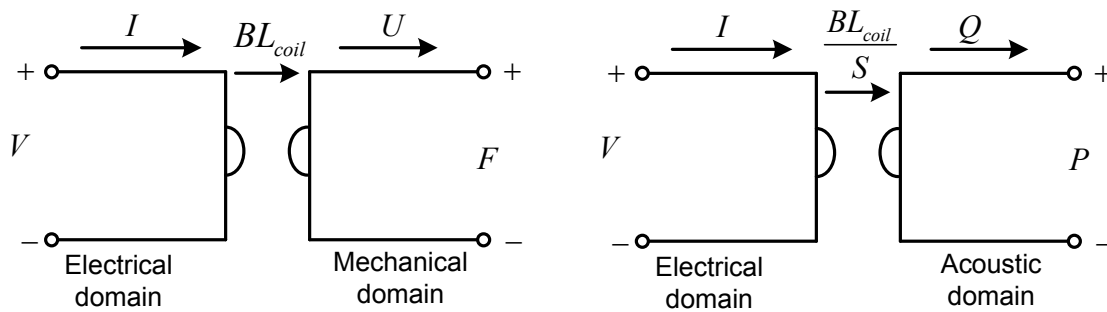


Figure 3-9. Two-port gyrator model of electrodynamic transduction

As discussed before, electrodynamic transduction scheme is “anti-reciprocal” or “antisymmetric” by definition, where the transduction coefficients are equal in magnitude but opposite in sign (3.48). This is a consequence of the sign conventions used in defining the various quantities for electrodynamic transduction [7]. From equations (3.44) and (3.46) the two transduction coefficients can be defined as

$$G_{me} = \frac{BL_{coil}}{S}, \quad G_{em} = -\frac{BL_{coil}}{S}. \quad (3.52)$$

However, by choosing appropriate sign convention, electrodynamic transduction can be represented as a reciprocal transduction scheme.

It can be seen that the assumptions of the constant current density and constant magnetic flux density are crucial to the electrodynamic transduction model developed here. For most cases (particularly for low frequencies), the assumption of constant current density through the coil is reasonable. However, the magnetic flux density B may vary along the length of the coil, and for actual wire conductors with non-zero diameters, the flux density may vary over the wire cross-section area. Moreover, as the coil and the magnet move with respect to each other during the device operation, the flux density changes with position. Hence, for more complex configurations, the magnetic field generated can be analyzed using finite element methods (FEM) to calculate the effective electromechanical transduction coefficient. The calculation of transduction coefficient using the 1-D circuit model and finite element simulations is discussed in the following sections.

3.3.1 Calculation of the Transduction Coefficient using 1-D Magnetic Circuit Model

The magnetic assembly of the electrodynamic ZNMF actuator consists of a hard magnet, a soft magnetic core and the air gap in which the coil resides. Figure 3-10 shows the schematic of the magnetic assembly and the equivalent 1-D circuit model. The 1-D magnetic circuit is used to predict the magnetic flux density in the air gap, which, combined with the length (and position) of the coil determines the transduction coefficient.

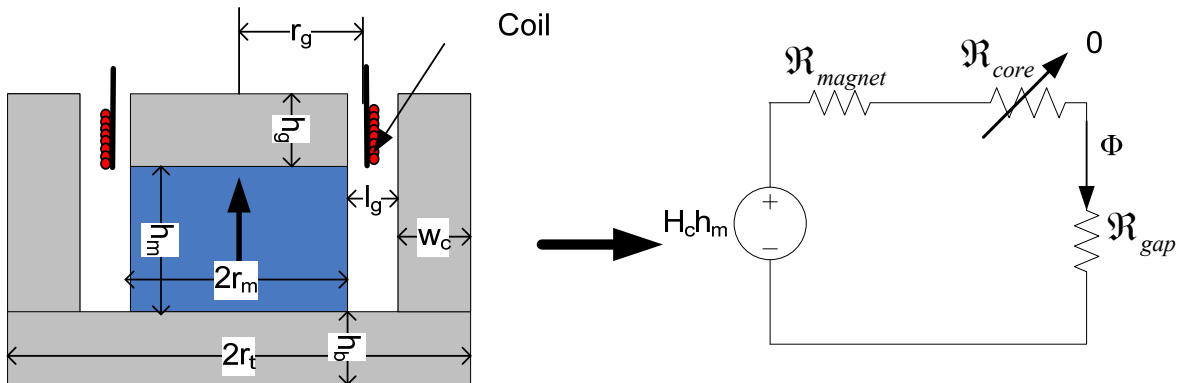


Figure 3-10. 1-D magnetic circuit approach

The 1-D magnetic circuit model is based on the integral form magnetostatic Maxwell's equations [24]. The key assumption involved in this approach is that the magnetic flux is entirely confined to the magnetic path. The entire magnetic path is represented as a *magnetic circuit* analogous to an electrical circuit as shown in Figure 3-10. The hard magnet acts as the source of the magnetic field. The soft magnetic core serves to guide the flux across the air-gap. The soft magnetic core and the air-gaps are represented in the magnetic model by their *magnetic reluctance* \mathfrak{R} , which is the “resistance” offered by the magnetic path to the flow of magnetic flux. Magnetic reluctance is a function of the geometry and the material and is given by

$$\mathfrak{R} = \frac{l}{\mu_0 \mu_r A}, \quad (4.53)$$

where l is the length of the magnetic path, A is the cross-sectional area through which magnetic flux flows, μ_0 is the magnetic permeability of free space and is given by 1.25×10^{-6} H/m and μ_r is the relative permeability of the material. For example, the reluctance of the magnet for the magnetic assembly in Figure 3-10 will be

$$\mathfrak{R}_{magnet} = \frac{h_m}{\mu_0 \mu_{magnet} A_{magnet}} = \frac{h_m}{\mu_0 \mu_{magnet} (\pi r_m^2)}, \quad (3.54)$$

where h_m is the height of the magnet, r_m is the radius of the magnet and for neodymium-iron-boron $\mu_{magnet} = 1.05$ [23]. Similar expressions can be obtained for the reluctance of the air gap. However, the magnetic flux in the air gap the flux is not restricted just to the cross-sectional area of the gap (Figure 3-11). This phenomenon is called “fringing.” The flux spreads out across a larger cross-section, and corrections are used to calculate the effective area and hence the reluctance of the air gap. The effective area for the annular air gap is given by [39]

$$A_{eff} = (h_g + l_g) \left(2\pi (r_g + l_g) \right). \quad (3.55)$$

The reluctance of the air gap is thus given by

$$\mathfrak{R}_{gap} = \frac{l_g}{\mu_0 A_{eff}} \quad (3.56)$$

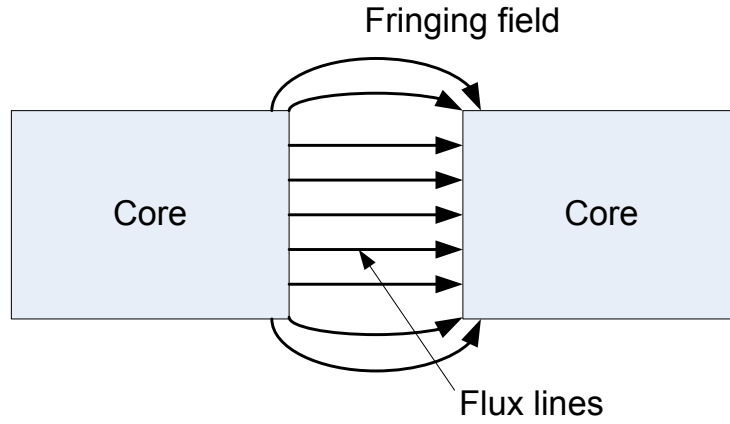


Figure 3-11. Fringing fields in the air gap

Note that the fringing field correction shown in (3.55) is only valid for cases where the area of the cross-section of the core on both sides of the air gap is the same and hence the fringing fields are symmetrical. In the case of the magnetic topology illustrated in Figure 3-10, the air gap is bounded by different core areas on the two sides, and hence the fringing fields will be asymmetric. The error introduced due this asymmetry is small as shall be shown using finite element analysis.

The reluctance of the core is composed of three different components – the bottom, the top and the annular portion. The reluctances of these components, along with the assumptions involved are detailed in Appendix A. The reluctance expressions for the three components are given below

$$\mathfrak{R}_{top} = \frac{h_g}{2\mu_{core}\pi r_m^2}, \quad (3.57)$$

$$\mathfrak{R}_{annular} = \frac{w_c + h_g}{\mu_{core}\pi \left((r_m + l_g + w_c)^2 - (r_m + l_g)^2 \right)}, \quad (3.58)$$

and

$$\mathfrak{R}_{bottom} = \frac{r_t}{2\mu_{core}\pi\left(r_m + l_g + \frac{w_c}{2}\right)h_g} \quad (3.59)$$

where μ_{core} is the permeability of the soft magnetic material used for the core. The overall core reluctance is the sum of these three components ($\mathfrak{R}_{core} = \mathfrak{R}_{top} + \mathfrak{R}_{annular} + \mathfrak{R}_{bottom}$). Note that the relative permeability of the soft magnetic core is usually extremely high ($\mu_{core} \sim 100000$) and hence the reluctance of the core is negligible as compared to that of the air gap and the magnet. This is discussed in detail in Appendix A.

The *magnetomotive force* (MMF) generated by the hard magnet is given by $MMF = H_c h_m$. Here H_c is the coercivity of the hard magnet and h_m is the height of the magnet. The coercivity H_c and the remnant magnetic flux density B_r of an ideal magnet (square M-H magnetic hysteresis loop) are related by

$$H_c = \frac{B_r}{\mu_0 \mu_{magnet}} \quad (3.60)$$

Thus the total flux Φ (in Weber) flowing through the gap is given by

$$\Phi = \frac{H_c h_m}{\mathfrak{R}_{magnet} + \mathfrak{R}_{core} + \mathfrak{R}_{gap}} \approx \frac{H_c h_m}{\mathfrak{R}_{magnet} + \mathfrak{R}_{gap}}. \quad (3.61)$$

The magnetic flux density in the air gap is thus calculated by dividing the flux with the cross-section area of the gap.

The magnetic flux density in the air gap B is thus given by

$$B = \frac{\Phi}{A_{eff}} = \frac{H_c h_m}{\left(\frac{h_m (h_g + l_g) (2\pi (r_g + l_g))}{\mu_0 \mu_{magnet} (\pi r_m^2)} + \frac{l_g}{\mu_0}\right)}. \quad (3.62)$$

The transduction coefficient for the axisymmetric magnetic assembly and coil configuration shown in Figure 3-10 is thus given by

$$G = \frac{BL_{coil}}{S} = \frac{H_c h_m}{\left(\frac{h_m (h_g + l_g) (2\pi (r_g + l_g))}{\mu_0 \mu_{magnet} (\pi r_m^2)} + \frac{l_g}{\mu_0} \right) S} \cdot L_{coil} \quad (3.63)$$

Note that the 1-D magnetic circuit model is used only to predict the magnetic flux density in the air gap and is not a part of the lumped element modeling paradigm where the power interactions between various components are represented in terms of conjugate power variables.

3.3.2 Calculation of the Transduction Coefficient using Finite Element Analysis

The 1-D magnetic circuit model may not be applicable for all magnetic assemblies. For example, if the length of the gap is much larger than the height of the magnet, the effect of the fringing fields cannot be captured by the simple corrections given by (3.55). In these cases, finite element analysis is used to determine the field pattern produced by the magnetic assembly. The overall transduction coefficient is calculated by computing the average radial flux density over the coil volume.

COMSOL Multiphysics finite element software is used in this work. Figure 3-12 shows the axisymmetric model used. Both the hard and soft magnets are assumed to be “ideal” (constant magnetization for the hard magnet). The hard magnetic material is modeled using the constitutive relationship given by

$$B = \mu_0 \mu_{magnet} H + B_r, \quad (3.64)$$

where B and H are the magnetic flux density (in T , Tesla) and magnetic field intensity (in A/m).

The soft magnetic material is modeled using the constitutive relationship given by

$$B = \mu_0 \mu_{core} H. \quad (3.65)$$

The various material properties used are shown below [23], [40]

- Hard magnet remnant magnetic flux density (B_r) = 1.2 T
- Hard magnet relative permeability (μ_{magnet}) = 1.05
- Core relative permeability (μ_{core}) = 100,000 (Hydrogen annealed). However, here “cold-worked” EFI-50 was used and the relative permeability of 100 was used.

Figure 3-13 shows the results from the finite element simulations. The plot shows the color surface plot of the radial magnetic flux density in the air gap (in Tesla). The streamlines of magnetic flux density are also shown in the same plot. It can be seen that the magnetic flux density in the air gap is primarily directed in the radial direction as expected (all the streamlines are nearly horizontal). The fringing fields can also be seen in the figure.

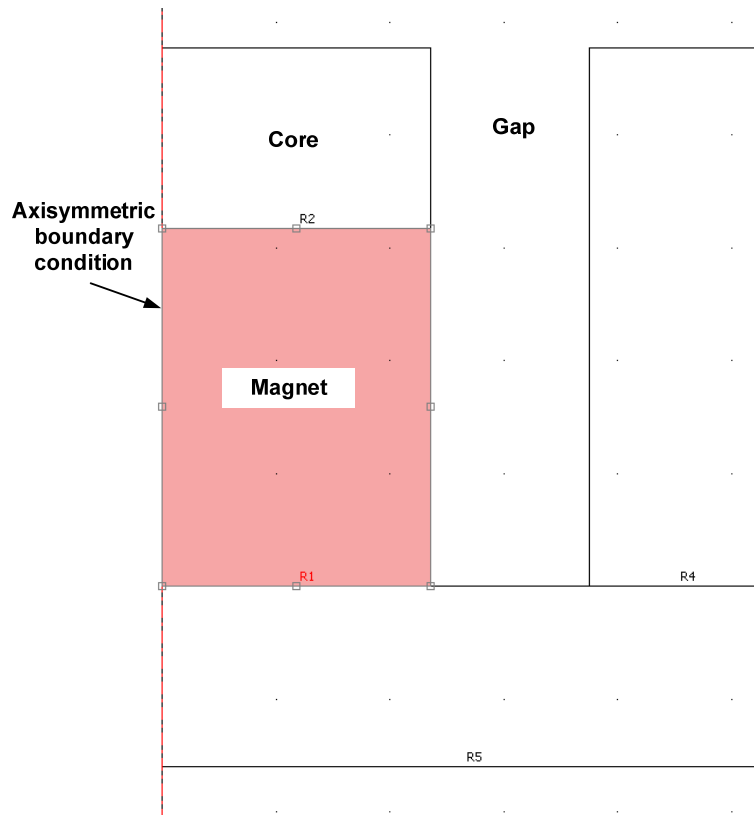


Figure 3-12. Axisymmetric COMSOL model

Table 3-3. Dimensions of the magnetic assembly for 1-D circuit model and finite element modeling comparisons

Parameter	Value (mm)
Magnet radius (r_m)	4.7
Magnet height (h_m)	6.35
Height of the air gap (h_g)	3.2
Width of the annular position (w_c)	3.2
Height of the bottom (h_b)	3.2
Length of the gap (l_g)	Variable

Figure 3-14 shows the comparison between the magnetic flux density calculated using finite element analysis and the simple 1-D model predictions as given by (3.62). The magnetic assembly geometry is detailed in Table 3-3. The magnetic circuit approach slightly over-predicts the flux density in the air gap, particularly for smaller air gaps. Thus the corrections for the fringing fields are adequate, but they do not account for the fringing completely. The general trend, however, is captured reasonably well (within 10%) by the 1-D analytical model for various gap lengths. Hence the 1-D circuit model will be used in this work to calculate the magnetic flux density in the air gap, as it much simplifies the design and optimization of the final structure.

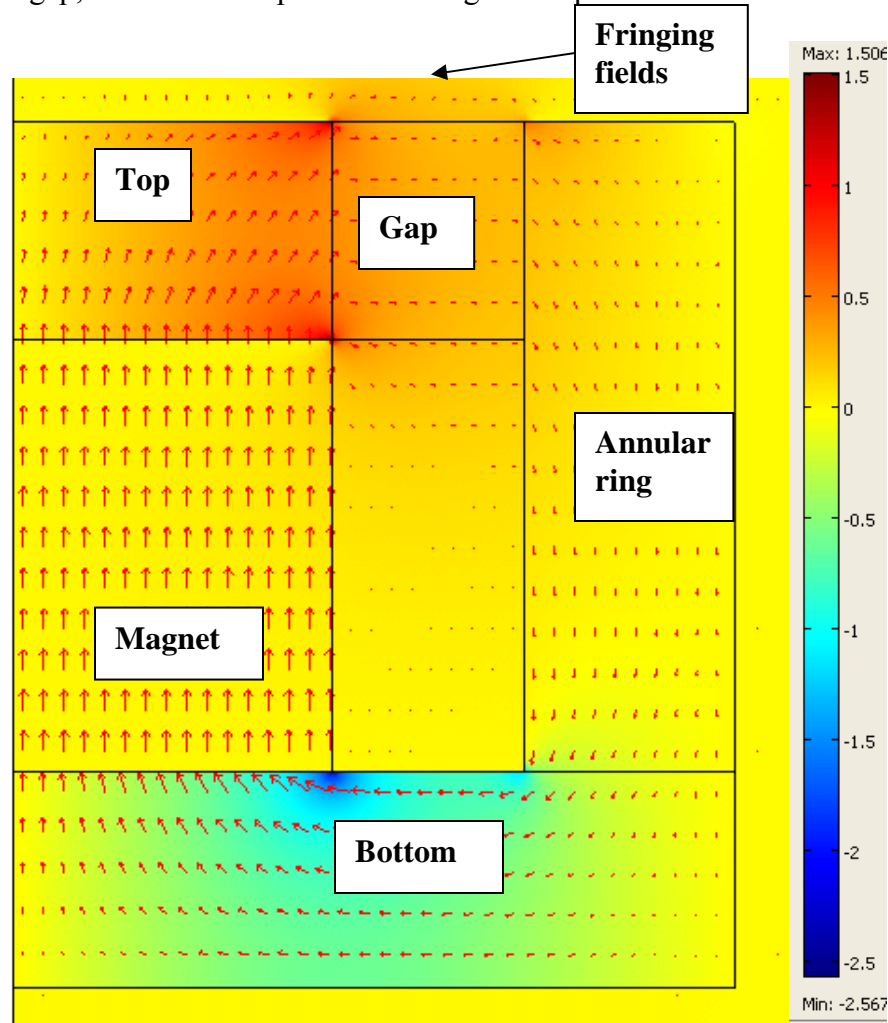


Figure 3-13. Results from the COMSOL model – radial magnetic flux density (Tesla) and streamlines of total magnetic flux density

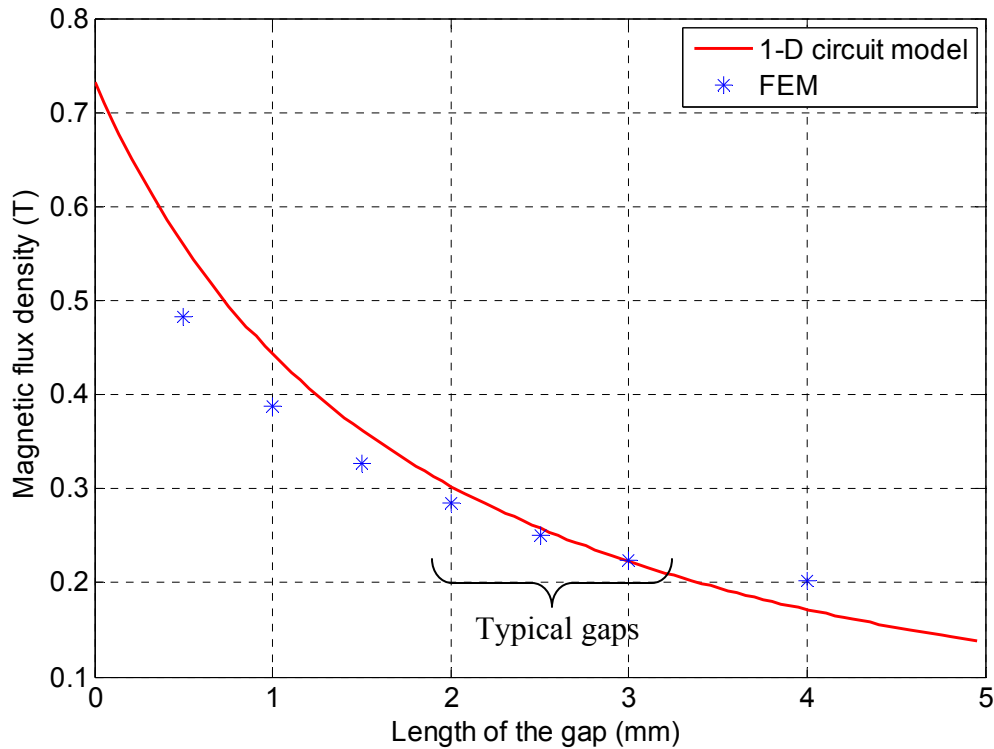


Figure 3-14. Comparison of the magnetic flux density in the air gap between the 1-D circuit model predictions and FEM results (averaged over entire gap volume)

3.4 Diaphragm Model

In order to develop the complete model of the electrodynamic ZNMF actuator, models for the cavity and the slot or orifice need to be developed. It is most convenient to model these components in the acoustic or the fluidic domain. Hence the overall lumped element model uses acoustic domain models for the diaphragm as well. The next section hence presents the coupling between the mechanical domain and acoustic domain. The following section presents the acoustic model of the diaphragm.

3.4.1 Coupling between Mechanical and Acoustic Domains

The conjugate power variables in the acoustic domain are the pressure P and volume velocity Q . The conjugate power variables in the mechanical domain are force F and velocity u . If the effective area of the diaphragm is S , the relationship between these quantities can be expressed as

$$\begin{bmatrix} p \\ Q \end{bmatrix} = \begin{bmatrix} 1/S & 0 \\ 0 & S \end{bmatrix} \begin{bmatrix} F \\ u \end{bmatrix}. \quad (3.66)$$

The pressure is the force divided by the area, whereas the volume velocity is the velocity multiplied by the area. These equations can be represented using an equivalent transformer with the turns ratio $1/S$ as shown in Figure 3-15.

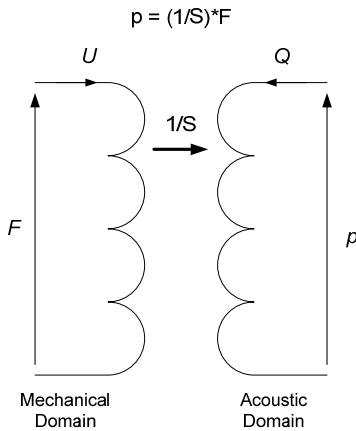


Figure 3-15. Equivalent circuit representation of coupling between the mechanical and acoustic domains

As discussed before, impedance is defined as the ratio of the effort variable and the flow variable. The acoustic impedance is thus defined as the ratio of the pressure p and the volume velocity Q ,

$$Z_{ac} = \frac{p}{Q}. \quad (3.67)$$

Basic transformer relationships then can be used to relate the acoustic impedance Z_{ac} and mechanical impedance Z_{mech} as shown below

$$Z_{ac} = \frac{p}{Q} = \frac{F/S}{Su} = \frac{F}{S^2u} = \frac{Z_{mech}}{S^2} \quad (3.68)$$

The following sections develop the acoustic model for the diaphragm.

3.4.2 Acoustic Model of the Diaphragm

Various diaphragm structures can be used for the electrodynamic ZNMF actuators. The most common configurations are a uniform isotropic diaphragm or a composite transversely isotropic diaphragm. Some commercial devices, such as common loudspeakers, use rigid diaphragms (implemented via a paper cone) with corrugated edges. However, it is much easier to fabricate and analyze the composite diaphragms, and hence they are used for this work.

The schematic of the composite diaphragm is shown in Figure 3-16. The diaphragm consists of a relatively rigid central boss of radius b , Young's modulus E_1 , Poisson's ratio ν_1 and density ρ_1 . The outer annular compliant region extends from $r = a$ to $r = b$. The solidity ratio of the composite diaphragm s is defined as $s = b/a$. The homogenous diaphragm is thus a special case of the composite diaphragm when $b = s = 0$. In this work, the central boss is assumed to be perfectly rigid. Thus the diaphragm is modeled as an annular plate with a clamped outer edge [41].

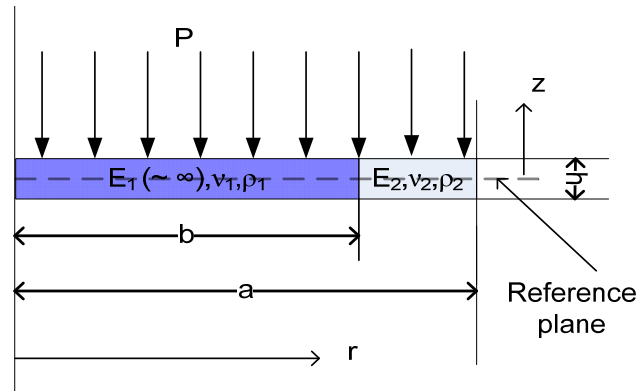


Figure 3-16. Composite diaphragm model as an annular plate

The transverse displacement of the diaphragm $w(r)$ under a uniform pressure load p can be obtained by applying appropriate boundary and matching conditions. The central boss region

moves as a piston with displacement $w(0)$. The transverse displacement of the annular compliant region ($w(r)$) is a function of the radial distance. These are given by

$$w(0) = w(b) = \frac{3p(1-\nu_2^2)a^4}{16E_2h^3} \left[1 + 4\left(\frac{b}{a}\right)^2 \ln\left(\frac{b}{a}\right) - \left(\frac{b}{a}\right)^4 \right] \quad (3.69)$$

and

$$w(r)|_{b < r < a} = \frac{3p(1-\nu_2^2)}{16E_2h^3} \left[1 + 4\left(\frac{b}{a}\right)^2 \ln\left(\frac{r}{a}\right) - 2\left(\frac{r}{a}\right)^2 + 2\left(\frac{b}{a}\right)^2 - 2\frac{b^2r^2}{a^4} + \left(\frac{r}{a}\right)^4 \right]. \quad (3.70)$$

The assumptions and limitations of this model are described in Appendix B.

The acoustic compliance accounts for the change in volume (∇) for a unit of applied pressure, when the electrical voltage to the coil is zero ($V = 0$). The change in volume is calculated by integrating the displacement of the diaphragm over the entire diaphragm. Thus the lumped acoustic compliance C_{aD} is given by

$$C_{aD} = \left. \frac{|\nabla|}{P} \right|_{V=0} = \frac{\int_0^a w(r)2\pi r dr}{P} = \frac{\int_0^b w_1(r)2\pi r dr + \int_b^a w_2(r)2\pi r dr}{P} \quad (3.71)$$

As the central region is assumed to be perfectly rigid, the compliance can be simplified to

$$C_{aD} = \frac{\pi(1-\nu_2^2)a^6}{16E_2h^3} \left[1 - 3\left(\frac{b}{a}\right)^2 + 3\left(\frac{b}{a}\right)^4 - \left(\frac{b}{a}\right)^6 \right], \quad (3.72)$$

and the acoustic compliance is only a function of the solidity ratio and the material properties of the annular region. The detailed derivation of the acoustic compliance is included in Appendix B

If there is no rigid central boss, where $s = b = 0$, the diaphragm is just a homogenous, compliant plate, and the compliance reduces to

$$C_{aD}|_{s=0} = \frac{\pi a^6(1-\nu_2^2)}{16E_2h^3}. \quad (3.73)$$

The effective area of the diaphragm is also determined by calculating the total change in volume and dividing it by the center displacement $w(0)$. Thus the effective area is given by

$$S = \frac{|\nabla|}{w(0)}. \quad (3.74)$$

If the central boss is assumed perfectly rigid, the effective area can be expressed as

$$S = \frac{\pi \left[a^6 - 3b^2 a^4 + 3a^2 b^4 - b^6 \right]}{3a^4 + 12a^2 b^2 \log\left(\frac{b}{a}\right) - 3b^4} = \frac{\frac{\pi a^2}{3} \left[1 - 3\left(\frac{b}{a}\right)^2 + 3\left(\frac{b}{a}\right)^4 - \left(\frac{b}{a}\right)^6 \right]}{\left(1 + 4\left(\frac{b}{a}\right)^2 \ln\left(\frac{b}{a}\right) - \left(\frac{b}{a}\right)^4 \right)}. \quad (3.75)$$

In the limit when the solidity ratio is 0 (homogenous compliant diaphragm), the effective area is $\pi a^2/3$.

The effective mass of the diaphragm is calculated by computing the total kinetic energy of the diaphragm and lumping it to the center velocity. Harmonic motion of the diaphragm is assumed. Since the coil is attached to the central boss of the diaphragm assembly, it also contributes to the total mass of the diaphragm. The acoustic mass of the diaphragm is given by [42]

$$M_{aD} = 2\pi \int_0^a \rho h \left(\frac{w(r)}{\nabla} \right)^2 r dr + \frac{M_{coil}}{S^2}, \quad (3.76)$$

where M_{coil} is the mass of the coil and S is the effective area of the diaphragm.

Since the inner central boss is assumed perfectly rigid, the lumped acoustic mass can be simplified to

$$\begin{aligned} M_{aD} &= \left(\pi b^2 \rho_1 h \right) \left(\frac{w(0)}{\nabla} \right)^2 + 2\pi \rho_2 h \int_b^a \left(\frac{w(r)}{\nabla} \right)^2 r dr + \frac{M_{coil}}{S^2} \\ &= \frac{M_{rigid}}{S^2} + 2\pi \rho_2 h \int_b^a \left(\frac{w(r)}{\nabla} \right)^2 r dr + \frac{M_{coil}}{S^2} \end{aligned}, \quad (3.77)$$

where ρ_1 and ρ_2 are the densities of regions 1 and 2 as indicated in Figure 3-16 and M_{rigid} is the physical mass of the central boss. The detailed derivation is included in Appendix B.

In the limit when the solidity ratio is 0 (homogenous compliant diaphragm), the lumped acoustic mass approaches the acoustic mass of a uniform, isotropic diaphragm given by

$$M_{ad}|_{s=0} = \frac{9}{5} \frac{h\rho_2}{\pi a^2} + \frac{9M_{coil}}{(\pi a^2)^2}, \quad (4.78)$$

where the second term represents the contribution from the mass of the coil.

3.5 Models of the Acoustic/Fluidic Components

The acoustic impedance was defined in the previous section. However, in some cases it is convenient to define another acoustic quantity called the specific acoustic impedance as the ratio of the pressure p and the particle velocity u ,

$$Z_{sp_ac} = \frac{p}{u} = \frac{p}{Q/S} = SZ_{ac}. \quad (3.79)$$

The specific acoustic impedance is useful in developing the models for the cavity and the orifice.

3.5.1 Cavity Model

A short closed cavity of volume V and length L_C driven by a piston is shown in Figure 3-17 [43]. The area of cross-section of the piston is S , and thus the volume is $V = SL_C$. The input specific acoustic impedance is given by [43]

$$Z_{in} = \frac{\rho_0 c_0}{j \tan\left(\frac{\omega L_C}{c_0}\right)} = \frac{\rho_0 c_0}{j \tan\left(\frac{2\pi f L_C}{c_0}\right)}. \quad (3.80)$$

Here ρ_0 is the density and c_0 is the speed of sound for the fluid in the cavity. The driving frequency is f .

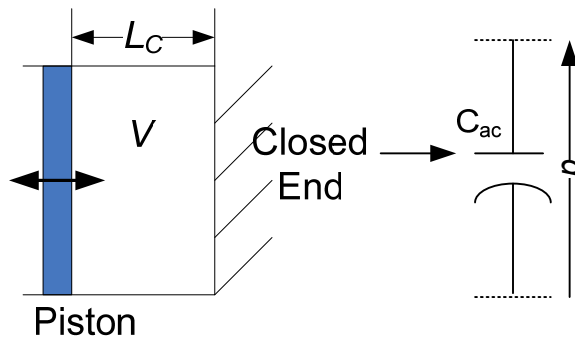


Figure 3-17. Short closed cavity and its lumped model

The cavity is considered “short” when the length L_C is small compared to the wavelength of the drive signal,

$$\frac{\omega L_C}{c_0} = \frac{2\pi L_C}{\lambda} \ll 1. \quad (3.81)$$

The specific acoustic impedance can be simplified using the Maclaurin expansion for the tangent function. The simplified specific acoustic impedance is obtained by ignoring the higher order terms and is given by

$$Z_{spCav} = \frac{\rho_0 c_0}{j \tan\left(\frac{\omega L_C}{c_0}\right)} \approx \frac{\rho_0 c_0}{j \left(\frac{\omega L_C}{c_0} + \frac{1}{3} \left(\frac{\omega L_C}{c_0} \right)^3 + \dots \right)} \approx \frac{\rho_0 c_0^2}{j \omega L_C}. \quad (3.82)$$

The higher order terms can be ignored for $\omega L_C/c_0 \ll 0.3$. The acoustic impedance is thus given by

$$Z_{aCav} = \frac{\rho_0 c_0^2}{j \omega L_C S} = \frac{\rho_0 c_0^2}{j \omega V}. \quad (3.83)$$

This behavior is analogous to a capacitor in the electrical domain. Thus, comparing to capacitive impedance $Z_C = \frac{1}{j\omega C}$, the acoustic compliance is defined as

$$C_{aCav} = \frac{V}{\rho_0 c_0^2}. \quad (3.84)$$

3.5.2 Orifice Model

This section discusses the acoustic model of a circular pipe. The circular pipe has radius a_{OS} and length L_{OS} as shown in Figure 3-18. This narrow orifice can be modeled as an open cavity. Thus the specific acoustic impedance is given by [43]

$$Z_{spOS} = j \rho_0 c_0 \tan\left(\frac{\omega L_{OS}}{c_0}\right) = j \rho_0 c_0 \tan\left(\frac{2\pi f L_{OS}}{c_0}\right). \quad (3.85)$$

The low-order lumped element model for a 2D-slot is developed by assuming a channel flow in the slot.

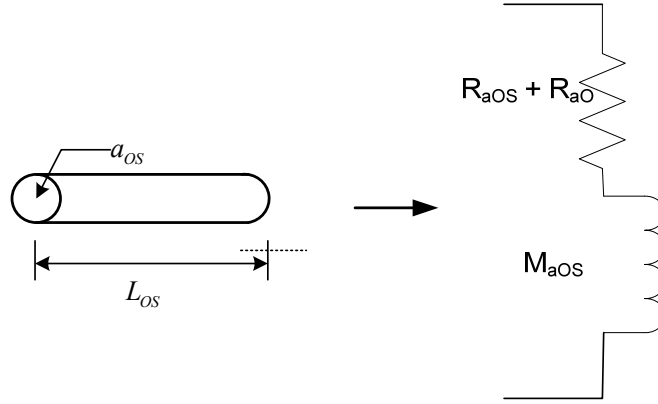


Figure 3-18. Narrow circular orifice and its lumped model

Again assuming a “short” tube per the condition of (3.81), the specific acoustic impedance can be simplified to

$$Z_{spOS} = j\rho_0 c_0 \tan\left(\frac{\omega L_{OS}}{c_0}\right) \approx j\rho_0 \omega L_{OS}. \quad (3.86)$$

Thus the corresponding acoustic impedance is given by

$$Z_{aOS} = \frac{j\rho_0 \omega L_{OS}}{S}. \quad (3.87)$$

This behavior is same as that of a mass in the mechanical domain or an inductor in the electrical domain. Thus, comparing to inductive impedance $Z_M = j\omega M$, the acoustic mass of the orifice is defined as

$$M_{aOS} = \frac{\rho_0 L_{OS}}{S}. \quad (3.88)$$

Note that the length L_{OS} can include end corrections for one or both sides of the tube, depending on whether the end is open or flanged [43]. Also this model assumes uniform flow through the pipe. If viscous effects are considered and fully developed Poiseuille flow is assumed through the pipe, the acoustic mass is slightly different than that given by (3.88). The fully developed Poiseuille flow assumes that the velocity profile through the slot/orifice is the same irrespective of the where the velocity profile is measured.

A complete orifice model also requires the inclusion of the viscous dissipation in the pipe.

The acoustic resistance is given by [43]

$$R_{aOS} = \frac{8\mu L_{OS}}{\pi a_{OS}^4}, \quad (3.89)$$

where μ is the dynamic viscosity of the fluid medium.

In a ZNMF actuator, it is necessary to model the non-linear dump loss in addition to the linear orifice/slot resistance. The non-linear resistance term R_{aO} , accounts for the losses around the corners of the neck. This loss is derived by modeling the orifice as a Bernoulli flow meter and is given by [44],[3]

$$R_{aO} = \frac{\frac{1}{2} K_D \rho_0 Q_{out}}{\pi^2 a_{OS}^4}, \quad (3.90)$$

where, K_D is the nondimensional loss coefficient (usually assumed to be unity), ρ_0 is the density of the fluid and Q_{out} is the output volume velocity. The loss coefficient, K_D is usually a function of the orifice geometry, frequency and the Reynolds number of the flow. Although a circular orifice is considered here, similar approach is used to derive the model parameters of a rectangular slot.

3.5.3 Acoustic Radiation Impedance

In addition to all the fluidic effects that are associated with the orifice discussed in the previous section, some acoustic effects are also important. The orifice (or the slot) is modeled as a piston in an infinite baffle to determine its sound radiation behavior. The radiation impedance associated with it is calculated by computing the average pressure amplitude on the face of the piston in reaction to a prescribed piston velocity. The radiation impedance is given by[43]

$$Z_p = \rho_0 c_0 \left[\underbrace{1 - \frac{2J_1(2ka_{OS})}{2ka_{OS}}}_{R_{aRad}} + j \underbrace{\frac{2K_1(2ka_{OS})}{2ka_{OS}}}_{X_{aRad}} \right]. \quad (3.91)$$

Here $k = \frac{2\pi f}{c_0}$ is the wavenumber at the drive frequency and J_1 and K_1 are the Bessel and Struve functions of order one respectively. R_{aRad} and X_{aRad} are the real and imaginary parts of the piston impedance. These can be simplified at low frequencies ($2ka_{OS} \ll 1$), to

$$R_{aRad} = \frac{(ka_{OS})^2}{1 \cdot 2} - \frac{(ka_{OS})^4}{1 \cdot 2^2 \cdot 3} + \frac{(ka_{OS})^6}{1 \cdot 2^2 \cdot 3^2 \cdot 4} \dots \rightarrow \frac{(ka_{OS})^2}{2}, \quad (3.92)$$

$$X_{aRad} = \frac{4}{\pi} \left[\frac{2ka_{OS}}{3} - \frac{(2ka_{OS})^3}{3^2 \cdot 5} + \frac{(2ka_{OS})^5}{3^2 \cdot 5^2 \cdot 7} \dots \right] \rightarrow \frac{8ka_{OS}}{3\pi}. \quad (3.93)$$

The reactive behavior (X_{aRad}) is analogous to an inductor in the electrical domain (kinetic energy storage). Thus, comparing to $Z_M = j\omega M$, the acoustic radiation mass is defined as

$$M_{aRad} = \frac{8}{3\pi^2 c_0 a_{OS}}. \quad (3.94)$$

Thus for low frequencies, a piston is represented as a frequency dependent resistance (R_{aRad}) and an acoustic radiation mass (M_{aRad}) as shown in Figure 3-19.

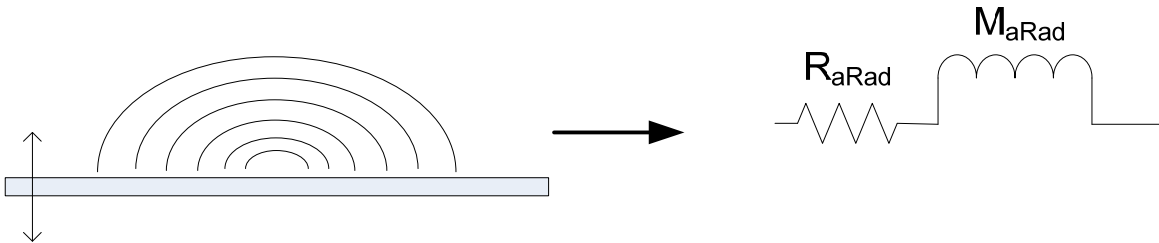


Figure 3-19. Lumped model of a piston in an infinite baffle

All the lumped parameters for the electrodynamic ZNMF actuator are summarized in Table 3-4 below. The simplified expressions for each parameter are included here as a quick reference. Note that the basic scaling information of the individual parameters can be easily deduced from these equations. For example, if all the dimensions of the diaphragm are scaled by a factor of k , the compliance scales as k^3 .

Table 3-4. Lumped parameters for electrodynamic ZNMF actuator

Parameter	Symbol	Value	Reference	
Lumped acoustic mass of the diaphragm	M_{aD}	$\frac{M_{rigid}}{S^2} + 2\pi\rho_2 h \int_b^a \left(\frac{w(r)}{\nabla} \right)^2 r dr + \frac{M_{coil}}{S^2}$	(3.77) (Appendix B)	
Lumped mechanical compliance of the diaphragm	C_{aD}	$\frac{\pi(1-\nu_2^2)a^6}{16E_2h^3} \left[1 - 3\left(\frac{b}{a}\right)^2 + 3\left(\frac{b}{a}\right)^4 - \left(\frac{b}{a}\right)^6 \right]$	(3.72)	
Lumped acoustic compliance of the cavity	C_{aCav}	$\frac{V}{\rho_0 c_0^2}$	(3.84)	
Lumped acoustic mass of the circular orifice or 2D slot	M_{aOS}	Orifice $\frac{\rho_0 L_{OS}}{\pi a_{OS}^2}$	Slot $\frac{6\rho_0 L_{OS}}{5w_{OS}d_{OS}} *$	(3.88)
Lumped acoustic resistance of a circular orifice or 2D slot	R_{aOS}	Orifice $\frac{8\mu L_{OS}}{\pi a_{OS}^4}$	Slot $\frac{12\mu L_{OS}}{w_{OS}d_{OS}^3} *[45]$	(3.89)
Non-linear resistance of the orifice/slot	R_{aO}	$K_D \frac{1}{2} \rho_0 \frac{ Q_{out} }{S_{OS}^2} *$		(3.90)
Lumped acoustic radiation resistance of the circular orifice	R_{aRad}	Orifice $\frac{\rho_0 c_0 (ka_{OS})^2}{2}$	Slot $\frac{1}{2\pi} \rho_0 c_0 k^2 \left(1 - \frac{k^2 d_{OS}^2}{36} \right) [46]$	(3.92)
Lumped acoustic radiation mass of the circular orifice	M_{aRad}	Orifice $\frac{8\rho_0}{3\pi^2 a_{OS}}$	Slot $\frac{\rho_0 w_{OS}}{\pi} \left(\frac{1}{\ln(2d_{OS}/w_{OS})} + \frac{1}{1 - \frac{1}{6}k^2} \right)$	(3.94)

* w_{OS} and d_{OS} are the width and the depth of the 2D slot and S_{OS} is the area of the slot or the orifice.

3.6 Transfer Function for Electrodynamic ZNMF Actuator

The overall lumped element model for the electrodynamic ZNMF actuator was developed in section 3.2 and all the individual components were detailed in following sections. This section uses the overall lumped model to obtain a relationship between the input electrical excitation and the output jet velocity. For a given electrical excitation, the output volume velocity Q_{out} is first

calculated from the nonlinear lumped element model as a function of frequency using an iterative technique to account for the nonlinear neck resistance term. Once the output volume velocity is known, the average jet velocity and centerline velocity can be calculated by assuming a Poiseuille flow in the slot or the orifice.

To facilitate a simpler electrical circuit, the gyrator can be “eliminated” from the circuit by referring the electrical components to the acoustic domain or vice versa (section 3.1). As drawn in Figure 3-20, the electrical impedance Z_{eC} can be referred to an effective acoustic impedance Z_a via

$$Z_{eC} = \frac{V}{I} = \frac{\frac{BL_{coil}}{S} Q}{\frac{S}{BL_{coil}} P} = \left(\frac{BL_{coil}}{S} \right)^2 \frac{Q}{P} = \frac{G^2}{Z_a}. \quad (3.95)$$

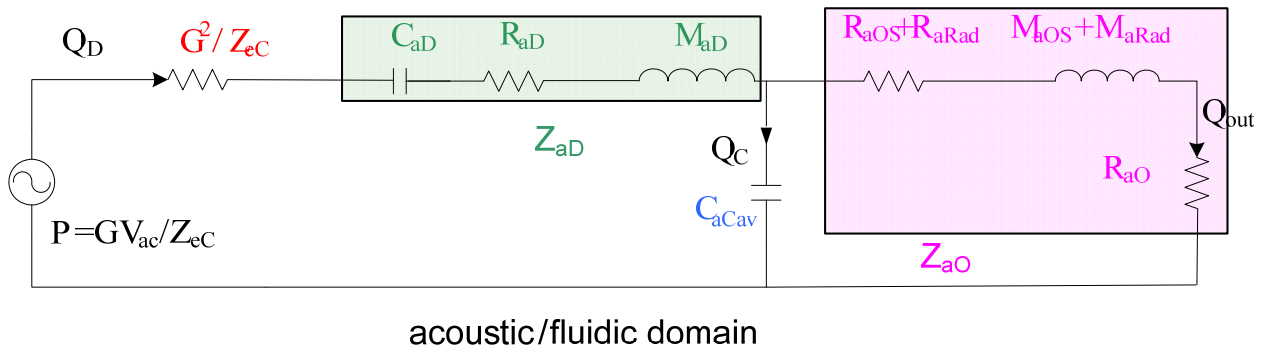


Figure 3-20. Lumped element model of the electrodynamic ZNMF actuator referred to the acoustic domain

The equivalent circuit referred entirely to the acoustic domain is shown in Figure 3-20. The electrical voltage source V_{ac} in is represented as a pressure source given by

$$P = \frac{GV_{ac}}{Z_{eC}} \quad (3.96)$$

Using the current divider relation,

$$\frac{Q_{out}}{Q_D} = \frac{1}{\left[C_{aCav} (M_{aOS} + M_{aRad}) \right] s^2 + \left[C_{aCav} (R_{aOS} + R_{aO}) \right] s + 1}. \quad (3.97)$$

The volume velocity Q_D is given by

$$Q_D = \frac{GV_{ac}/Z_{eC}}{Z_{eff} + G^2/Z_{eC}} \quad (3.98)$$

where $Z_{eff} = Z_{aD} + (Z_{aCav} \parallel Z_{aO})$. The overall transfer function is thus given by

$$\frac{Q_{out}}{V_{ac}} = \frac{G/Z_{eC}}{\left[\frac{G^2}{Z_{eC}} + (R_{aD} + sM_{aD}) + \frac{1}{sC_{aD}} \right] \left[C_{aCav}M_{aO}s^2 + C_{aCav}(R_{aOS} + R_{aO})s + 1 \right] + (R_{aOS} + R_{aO} + sM_{aO})} \quad (3.99)$$

where $M_{aO} = M_{aOS} + M_{aRad}$ is the effective acoustic mass of the orifice that includes the radiation mass of the orifice.

Using the transfer function, a few limiting cases can be investigated to obtain some insight into the device operation. Here $Z_{eff} = Z_{aD} + (Z_{aCav} \parallel Z_{aO})$ is the effective acoustic impedance of

the mechanical and acoustic components. Also Q_D is defined as $Q_D = \frac{GV_{ac}/Z_{eC}}{Z_{eff} + G^2/Z_{eC}}$.

- CASE 1. $Z_{aO} \gg Z_{aCav}$, that is the orifice impedance is much larger than the cavity impedance, then $Q_{out} \rightarrow 0$. There is no output volume velocity as all the fluid displaced by the diaphragm is compressed or expanded within the cavity. This case will arise for a highly compliant cavity (i.e., very large volume or compliant walls).
- CASE 2. $Z_{aCav} \gg Z_{aO}$, that is the orifice impedance is much larger than the cavity impedance, then $Q_C \rightarrow 0$. In this case, all the fluid displaced by the diaphragm is pushed out of the orifice and there is no compression of the fluid in the within the cavity. This makes sense for a very stiff cavity (i.e., very small volume).
- CASE 3. $Z_{aD} \rightarrow \infty$, that is the diaphragm impedance is very high, then $Q_{out} \rightarrow 0$. Physically, this corresponds to case when the diaphragm does not provide significant displacement. This can happen for a diaphragm with large resistance and mass and a low compliance (i.e., high stiffness).
- CASE 4. $G^2/R_{eC} \gg Z_{eff}$, that is the referred electrical impedance is larger than any other impedance in the model, then $Q_D \rightarrow \frac{V_{ac}}{G}$. Here the electrical components of the actuator dominate the overall behavior of the actuator.

- CASE 5. $G^2/R_{eC} \ll Z_{eff}$, then $Q_D \rightarrow GV_{ac}/(R_{eC}Z_{eff})$. Physically, this corresponds to the case where the effective acoustic impedance of the components dominates and limits the diaphragm volume velocity.

The overall lumped element model for the electrodynamic ZNMF actuator is developed in Chapter 3. This model can be used as a predictive tool for determining the performance of any device. The model can also be used as a design and optimization tool to meet target specifications for various applications.

CHAPTER 4 FABRICATION AND MODEL VALIDATION OF PROTOTYPE ELECTRODYNAMIC ZNMF ACTUATORS

The overall lumped element model for the electrodynamic ZNMF actuator was developed in Chapter 3. Chapter 4 presents fabrication and experimental validation of two electrodynamic ZNMF actuators. Section 4.1 describes a prototype ZNMF actuator built around a conventional loudspeaker. The parameter extraction and the model validation of this actuator are also presented in this section. Section 4.2 discusses the fabrication details for a completely custom-made, composite-diaphragm ZNMF actuator. The model validation for this custom-built actuator is discussed in section 4.3.

4.1 Speaker-Driven Electrodynamic ZNMF Actuator

From the schematic of a generic electrodynamic ZNMF actuator shown in Figure 3-3, it can be seen that the structure is essentially an oscillating diaphragm with a cavity and a slot through which the jet is established. For initial validation of the lumped model, a prototype device with a commercial speaker as the mechanical driver and a custom-built cavity and slot (or orifice) was built.

A 1 W, 8 Ω speaker (CUI, Inc. Model number GF0771) was used as the mechanical driver [47]. The cavity and the slot were rapid prototyped using Acrylonitrile butadiene styrene (ABS) plastic. A schematic and the photographs of the device are shown in Figure 4-1 and Figure 4-2 respectively. The dimensions of the speaker driver, the cavity, and the slots are summarized in Table 4-1. The volume of the cavity is one of the parameters need to calculate its lumped compliance. The volume was calculated using the manufacturer specified dimensions of the speaker cone. The profile of the speaker cone was also verified using the Keyence LKG 32 (Model Number LKGD 500) laser displacement sensor.

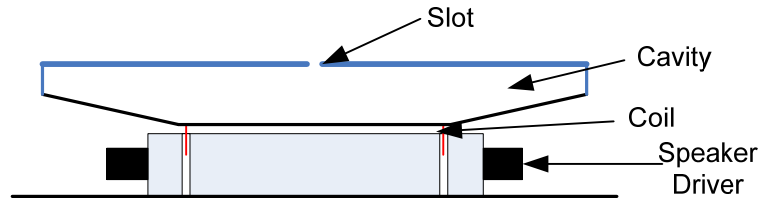


Figure 4-1. Schematic of the speaker-driven electrodynamic ZNMF actuator

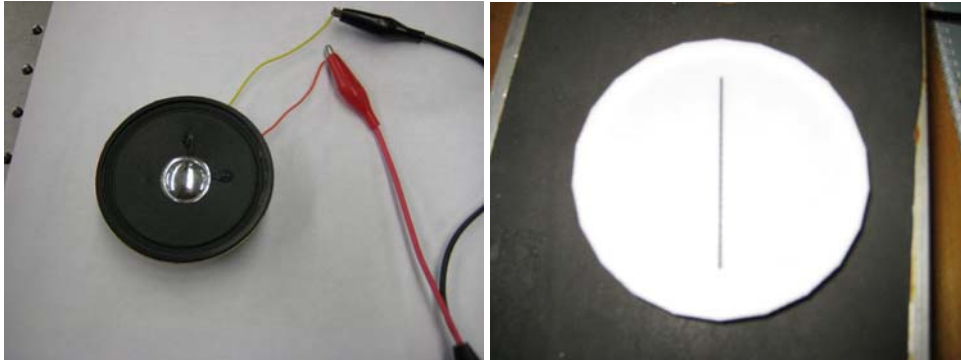


Figure 4-2. Photograph of the speaker-driver, the cavity and the slot

Table 4-1. Geometrical parameters for speaker-driven ZNMF actuator

Parameter	Value
Piston radius (a)	38.5 mm
Cavity volume (V)	$2.7 \times 10^{-4} \text{ m}^3$
Slot height (L_{OS})	1 mm
Slot width (d_{OS})	1 mm
Slot length (w_{OS})	60 mm

4.1.1 Lumped Parameter Extraction

Since the speaker was purchased and not designed in-house, the lumped element model parameters for the speaker-driver such as the acoustic compliance, acoustic mass, diaphragm damping, and transduction coefficient were not known beforehand. In order to model the actuator performance, it is essential to know these parameters. This section discusses generic parameter extraction procedures to determine the relevant model parameters.

4.1.1.1 Electrical impedance (R_{eC} and L_{eC})

The speaker driver had a rated resistance of 8 Ω . The dc resistance was measured to be 7.8 Ω using Fluke digital multimeter. The impedance of the speaker versus frequency—both the resistance and inductance—was measured using the Agilent 4294A precision impedance analyzer over a frequency range of 40 Hz – 1000 Hz. The diaphragm was free to move; thus this actually was a measure of the series combination of the electrical impedance and the reflected mechanical impedance $\frac{(BL_{coil})^2}{Z_{aD}}$, where $(Z_{aD} = R_{aD} + j\left(\omega M_{aD} - \frac{1}{\omega C_{aD}}\right))$. The measured free impedance of the speaker-driver is shown in Figure 4-3. As this test was performed in air, there is an additional acoustic load on the diaphragm (acoustic radiation resistance and acoustic radiation mass).

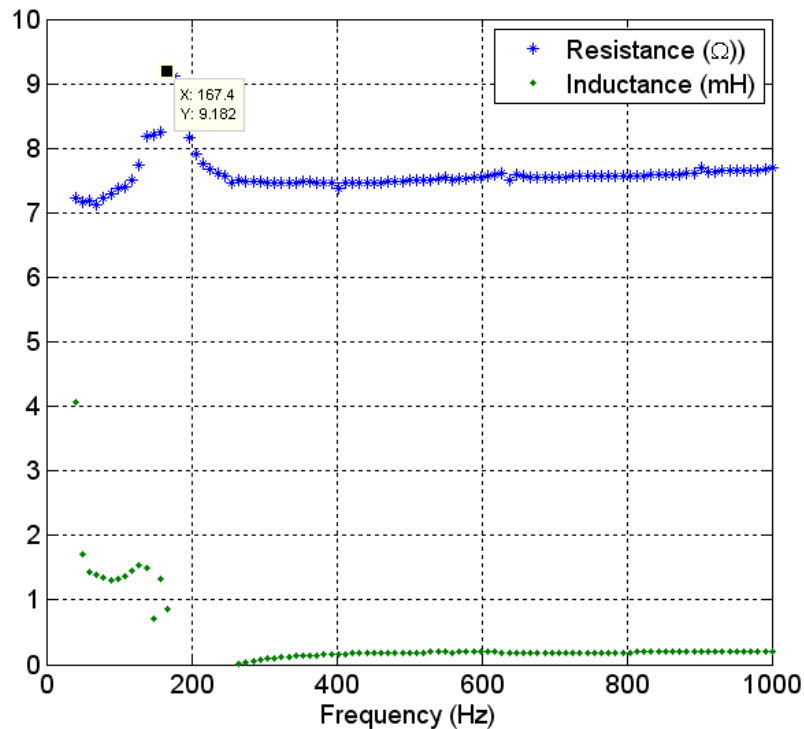


Figure 4-3. Electrical impedance of the speaker-driver

The peak seen in the data at about 165 Hz is due to the electromechanical resonance. Since the electrical coil parameters (R_{ec} and L_{ec}) could not be isolated from this measurement, the dc resistance of the coil was used, and the inductance was ignored as at low frequencies the contribution of the inductive reactance is small.

4.1.1.2 Mechanical compliance (C_{mD})

The speaker-driver has corrugated edges that determine the mechanical compliance. The maximum displacement and the resonant frequency of the actuator are both controlled by the compliance. The mechanical compliance (C_{mD}) of the speaker diaphragm was measured using static mechanical pull tests, as illustrated in Figure 4-4. The speaker-driver (without the cavity assembly) was mounted on a rigid platform and loaded with known weights. The resulting center displacement of the speaker-driver was measured using a laser displacement sensor (LDS) (Keyence LKG-32 Model Number LKGD 500).

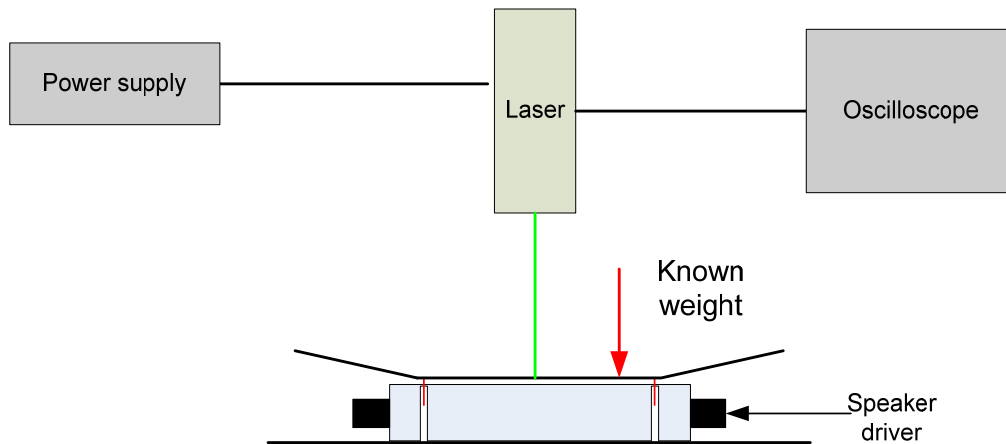


Figure 4-4. Experimental setup for compliance measurement

To extract a suitable compliance parameter, the displacement range mimicked that during standard operation. The maximum displacement observed for the speaker was about 0.3 mm (peak). Hence the displacement range used for the compliance and transduction factor

measurements was ± 0.2 mm. The results from a static displacement test are shown in Figure 4-5. It can be seen that for the measured range of applied forces the speaker-driver displacement is very linear. The extracted mechanical compliance of this speaker-driver was 0.46 mm/N, as indicated in Table 4-2.

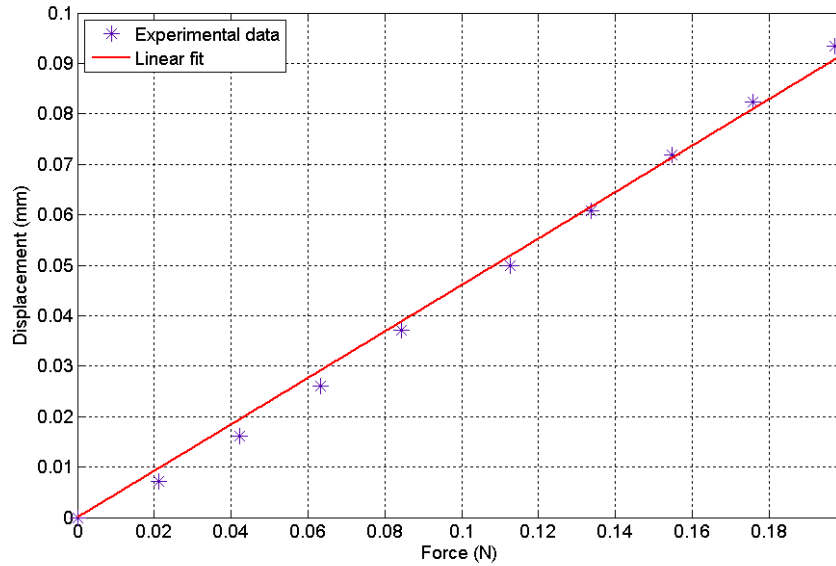


Figure 4-5. Results from compliance measurement

Table 4-2. Linear curve fit results for compliance measurements

Parameter	Value
Extracted mechanical compliance	0.46 mm/N
95 % confidence intervals	0.4469 – 0.4739 mm/N
R^2	0.9953

The overall lumped model for the ZNMF actuator developed in Chapter 3 requires the acoustic compliance C_{aD} . Thus it is necessary to convert the measured mechanical compliance to an acoustic compliance. The relationship between the mechanical and acoustic impedances was presented in section 3.41. Using this relation, the acoustic compliance can be converted to the equivalent acoustic compliance as follows

$$C_{aD} = C_{mD} S^2 \quad (4.100)$$

where S is the equivalent area of the mechanical structure. Here it is assumed that the entire speaker-driver moves as a rigid piston, since the corrugated edge diaphragm accounts for only a small portion of the surface area. Thus the equivalent area of the speaker-driver is assumed to be the physical area. The acoustic compliance of the speaker-driver was calculated to be $9.97 \times 10^{-9} \text{ m}^5/\text{N}$.

4.1.1.3 Electromechanical transduction coefficient (BL_{coil})

The transduction factor from the electrical to the mechanical domain is given by BL_{coil} as discussed in section 3.2. As the details regarding magnetic assembly and the coil structure of the speaker driver were not known, the transduction factor was determined indirectly by exciting the piston electrically with a dc current and measuring the displacement with a LDS, as shown in Figure 4-6. Using the force balance, $F = BL_{coil}I = x/C_{mD}$, the transduction factor was determined since the mechanical compliance was known, and the displacement x and current I were directly measured. The displacement was measured using the Keyence LKG-32 LDS (Model Number LKGD 500), and the current was measured using a Tektronix TCPA300 current probe.

Like the compliance test, the displacement range mimicked the operational range of the actuator. A least squares method was used to fit a line to the data, as shown in Figure 4-7. The displacement at each drive current was measured 31 times. The uncertainty estimates in the measurement are also indicated in the plot. Note that this measurement was carried out at both positive and negative currents, and the device was shown to exhibit some hysteresis behavior. This could be due to magnetic or mechanical non-linear effects, especially since the speaker was being driven beyond its normal operational limits. Also, since the detailed design and operation of the speaker was outside the scope of this work, the source of this hysteresis was not fully

investigated. The curve fit results for the transduction factor measurements are indicated in Table 4-3, and the extracted transduction factor was 1.35 N/A. The electromechanical transduction coefficient was converted to equivalent electroacoustic transduction coefficient (G) by using the effective area of the speaker-driver. The electroacoustic transduction coefficient of the speaker-driver is 289.9 Pa/A.

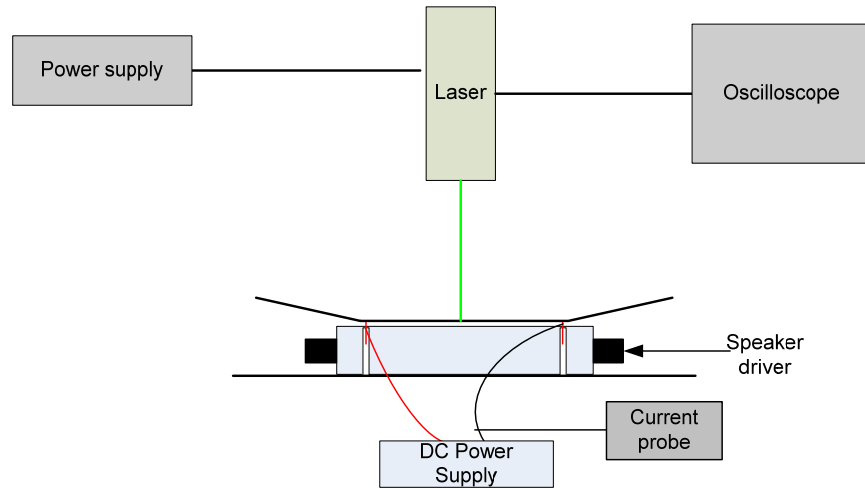


Figure 4-6. Experimental setup for transduction factor measurement

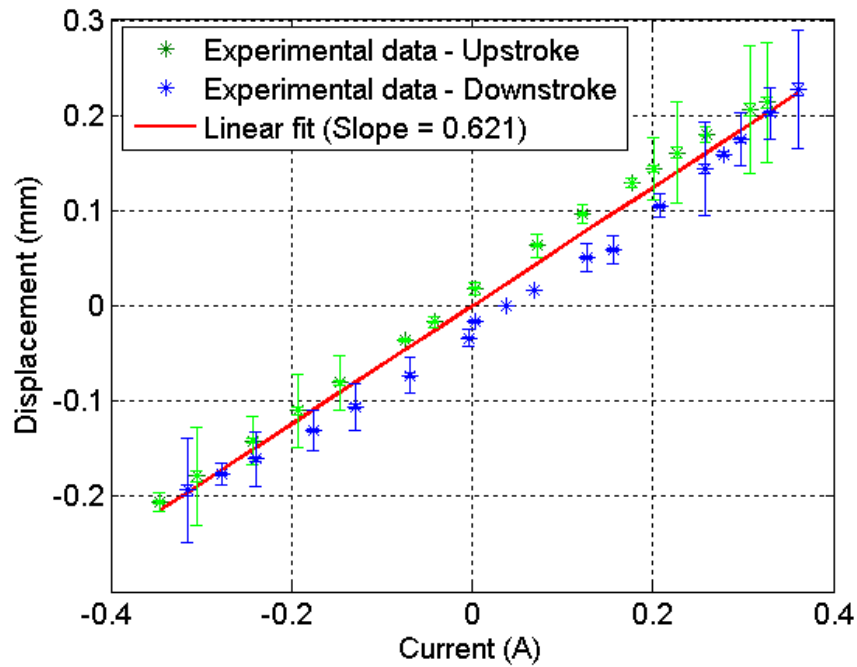


Figure 4-7. Results from the transduction factor measurement

Table 4-3. Linear curve fit results for transduction factor measurements

Parameter	Value
Extracted slope	0.621 mm/A
95 % confidence intervals	0.5907 – 0.6513 mm/N
R^2	0.9809

4.1.1.4 Diaphragm acoustic resistance (R_{aD}) and equivalent acoustic mass (M_{aD})

The diaphragm and voice coil are all permanently attached to one another, and hence the effective mechanical mass of the piston was measured indirectly by performing an impulse test. The damping ratio and consequently the acoustic resistance (R_{aD}) corresponding to the diaphragm damping is also obtained from this test.

In order to measure the diaphragm parameters, it is essential to isolate the electrical components of the device (to avoid any unwanted electromechanical coupling) but also to provide consistent mechanical excitation. A known force was applied by exciting the coil with a dc current to achieve a static displacement of the diaphragm. An electrical switch was then opened to open-circuit the coil such that current could no longer flow, thereby removing the mechanical force. Any electrical transients were assumed to be much faster than the resulting mechanical motion, so this procedure simulated an impulse response with a known initial condition. The resulting diaphragm oscillation was measured using the laser displacement sensor (LDS) (Keyence LKG-32 Model Number LKGD 500). The setup of the experiment is shown in Figure 4-8.

The time-series data of the displacement is shown in Figure 4-9. The initial displacement of -0.3 mm is seen when the coil is excited with a dc current. When the switch is opened, the displacement decays to zero. The displacement is essentially the free response of the diaphragm with the dc displacement as the initial condition (initial value problem). The characteristic under-damped system response is observed. The damping ratio and the damped natural frequency are

extracted from this data using the log decrement method described below[48]. A non-linear curve fit may also be used to extract these parameters as shown in the figure.

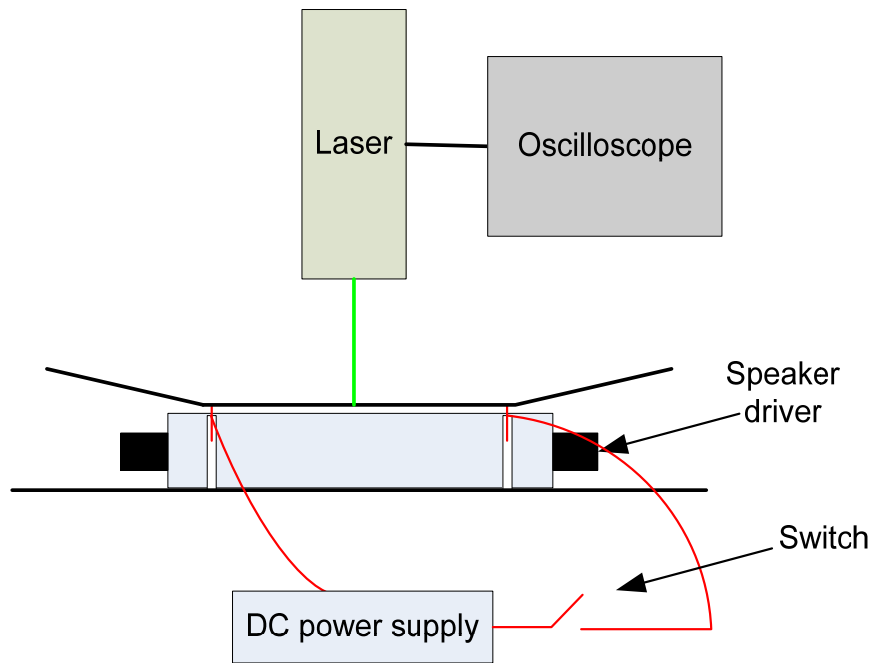


Figure 4-8. Setup for the impulse response test

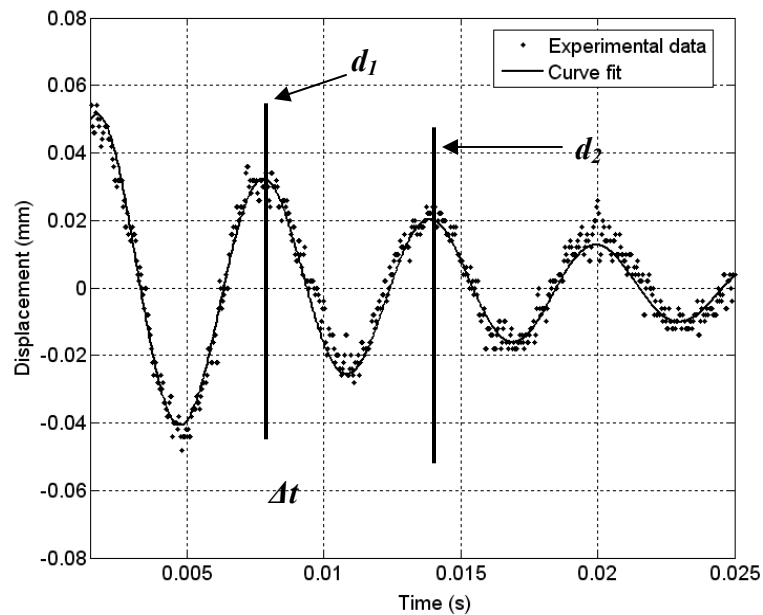


Figure 4-9. Results from the impulse response test

If d_1 and d_2 are the values of displacements measured at two consecutive peaks as shown, the damping ratio is given by

$$\delta = \ln\left(\frac{d_1}{d_2}\right), \quad \zeta = \frac{\delta}{\sqrt{\delta^2 + 4\pi^2}} \quad (4.101)$$

The damped natural frequency f_d can be extracted from the time difference between the two peaks as follows

$$f_d = \frac{1}{\Delta t} \quad (4.102)$$

The natural frequency is then given as

$$f_n = \frac{1}{2\pi} \left(\frac{2\pi}{\Delta t} - \sqrt{1 - \zeta^2} \right) \quad (4.103)$$

The natural frequency is related to the mechanical mass and compliance

$$f_n = \frac{1}{2\pi\sqrt{M_{mD}C_{mD}}} \quad (4.104)$$

Thus the effective mechanical mass can be obtained and it is converted to equivalent acoustic mass (M_{aD}) as follows

$$M_{aD} = \frac{M_{mD}}{S^2}. \quad (4.105)$$

The extracted values of the damping and natural frequency were 0.015 and 193 Hz respectively.

Thus the effective mechanical mass calculated using (4.104) is 1.5 g. The effective acoustic mass calculated using (4.105) is 70.3 kg/m⁴. The damping ratio is converted to an equivalent acoustic resistance as follows

$$R_{aD} = 2\zeta \sqrt{\frac{M_{aD}}{C_{aD}}}. \quad (4.106)$$

Thus the extracted acoustic resistance is 2.52 x 10³ N-s/m⁵.

Another experiment was also used to extract the diaphragm damping. The experimental setup is similar to the one shown in Figure 4-6. The only difference was that the speaker-driver

was excited with a 5 V p-p, 1 Hz, 50 % duty cycle square wave using an Agilent 33120A function generator. The electrical stimulus was never disconnected. In this configuration, the total observed damping originates from mechanical and electrical losses (due to the electromagnetic coupling).

This system exhibited a characteristic underdamped second-order displacement step response, as shown in Figure 4-10. The displacement step response for a standard second order system is given by

$$x(t) = 1 - e^{-\zeta\omega_n t} \cos(\omega_n \sqrt{1-\zeta^2} t) \quad (4.107)$$

where $x(t)$ is the displacement of the diaphragm, ω_n is the natural frequency in rad/sec and ζ is the damping ratio of the system. A non-linear curve fit was used to fit the standard second order system response to the measured displacement data. The curve fit is also shown in Figure 4-10.

The extracted values of damping ratio and the total damping from this experiment were 0.08 and 1.23×10^4 N-s/m⁵ respectively.

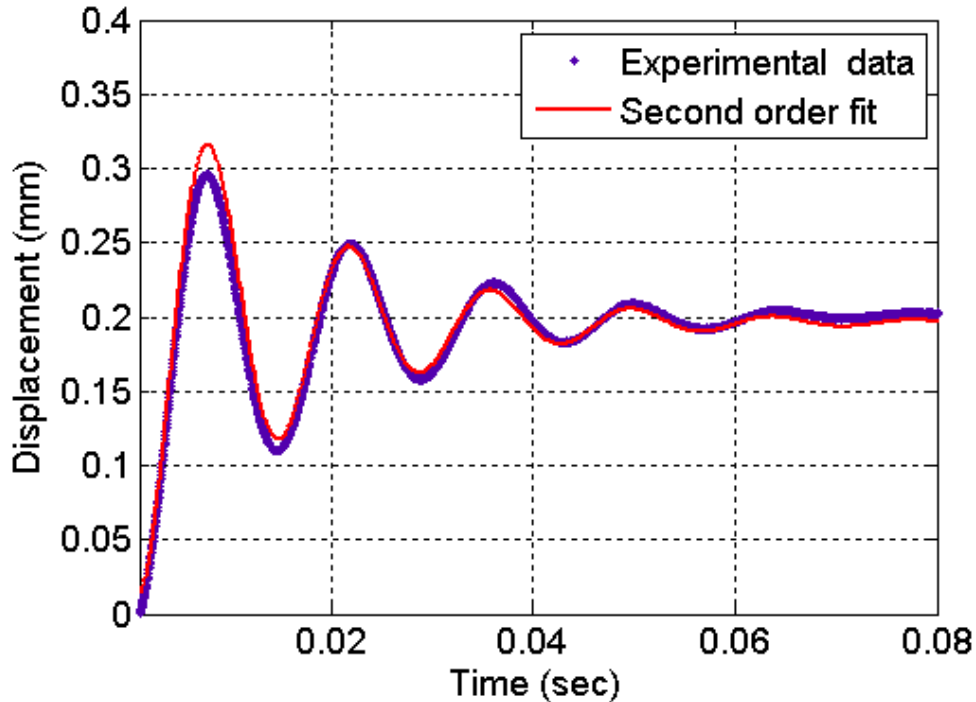


Figure 4-10. Step response of the diaphragm and the curve fit

As mentioned above, the damping measured here is a combination of the diaphragm damping and an effective electrical damping. The equivalent electrical circuit is shown in Figure 4-11. Note that the impedance of the source driving the speaker is usually small and is ignored in this analysis. Thus the total damping term measured is given by

$$R_{measured} = \frac{G^2}{R_{eC}} + R_{aD} \quad (4.108)$$

Based on other previous measurements, the equivalent electrical damping G^2/R_{eC} is calculated to be 9.55×10^3 N-s/m⁵. Thus the diaphragm damping R_{aD} is 2.72×10^3 N-s/m⁵. Note, the electrical damping component is nearly four times higher than the mechanical damping.

Comparing this closed-circuit result to the other open-circuit damping experiment, fairly good agreement is seen in the extracted diaphragm damping. However, the open-circuit damping measurement is used for this work, since it is a more direct measurement of the damping. Table 4-4 summarizes all the extracted parameters of this actuator. These parameters are used in the lumped element model to predict the output volume velocity produced by the actuator.

Table 4-4. Extracted parameters for the speaker-driven ZNMF actuator

Extracted parameter	Value
Electrical resistance (Ω) (R_{eC})	7.8
Mechanical transduction coefficient [49] (BL_{coil})	1.35
Acoustic transduction coefficient [Pa/A] (BL_{coil}/S)	289.9
Mechanical compliance [mm/N] (C_{mD})	0.46
Acoustic compliance [m ⁵ /N] (C_{aD})	9.97×10^{-9}
Mechanical mass [gm] (M_{mD})	1.5
Acoustic mass [kg/m ⁴] (M_{aD})	70.34
Damping ratio (ζ) (Diaphragm only)	0.015
Damping ratio (ζ) (Diaphragm + Electrical)	0.083
Natural frequency [Hz]	193
Equivalent diaphragm damping [N-s/m ⁵] (R_{aD}) (Diaphragm only)	2.52×10^3
Equivalent diaphragm damping [N-s/m ⁵] (R_{aD}) (Diaphragm + Electrical)	2.72×10^3

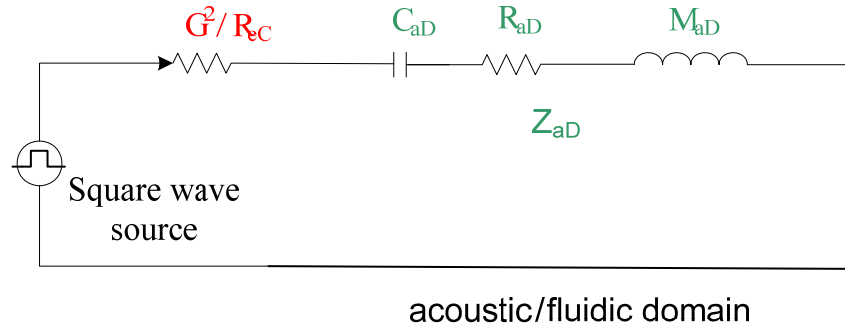


Figure 4-11. Equivalent circuit for the impulse response test

4.1.2 Hotwire Measurements – Overall Model Verification

The validation of the lumped model for speaker-driven actuator is presented in this section. The output velocity from the actuator was measured using a constant temperature hotwire anemometer with a standard 5 μm diameter, 1.25 mm long wire (Dantec 55P11). The Dantec Streamline 90N10 Frame and 90N02 flow unit were used for calibration of the hot wire. The hotwire calibration provides the relationship between flow velocity and hotwire voltage. The empirical relationship between hotwire voltage E and the flow velocity U is given by King's law as

$$E^2 = A + BU^n, \quad (4.109)$$

where A , B and n are constants[50]. A least square curve fit is used to extract the constants. Thus the velocity for any measured hotwire voltage can be calculated. A typical hotwire calibration curve is shown in Figure 4-12. In this case, the constants A , B and n are 0.0069, 0.0036 and 0.4537 respectively.

After calibration, the hotwire was moved to the center of the actuator slot. The speaker actuator was then excited using sinusoidal voltage. The voltage signal shown on the oscilloscope was used to adjust the depth of the wire in the slot such that the unrectified and rectified voltage signals were equal in amplitude; this ensured that the hotwire was exactly in the center of the slot, though the length of the slot. Thus the peak velocity produced by the jet is measured using

the hotwire. The lumped element model of the ZNMF actuator developed in Chapter 3 predicts the total output volume velocity Q_{out} . This is converted to the peak velocity by assuming Poiseuille flow in the orifice. For Poiseuille flow through an orifice, the peak (centerline) velocity is 1.5 times the average velocity [51]. For the flow through the 2D slot, the channel flow model is used [45]. The peak (centerline) velocity in this case is twice the average velocity. Note that the velocity profile in the slot/orifice is dependent on the Stoke's number of the flow defined as $St = \sqrt{\omega d^2/\nu}$. Here ω is the radian frequency of operation, d is the depth of the slot and ν is the kinematic viscosity of the fluid. The Poiseuille flow assumption is only valid for Stoke's number of zero. For non-zero Stoke's number a frequency dependent correction factor is necessary to convert from average velocity to centerline velocity[45]. For example, at 100 Hz the Stoke's number corresponding to the 1 mm radius orifice is about 1. Thus the ratio of the centerline velocity and the average velocity is lesser than 1.5.

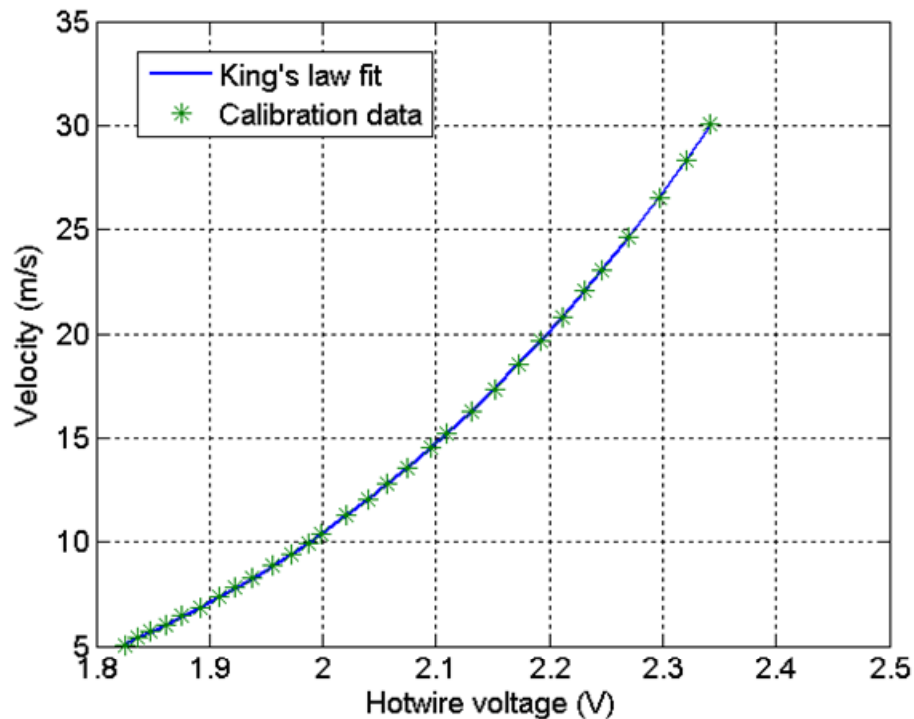


Figure 4-12. Typical hotwire calibration curve

The excitation frequency and amplitude was varied over the range of interest for each device, with the maximum voltage limited by the maximum allowable current through the coils. Figure 4-13 shows the comparison between the model-predicted and experimentally measured output velocity. 10 blocks of data were taken and the 95 % confidence intervals B for the measured velocity were calculated using the standard t-distribution as follows [52]

$$B = \pm \frac{1.812\sigma}{\sqrt{10}} \quad (4.110)$$

where σ is the standard deviation of the velocity. It can be seen that the model captures the first resonant peak (both the frequency and amplitude) of the output velocity well. The LEM predictions deviate from the experimental results particularly for higher frequencies. This may be due to the non-linearities in the speaker compliance or the transduction coefficient. In addition, there is significant uncertainty in the volume of the cavity. The slot model also needs to be refined to be applicable at higher frequencies.

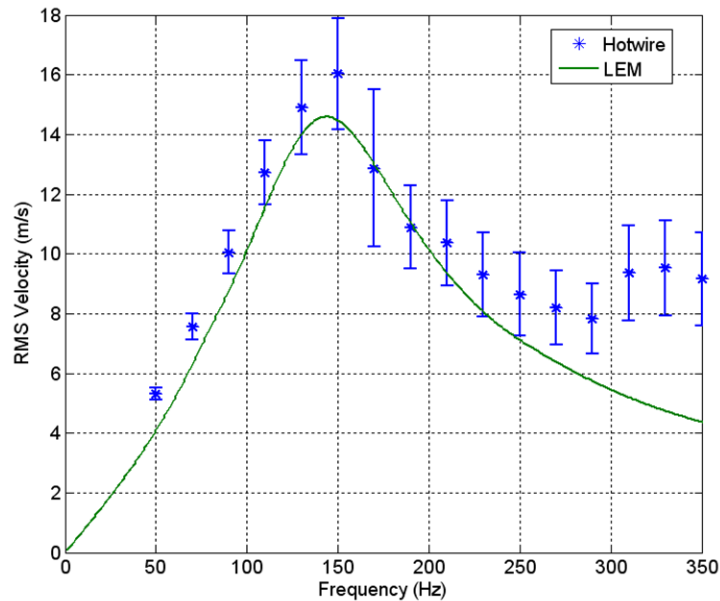


Figure 4-13. Model predicted and experimentally measured output velocity of the speaker-driven ZNMF actuator for 3V pp voltage input

It can thus be concluded that the LEM developed in Chapter 3 provides a powerful tool for analysis and prediction of the performance of ZNMF actuator. However, the LEM was validated only for an actuator where many important lumped parameters were extracted experimentally. The next section presents the fabrication method and validation of a composite diaphragm ZNMF actuator. The models for both the magnetic assembly and mechanical structure developed in Chapter 3 are used to predict the device performance.

4.2 Fabrication of Custom ZNMF Actuators

This section describes the fabrication of a custom-built, ZNMF actuator, as shown in Figure 4-14. The actuator consists of three major components—a magnetic assembly for creating a static magnetic field, a movable composite diaphragm/coil assembly for creating fluid motion, and a cavity with an orifice (or slot) through which the fluid is expelled or injected.

The magnetic assembly comprises permanent and soft magnets to establish a fixed, uniform magnetic field across the coil windings. A multi-turn, multi-layer solenoidal coil of total length L_{coil} resides in the annular air gap. The moveable portion of the ZNMF actuator consists of an axisymmetric composite diaphragm clamped at its outer edges. The rigid central boss has a radius b and the outer annular compliant region has an outer radius of a . The thickness of the diaphragm is h . The solenoidal coil is rigidly affixed to the central boss. The diaphragm forms the bottom portion of a sealed cavity of length L_c . The top of the cavity is bounded by a rigid plate containing an orifice (or slot). A circular orifice with radius a_{os} and length L_{os} is shown in the schematic.

Many of the sub-components in the actuator—the housing, diaphragm central boss, cavity, and orifice (or slot) structure—were rapid prototyped using a ZCorp Z415 3D printer. The resulting material is a composite powder that is held together by a binder. The material is

extremely light and sturdy. Thus the housing pieces do not contribute significantly to the overall mass of the actuator; in fact, most of the total mass of the actuator arises from the magnetic assembly. The overall density of the binder material was measured to be 1190 kg/m^3 . The manufacturing tolerances in the 3D printing process decide several key dimensions of the actuator. Thus the lower limits on the cavity length, the orifice (or slot) dimensions and the rigid center boss thickness are set by the tolerances of the 3D printing. Both the vertical and lateral tolerances on the Z415 are $\pm 0.05 \text{ mm}$. In addition to the 3D printer tolerances, the minimum dimensions were restricted to ensure repeatability of the manufacturing process and maintain structural strength of all the parts built. Based on these limits, the smallest diaphragm/central boss thickness was limited to 1 mm , the minimum cavity length was set to 3 mm , and the minimum slot/orifice dimensions were 0.5 mm .

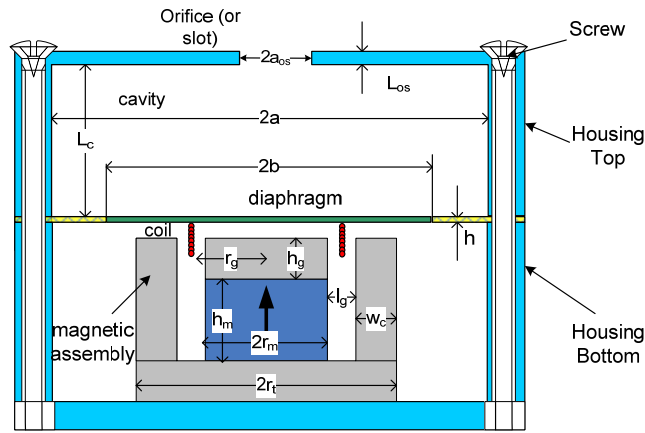


Figure 4-14. Schematic of Polydimethylsiloxane (PDMS) composite diaphragm actuator

4.2.1 Magnetic Assembly

The primary objective of the magnetic assembly is to produce a large, constant magnetic field in the annular air gap. The two most commonly used high-performance permanent magnet materials are neodymium-iron-boron (NdFeB) and samarium cobalt (SmCo). From the 1-D magnetic circuit model developed in section 3.3.1, it was seen that material with high coercivity

H_c and remnant magnetic flux density B_r should be used to obtain large magnetic flux density in the air gap. Hence NdFeB magnets (from K J Magnetics) were used, as they have the highest remnant magnetic flux density among commercially available magnets (1.3 T). The soft magnetic material in the magnetic assembly provides a low reluctance path for the magnetic flux. Hence soft magnetic material with very large relative permeability should be selected. Here, EFI50 (nickel-iron alloy) from Ed Fagan Industries with relative permeability of 100,000 was used [40]. In addition, EFI 50 also has relatively high saturation magnetization of 1.45 T.

The hard magnet was purchased at a specific size, and the soft magnetic core pieces (top, bottom and annular piece) were conventionally machined to the desired dimensions. All the pieces of the magnetic assembly were held together using a two-part epoxy. The geometrical dimensions of the magnetic assembly were chosen to keep the final actuator device confined to a size of approximately a 25 mm on a side. The final dimensions of the magnetic assembly are shown in Figure 4-15, along with a photograph of the magnetic assembly sitting within the bottom housing of the actuator. The magnetic assembly is attached to the bottom housing piece using a two-part epoxy.

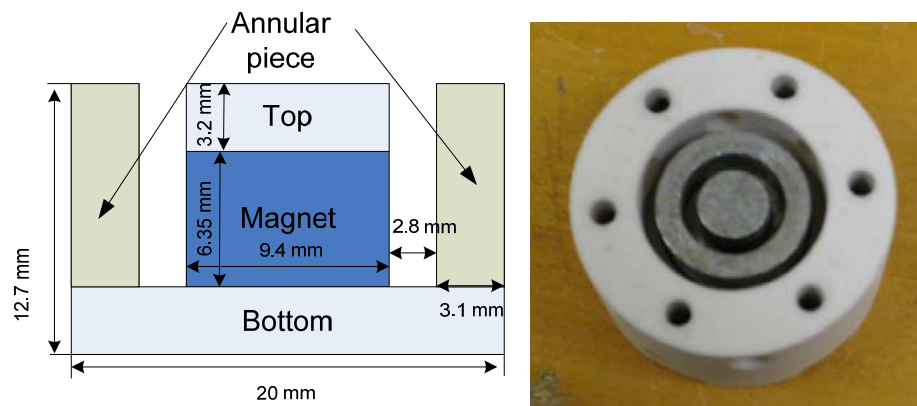


Figure 4-15. Magnetic assembly schematic and photograph

4.2.2 Diaphragm Assembly

The diaphragm assembly is the most complex component of the actuator. Fabrication was achieved using a multi-step process—the rigid center boss and the coil assembly were fabricated first, followed by assembly with the PDMS to form the composite diaphragm.

In order to ensure that the PDMS adheres well to the center boss, a two-flange design was employed in the center boss, as detailed in Figure 4-16. During assembly of the diaphragm, the liquid PDMS would flow between the flanges, providing a reliable connection. The overall diameter of both the flanges was set to $2b$ as decided by the desired solidity ratio. The two discs were connected together by a central region with a diameter of b . Six additional smaller outer posts around the periphery provided additional supporting structures to which the PDMS could attach. Note that the dimensions of the central post and the outer posts are not critical as long as the overall structural integrity and rigidity of the central boss is ensured. The entire structure was rapid prototyped using the ZCorp Z415 3D printer.

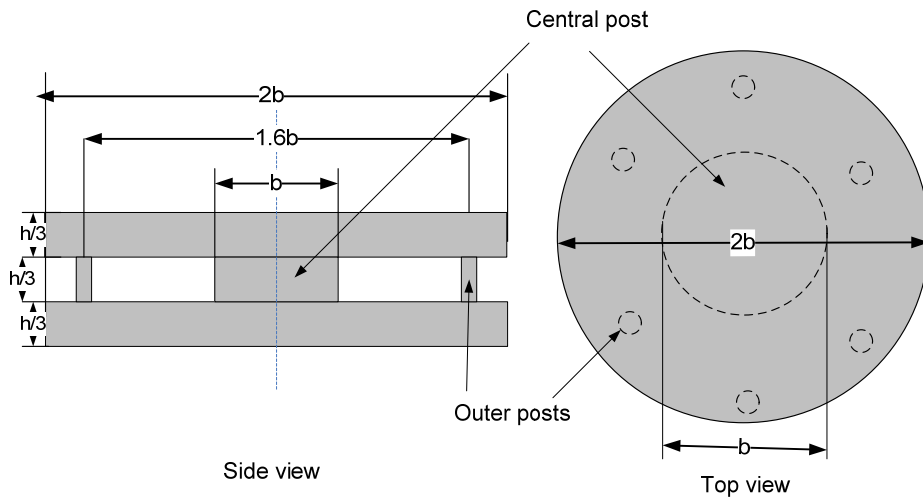


Figure 4-16. Two-flange design for the rigid central boss

The coil winding was formed using bondable copper wire from MWS Wire Industries [53]. The required number of coil turns were wound on a cylindrical post of desired coil diameter. The

copper wire has a thin coating of Polyvinyl Butryl, which is a thermoplastic adhesive. When the adhesive is heated to 130°C, it binds the coil windings together, and the self-supporting coil is then slid off the winding post. The coil was then attached to the diaphragm central boss using a two-part epoxy. Several different coil configurations were manufactured, as will be described later. Figure 4-17 shows photographs of the coil and the rigid center boss.

The annular compliant portion of the composite diaphragm was fabricated using PDMS. PDMS is a silicon-based organic polymer elastomer material. It is very suitable as a structural material because it is very compliant (Young's Modulus in the 100 kPa – 760 kPa range [54]) and thus can enable in large displacements for a small forces. PDMS is a viscoelastic silicon-based organic polymer material that conformally reflows when poured into a mold. After curing, it behaves as an elastic solid. Dow Corning Sylgard 184 Elastomer Kit was used in this work. The kit consists of an elastomer base and a curing agent, which are mixed in 10:1 weight ratio. The mixture was allowed to degas for 30 minutes before pouring into molds (fabricated using the 3D printer) to form the diaphragms. This prevented the formation of bubbles in the PDMS during the curing process. During the curing process, the polymer chains in the PDMS cross-link making the material stiffer. The final material properties are a function of the curing temperature and curing time [54]. A 2 hour cure at 50°C on a hotplate was used for this work.



Figure 4-17. Diaphragm components

To form the diaphragm assembly, the PDMS mixture was poured into to a shallow mold. The central boss was placed, centered into the uncured PDMS and centered using the centering mechanism as shown in Figure 4-18. The PDMS was then cured at 50 °C for 2 hours. Note the PDMS mold has eight posts to create holes in the PDMS layer to accommodate the screws for the final assembly. After the curing process is completed, the diaphragm was removed from the mold, with the central boss/coil attached as shown. The photographs of the mold and the released diaphragm-coil assembly are shown in Figure 4-19. Finally, the diaphragm was placed between the two housing pieces. The bottom housing holds the magnetic assembly, and the top housing forms the cavity/slot. Both these pieces have through holes on the edges that align with the holes in the diaphragm. The photograph of the fully assembled device with a 2D-slot is shown in Figure 4-20.

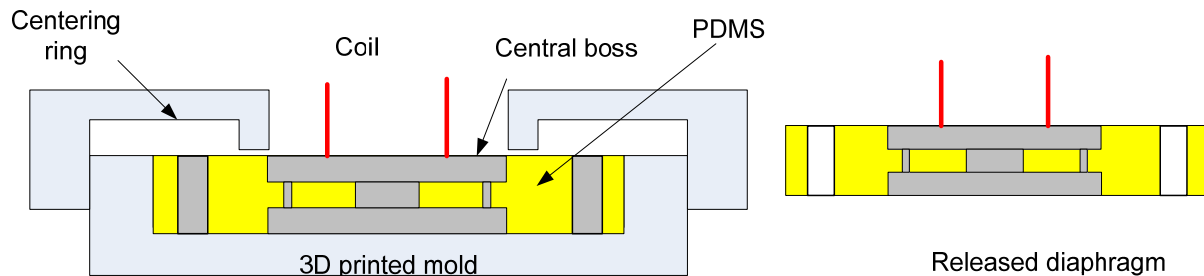


Figure 4-18. Centering ring for the central boss

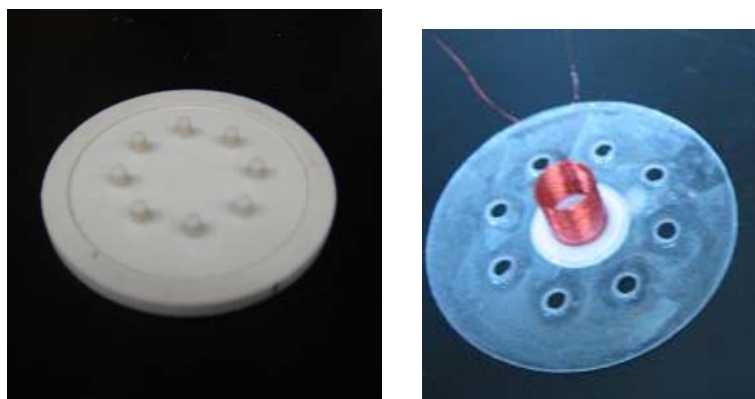


Figure 4-19. Mold for the PDMS diaphragm fabrication and released PDMS diaphragm with the rigid center boss



Figure 4-20. Fully assembled device

4.3 Model Validation

Before validating the overall model of the electrodynamic ZNMF actuators, several experiments were carried out in order to verify the models of the individual components of the ZNMF actuator. The coil electrical impedance was measured to verify the coil resistance and inductance (R_{eC} and L_{eC}). Similarly, experimental characterization of the diaphragm assemblies is very important in order to verify the diaphragm model. The acoustic compliance and the acoustic mass of the diaphragm are discussed in section 3.4.2. Two different characterization experiments were performed to experimentally verify the diaphragm model (with attached coils). First, the static center deflection was measured using a dc loading test to measure the center displacement. The center displacement of the PDMS diaphragm under a uniform pressure load was also measured. The resonant frequency and the diaphragm damping were then extracted using the impulse response measurements. The comparison between measured and model predicted resonant frequency will provide an independent but indirect validation of diaphragm model.

The material properties and the geometrical dimensions of the composite diaphragm are tabulated in Table 4-5. Based on these parameters, the lumped acoustic compliance, acoustic mass and resonant frequency of the diaphragm were calculated (section 3.4), as shown in Table 4-6. Note that this particular PDMS diaphragm and coil assembly is used in actuator A1.

The volume of the front cavity for the prototype actuators is 1.5 cm^3 and the total volume of the back cavity is nearly 12 cm^3 . Moreover, the bottom housing section has six large openings as can be seen from Figure 4-20. Thus it can be seen that the back cavity is at least 8 times larger than the front cavity and its effect can be neglected.

Table 4-5. Diaphragm material properties and geometry

Parameter	Value
Outer radius (a)	12.7 mm
Inner radius (b)	9.5 mm
Height (h)	1 mm
Young's modulus of the annular portion (E_2)	360 kPa [55]
Poisson's ratio of the annular portion (ν_2)	0.33
Density of the annular portion (ρ_2)	970 kg/m ³
Young's modulus of the central portion (E_1)	20 GPa[56]
Poisson's ratio of the central portion (ν_1)	0.33
Density of the central portion (ρ_1)	1190 kg/m ³
Mass of the coil (M_{coil})	0.31 g

Table 4-6. Model parameters for PDMS diaphragm corresponding to actuator A1

Parameter	1 inch diameter
Effective area (S)	$3.89 \times 10^{-4} \text{ m}^2$
Acoustic compliance (C_{ad})	$2.70 \times 10^{-10} \text{ m}^5/\text{N}$
Acoustic mass (M_{ad})	$5.08 \times 10^3 \text{ kg/m}^4$
Mass contribution of the coil (M_{coil}/S^2)	$1.85 \times 10^3 \text{ kg/m}^4$
Predicted resonant frequency (Hz)	151.7 Hz

4.3.1 Electrical Impedance Measurements

The electrical resistance of the coil can be calculated based on the number of turns, the average diameter of each turn and the gauge of the wire used. Thus, for 150 turn, 40 AWG turn with mean diameter of 10.6 mm is calculated to be 23 Ω . The coil resistance and inductance was measured using the Agilent 4294A precision impedance analyzer from 40 Hz – 1000 Hz. The

results of the resistance and inductance measurements are shown in Figure 4-21. At each frequency, 30 averages were used. The resistance of the coil is shown to be 25.2Ω and the inductance was measured to be 0.48 mH . Note that at the maximum frequency of interest here (500 Hz), the inductive portion of the coil impedance is 1.5Ω . Thus it can be seen that the inductive impedance of the coil even at the maximum frequency of interest is nearly 20 times smaller than the resistance of the coil. The magnetic assembly and the diaphragm were not used during this experiment.

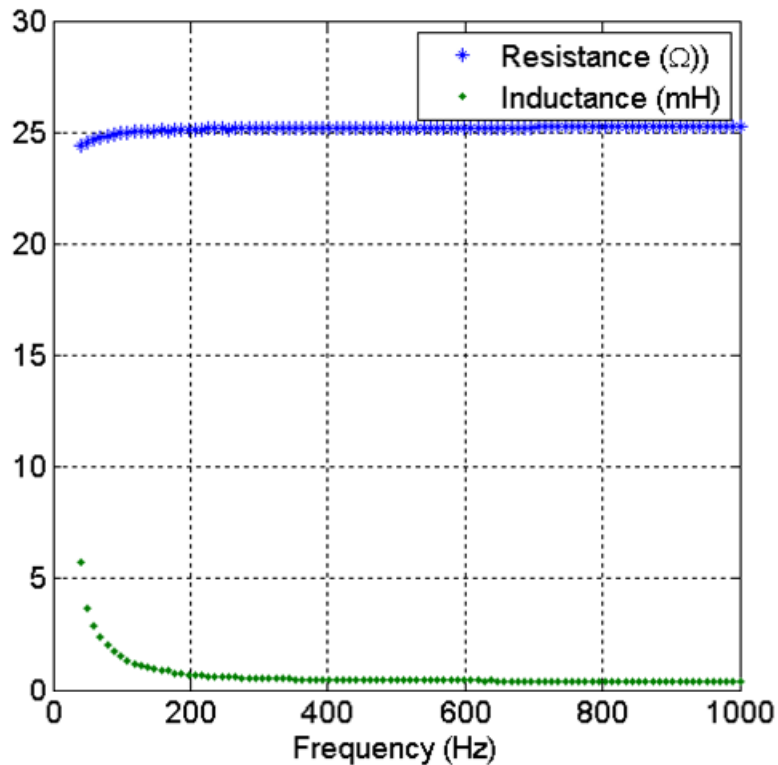


Figure 4-21. Impedance measurements of 150-turn 40 AWG copper coil without the magnetic assembly

4.3.2 Static Displacement Tests

The Lorentz force on the coil $F = BLI$. Thus if the coil is excited by a dc current a static force is applied on the diaphragm. The center deflection $w(0)$ of the diaphragm under this condition can be predicted from the model developed in Chapter 3 and is given below

$$w(0) = b_1^{(1)} \left(\frac{-b^2}{2} \right) - \frac{P(-b^4)}{64D_{11}^{(1)}} + b_1^{(2)} \left[\frac{b^2 - a^2}{2} - a^2 \ln \left(\frac{b}{a} \right) \right] + \frac{P}{64D_{11}^{(2)}} \left[4a^4 \ln \left(\frac{b}{a} \right) - b^4 + a^4 \right], \quad (4.111)$$

where the constants are detailed in the Appendix B. Note that this deflection assumes a uniform pressure load. The Lorentz force load on the coil is converted to an equivalent pressure as follows

$$P = \frac{F}{S} = \frac{BL_{coil}I}{S}. \quad (4.112)$$

Thus if the magnetic field B and the coil length L_{coil} are known, the applied force F is known for a given current I . Note that S is the effective area of the diaphragm. The radial magnetic flux density in the gap was measured using a Lakeshore 475 DSP Gaussmeter with a Lakeshore hall probe HMNT-4E04-VR. The average measured magnetic flux density in the air gap (B) was 0.33 T. This measured value matched well with finite element analysis of the magnetic assembly. The coil consists of 150 turns of 40 AWG copper wire. The average diameter of the coil was 10.6 mm, making the total coil length 6.7 m. All the electrical and magnetic parameters of the magnetic assembly are tabulated in Table 4-7.

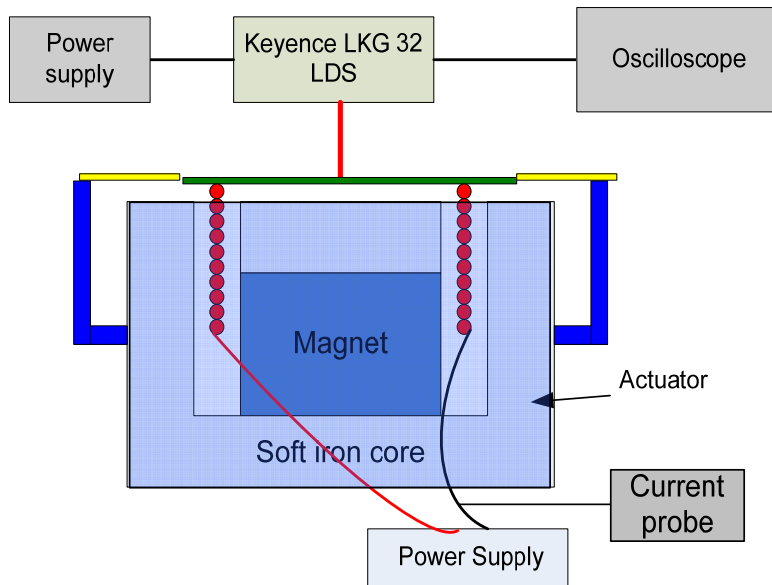


Figure 4-22. Setup for dc displacement test and the step response test

Table 4-7. Electrical and magnetic parameters

Number of coil turns	150
Coil resistance (R_{eC})	25.2 Ω
Coil Inductance (L_{eC})	0.48 mH
Coil length (L_{coil})	6.7 m
Magnetic field in the gap (B)	0.33 T
Maximum current	110 mA

For the testing, the coil was excited using a DC current source, and the current through the coil (I) was measured. The displacement of the diaphragm was measured using the Keyence LKG 32 laser displacement sensor. The test was performed for a range of currents up to the maximum allowable current through the coil (110 mA for 40 AWG copper wire). The force was calculated using the Lorentz force equation ($F = BL_{coil}I$), and the equivalent acoustic pressure corresponding to each case was calculated using (4.112).

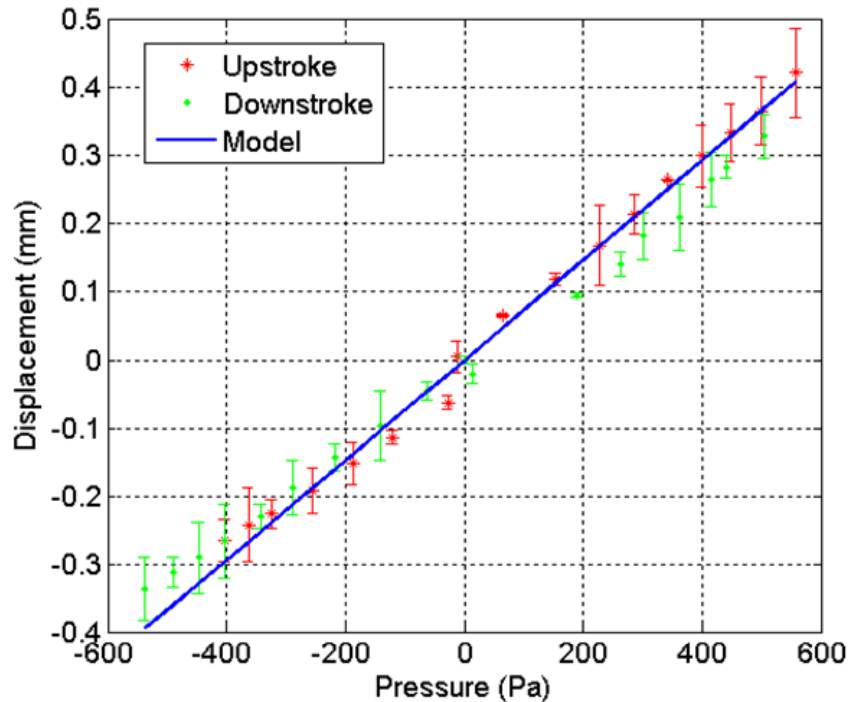


Figure 4-23. DC displacement test results

Figure 4-23 shows the measured and predicted values of the center displacement as a function of the applied equivalent pressure. The displacement was measured 31 times at each

applied pressure and the uncertainty estimates calculated are also indicated on the plot. The displacement is fairly linear with respect to applied pressure and matches very well to the model predicted displacement.

The center displacement was also measured by loading the diaphragm by a uniform pressure. The experimental setup for this measurement is shown in Figure 4-24. The setup consists of a vacuum chamber whose one wall was formed by the diaphragm under test. A vacuum was generated in the chamber by means of a small electric motor. The pressure inside the chamber was measured using a Heise ST-2H pressure gauge. The diaphragm which forms one wall of the chamber was clamped in between two annular magnets as shown. The displacement of the diaphragm was measured using the Keyence laser displacement sensor as described in the previous experiment.

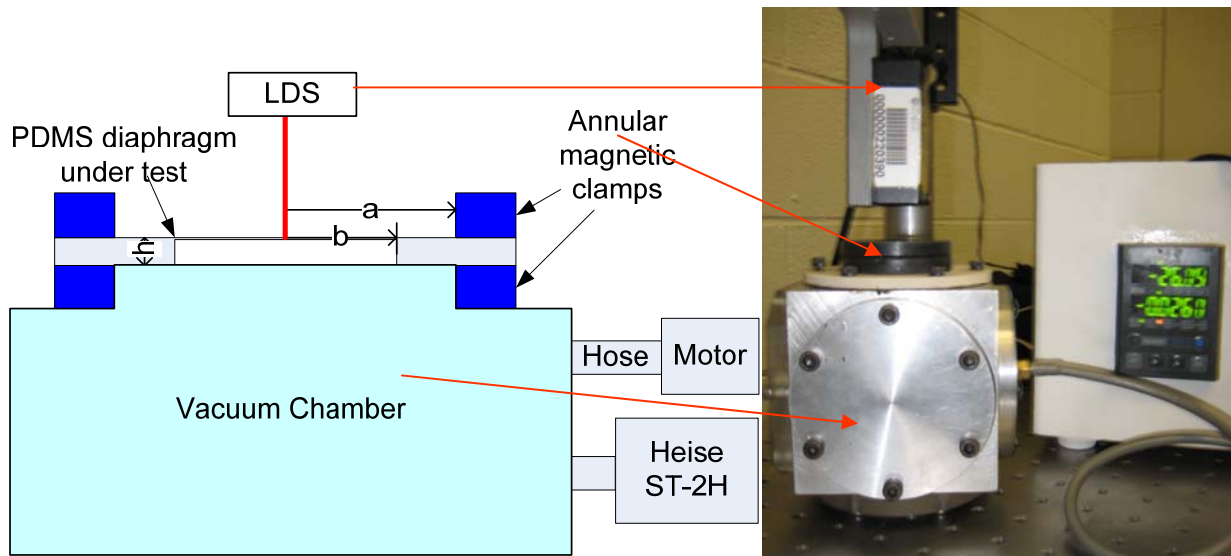


Figure 4-24. Displacement measurement under pressure load

Figure 4-25 shows the displacement as a function of the pressure. The comparisons with the model predictions are also shown in the same plot.

It can be seen that the model matches the experimental data well. Note that due to the limitations of the experimental setup, the displacement of the diaphragm could not be measured

over the range of displacements that were observed during the device operation. A better experimental setup with a better control of the pressure inside the chamber will be necessary to characterize the static displacement profiles more completely. In addition, a setup with means to pressurize as well as to establish a vacuum in the chamber can be used to study any hysteresis behavior present.

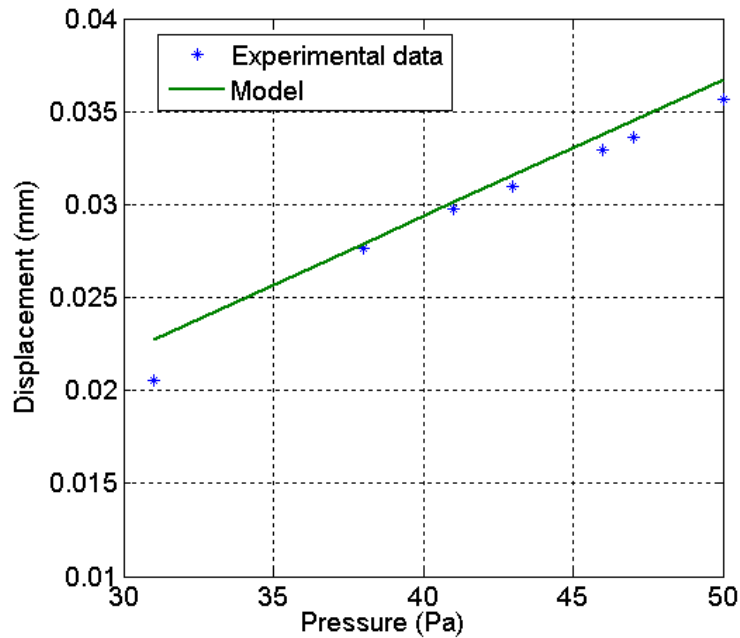


Figure 4-25. Displacement measurements under uniform pressure load

Table 4-8. PDMS diaphragm parameters for actuator A1

Parameter	Value
Extracted resonant frequency	143.7 Hz
95 % Confidence intervals (frequency)	142.8 – 144.6 Hz
Model predicted resonant frequency	151 Hz
Extracted damping ratio	0.015
95 % Confidence intervals (Damping ratio)	0.0146 - 0.154
R^2	0.9476
Diaphragm damping (R_{ad})	1.3×10^5 N-s/m ⁵

It can be seen from the dc displacement test (Figure 4-23) and the pressure loading test (Figure 4-25) that the composite diaphragm model predicts the center displacement accurately. Moreover, the resonant frequency measured using the step response test is within 5 % of that

predicted by the model (Table 4-8). This indicates that the diaphragm model is reliable and can be used to predict the overall response of the ZNMF actuator.

4.3.4 Hotwire Measurements

The purpose of the lumped element model of the electrodynamic ZNMF actuator is to predict output velocity obtained from the jet. The previous sections discussed verification of the diaphragm model and extracted the diaphragm damping. This section discusses the validation of the overall model by measuring the output velocity from the jet using hotwire anemometer measurements. The general experimental setup, calibration and procedure for the hotwire measurements were described in section 4.1.2.

Table 4-9. Device configuration for hotwire tests

Actuator	A1	A2	A3
Magnetic flux density in the gap (B) T	0.4	0.4	0.4
Length of the coil (L_{coil}) m	6.6 (150 turns, 40 AWG)	4.5 (90 turns, 34 AWG)	4.5 (90 turns, 34 AWG)
Solidity ratio (b/a)	0.75	0.75	0.75
Effective area (A_d) m ²	3.89×10^{-4}	3.89×10^{-4}	3.89×10^{-4}
Transduction factor (G) Pa/A	6.8×10^3	4.62×10^3	4.62×10^3
Resistance of the coil (R_{ec}) Ω	23.3	3.8	3.8
Equivalent electrical resistance (G^2/R_{ec}) N-s/m ⁵	1.28×10^6	5.62×10^6	5.62×10^6
Mass of the coil (M_{coil}) g	0.56	0.31	0.31
Predicted resonant frequency (f_{res}) Hz	151	177	177
Extracted resonant frequency (f_{res}) Hz	144	167	167
Extracted damping ζ	0.015	0.012	0.013
Slot/orifice geometry	24 mm x 1 mm x 1mm slot	24 mm x 1 mm x 1mm slot	2 mm diameter x 1 mm deep orifice
Maximum current (rms) (mA)	110	330	330
Maximum input power (mW)	200	400	400

Hotwire results for three different actuators are discussed here. The only difference in the three devices was the coil and slot configurations; the diaphragm, cavity, and magnetic assembly dimensions, were identical. The geometries are summarized in Table 4-9. Figure 4-26 - Figure 4-

28 show the hotwire results for the three devices. 100 blocks of data were used to obtain the error estimates and the bounds on the data based on (4.113) and (4.114). The error estimates for each frequency were obtained by analyzing the time data at each frequency. The normalized random error ε_r for the measurement is given by [52]

$$\varepsilon_r = \frac{\sigma}{\phi} \quad (4.113)$$

where σ is the standard deviation of the measurement and ϕ is the mean of the measurement.

The 95 % confidence interval for the mean of the measurement is given by

$$B = \frac{2\sigma}{\sqrt{N}} \quad (4.114)$$

where N is the number of independent observations. This is obtained from the t-distribution and assuming that number of independent observations N is greater than 31. Thus the mean of the measurement is bounded by $\phi - B \leq \phi \leq \phi + B$. (Here, $N = 100$). The overall rms and mean errors for each of the actuators were calculated. The maximum rms error was calculated to be 11.3 %, and maximum mean error was 9.8 %. The model predictions for both the devices are also shown in the plots. The hotwire results indicate that the lumped element model predicts the resonant frequency of the device well. Note that device 2 has a much “broader” peak around the resonant frequency. This is because of the difference in equivalent electrical damping in the two devices as shown in Table 4-9.

The resistance of the coil for device A1 and device 2 is 23 Ω and 4.5 Ω respectively. Thus when this resistance is referred to the acoustic domain, the equivalent electrical damping for device 2 is much higher than for device A1. Device A3 shows even “flatter” frequency response because in addition to extra electrical damping, this device also has higher fluidic resistance (R_{aOS} and R_{aO}). In all three cases, the model predicts the behavior of the device up to the resonant frequency extremely well. At higher frequencies the deviation from the model predictions is

higher. This may be due to non-linear effects in the composite diaphragm, magnetic assembly, fluidic components etc.

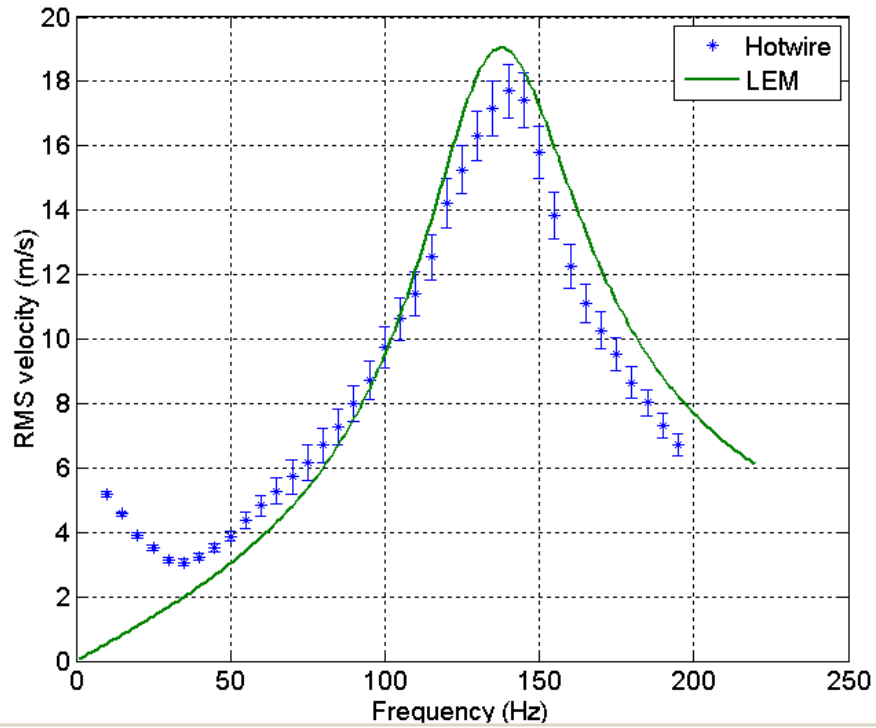


Figure 4-26. Hotwire results and model comparisons for device A1

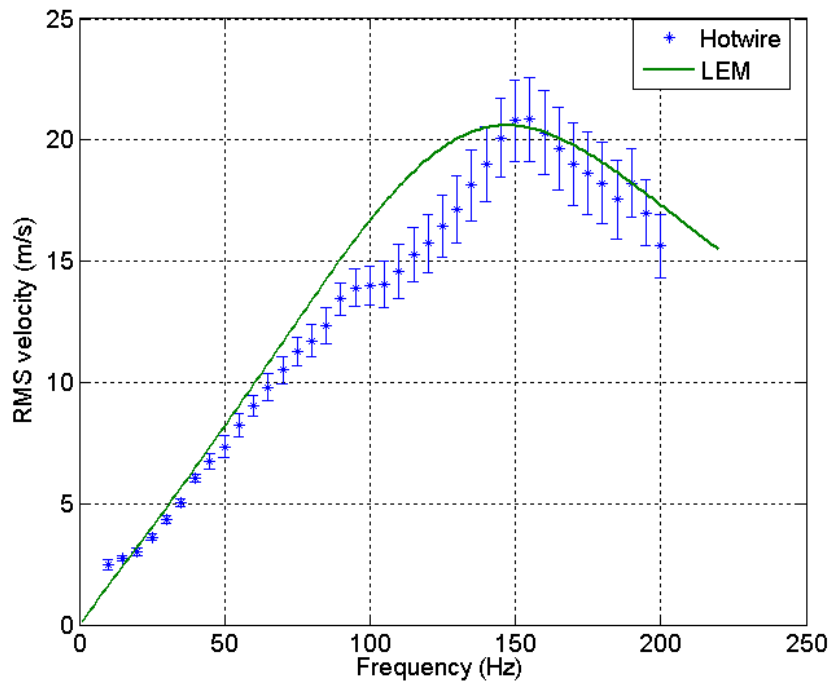


Figure 4-27. Hotwire results and model comparisons for device A2

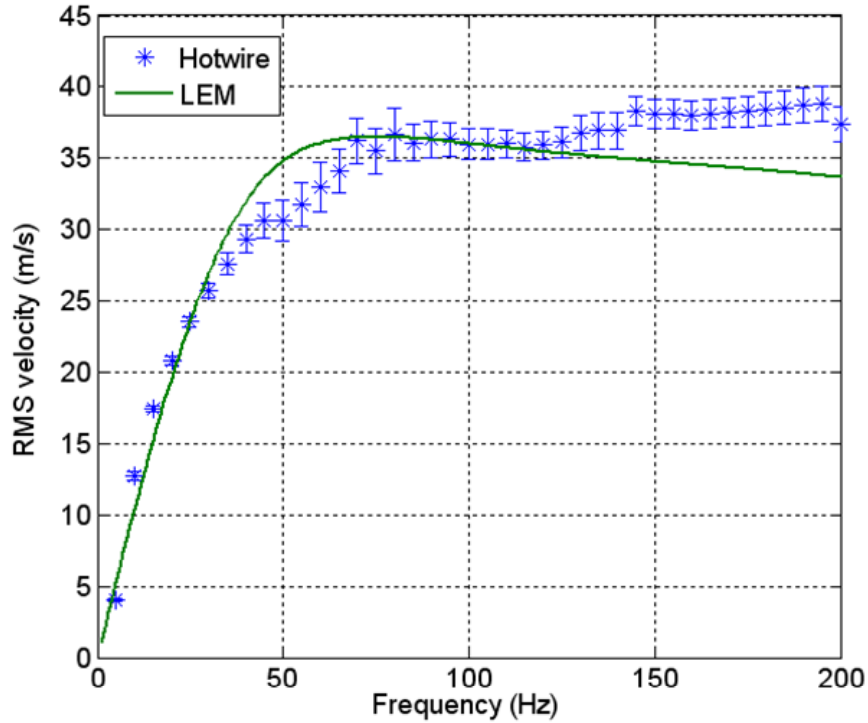


Figure 4-28. Hotwire results and model predictions for device A3

In almost all actuators, the overall damping is constant. ZNMF actuators are unique in this respect because the damping is frequency dependent that due to the non-linear slot/orifice resistance (R_{aO}), the damping is frequency dependent. Figure 4-29 shows the relative magnitudes of the slot/orifice damping and the total damping for device A1. Table 4-10 shows the relative magnitudes of various damping components in the three actuators.

Table 4-10. Various components of the damping

Damping term	Actuator A1	Actuator A2	Actuator A3
Equivalent electrical damping (G^2/R_{ec})	1.28×10^6	5.62×10^6	5.62×10^6
Diaphragm damping (R_{aD})	1.3×10^5	0.9×10^5	1.1×10^5
Linear slot/orifice damping (R_{aOS})	0.4×10^5	0.4×10^5	0.85×10^5
Non-linear slot/orifice damping (R_{aO}) at resonance	5.1×10^5	2.7×10^6	2.9×10^6
Total damping	1.86×10^6	8.3×10^6	8.6×10^6

It can be seen that the diaphragm damping is very small portion of the overall damping in each of the actuators. For actuator A1, the equivalent electrical damping is constant with

frequency (G^2/R_{ec}) and forms the bulk of the damping ($1.28 \times 10^6 \text{ N-s/m}^5$). However, near the resonant frequency of the device, the slot damping term is at least 50 % of the equivalent electrical damping. Thus the total damping in the ZNMF actuator particularly near the resonant frequency is frequency dependent. Similar trends are also seen for actuators A1 and A2. This presents several challenges in design and optimization of these actuators as will be discussed in Chapter 5.

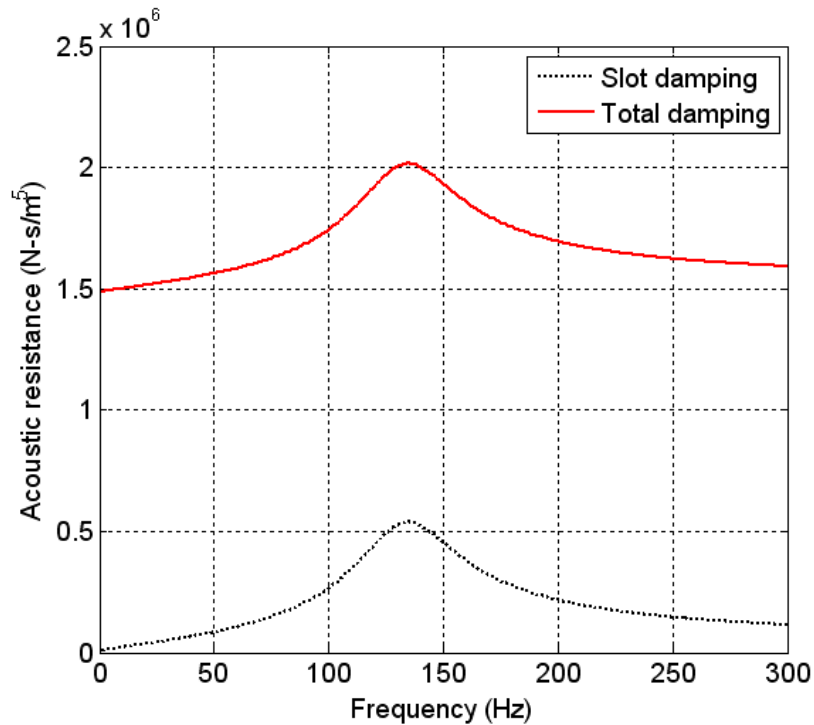


Figure 4-29. Relative magnitudes of the slot damping and the total damping for device A1

4.3.5 Summary

The model has been validated for three different electrodynamic ZNMF actuators. It can be seen that lumped element model developed is a very powerful predictive tool for analysis and design of electrodynamic ZNMF actuators. The only parameter extracted experimentally was the equivalent diaphragm damping. Several trends and tradeoffs can be inferred based on the models developed in Chapter 3 and the experimental results presented in Chapter 4. The parameters that

have the most effect on the device performance can also be identified. The electrical resistance of the coil determines the “breadth” of the velocity peak. The resonant frequency of the actuator is predominantly determined by the diaphragm dimensions. A more detailed discussion of various design trends and tradeoffs will be presented in Chapter 5.

The custom-built device is very compact, with a volume of $\sim 15 \text{ cm}^3$ and weight of about 80 g. The magnetic assembly is the heaviest component of the actuator with weight of about 50 g. The maximum power consumption of all three actuators was under 500 mW. Note that both the input and output power are a function of the drive frequency and the maximum occurs at the resonance.

A fabrication methodology for PDMS based composite diaphragms was presented. The fabrication methodology is very robust and cost effective. Moreover, the fabrication is modular where each of the components can be designed and then fabricated to meet the desired specifications of the actuator. In addition, the fabrication can be adapted to a wide range of sizes and thus much smaller actuators than the ones described in this work can be fabricated using this fabrication methodology.

CHAPTER 5 DESIGN AND OPTIMIZATION STRATEGIES FOR ELECTRODYNAMIC ZNMF ACTUATORS

Chapter 5 presents several design and optimization strategies for designing electrodynamic ZNMF actuators based on the lumped element model for these actuators developed in Chapter 3 and validated in Chapter 4. Section 5.1 outlines some of the challenges for design of ZNMF actuators. Section 5.2 presents detailed discussion of the performance of the electrodynamic ZNMF actuator in various frequency ranges. The design tradeoffs and trends for various performance parameters of a composite diaphragm ZNMF actuator developed in Chapter 4 are discussed in section 5.3. This section is divided into three major sections – the first section discusses the design methodology for the magnetic assembly, the next section discusses some trends, and the final section discusses tradeoffs involved in the PDMS diaphragm. Some system-level design tradeoffs are then presented. Section 5.4 presents a complete constrained optimization formulation for the composite diaphragm electrodynamic ZNMF actuator, including the choice of the objective function and sensitivity analysis of the optimized design to design variables.

5.1 Challenges in Design and Optimization of Electrodynamic ZNMF Actuators

As discussed in Chapter 2, two most important performance metrics of an actuator are blocked force and free displacement. Most actuator performance requirements such as maximum achievable force, maximum displacement, resonant frequency are dependent on application. Depending on the type of load that the actuator is driving, the desired performance characteristics are different. In order to optimize any given actuator performance, it is necessary to understand the loading on the actuator. Figure 5-1 shows the equivalent lumped-element circuit model for an electrodynamic actuator without a load impedance Z_{load} . The equivalent

acoustic domain representation of the electrodynamic actuator is shown in Figure 5-2. The details of circuit analysis to eliminate the gyrator were discussed in section 3.1.2.

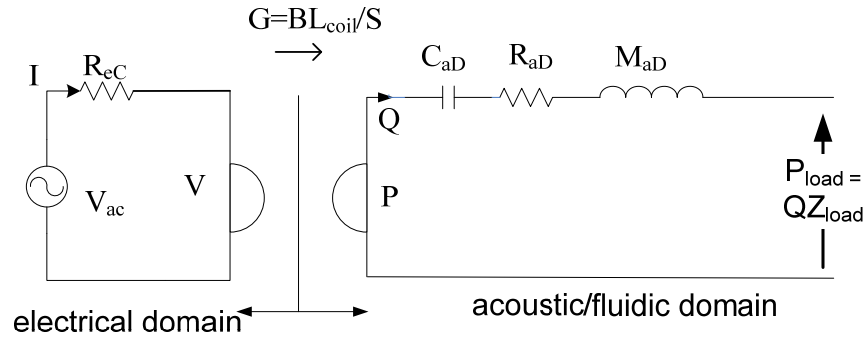


Figure 5-1. Loaded electrodynamic actuator

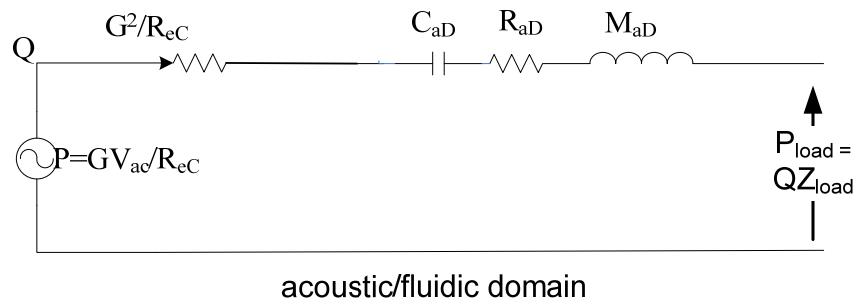


Figure 5-2. Electrodynamic actuator circuit referred to the acoustic domain

In many cases, the load consists of series-connected resistive and reactive components where the total load impedance can be expressed $Z_{load} = R_{load} + j\omega M_{load} - \frac{j}{\omega C_{load}}$. If so, the output volume velocity Q generated by the actuator is

$$Q(\omega) = \frac{P}{G^2/R_{eC} + R_{aD} + R_{load} + j\omega M_{aT} + 1/j\omega C_{aT}}, \quad (5.115)$$

where ω is the frequency of operation and C_{aT} and M_{aT} are the overall acoustic compliance and acoustic mass respectively. The total acoustic compliance and acoustic mass are

$$C_{aT} = \frac{C_{load}C_{aD}}{C_{load} + C_{aD}}, \quad (5.116)$$

and

$$M_{aT} = M_{aD} + M_{load}. \quad (5.117)$$

Note that in the case of a ZNMF actuator, there is the additional branch due to the compliance of the cavity (C_{acav}). However, for low frequency operation and compact cavities, the impedance of the cavity is very high and is ignored for simplified analysis.

A typical velocity (or volume velocity) vs. frequency curve for a second-order system is shown in Figure 5-3. The low-frequency response of the actuator is dominated by the acoustic compliance, and the high frequency response is determined by the total acoustic mass as indicated by (5.115).

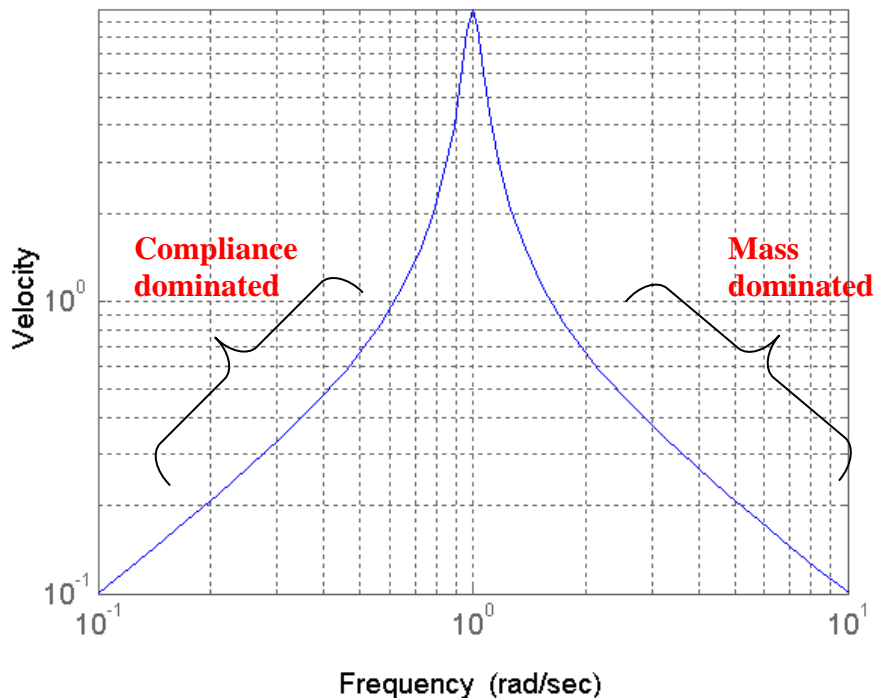


Figure 5-3. Typical velocity frequency response of a second-order system

At dc, the volume velocity (or velocity) generated by the actuator goes to zero. Thus at dc the change in volume or volume displacement achieved by the actuator is an important

performance metric. The dc volume displacement is determined by the total acoustic compliance of the overall system, and the resonant frequency is determined by the overall system dynamics as follows

$$|\Delta V|_{f \rightarrow 0} = C_{aT} P, \quad (5.118)$$

and

$$f_{res} = \frac{1}{2\pi\sqrt{M_{aT}C_{aT}}}, \quad (5.119)$$

where ΔV is the volume displacement, P is the applied pressure and C_{aT} and M_{aT} are the total acoustic compliance and acoustic mass, respectively. The product of dc volume displacement and the resonant frequency for a second-order system—the “gain-bandwidth” product—is an important performance metric[57]. Here, this is given by

$$|\Delta V|_{f_{res}} = \frac{1}{2\pi} \sqrt{\frac{C_{aT}}{M_{aT}}}. \quad (5.120)$$

Thus a common objective function used for actuator optimization is the maximization of the volume displacement-resonant frequency product. However, depending on the load requirements, other objective functions may be chosen.

In contrast to the simple formalism described above, the design of ZNMF actuators is more complicated for several reasons. First, the load impedance is not represented by a simple RLC network. The load consists of the parallel combination of the cavity compliance and the slot/orifice impedance as discussed in Chapter 3 (section 3.6, Figure 3-20). Thus, a ZNMF actuator does not, in general, reduce to a second-order system. For this work, however, compact actuators are considered, and the low frequency performance of the ZNMF actuator is of interest. Hence the cavity compliance can be ignored (assumed infinitely stiff), and the ZNMF actuator can be reduced to a nominal second-order system.

Second, the load impedance is nonlinear, as discussed in section 3.5.2; specifically, the dump loss resistance R_{dO} is dependent on the output volume velocity. Thus a simple “gain-bandwidth” type metric cannot be easily defined for these actuators. As the output volume velocity increases, the non-linear dump-loss resistance increases driving the output volume velocity lower. Thus the output volume velocity is calculated iteratively and a linear input-output transfer function cannot be defined. In other words, the slope of the volume velocity vs. frequency in the compliance dominated region (especially for frequencies near the resonance) is dependent on the input signal.

Another key challenge for ZNMF actuators is identifying an appropriate objective function that maximizes the fluidic impact of these actuators. Since the application of ZNMF actuators in flow control is still an ongoing research topic, the specific needs are not well documented. Gallas et al. [58] presented optimization strategies for improving the performance of piezoelectric ZNMF actuators for flow control applications. The authors investigated two different objective functions—(i) maximizing the total velocity over a range of frequencies and (ii) maximizing the velocity at a specific frequency. They also divided the optimization problem into two separate problems—(i) optimization of the orifice and cavity for a given piezoelectric driver and (ii) optimization of the piezoelectric driver independent of the slot and cavity configuration.

Chapter 5 first investigates the actuator performance in various frequency regimes based on the lumped element model developed. In ZNMF actuators, the magnetic assembly and mechanical structure can be designed almost completely independently. These sub-components impact different performance parameters of the actuator. Hence these sub-components are investigated individually to identify various trends and limitations. The overall system-level tradeoffs are then presented. To ensure maximum fluidic impact from these actuators three

different objective functions are investigated before choosing the most appropriate one. The magnetic assembly and the diaphragm are then individually investigated. Although the design tradeoffs and limits presented here are specific to the topology of the actuator chosen, the overall strategy is generic and can be adapted to any actuator configuration.

5.2 Frequency Dependence of Actuator Performance

The overall lumped element model for the electrodynamic ZNMF actuator was developed in section 3.6. The output response function of the ZNMF actuator was given by (3.61) and is included here again

$$\frac{Q_{out}}{V_{ac}} = \frac{sGC_{aD}/Z_{eC}}{\left[\frac{G^2}{Z_{eC}} sC_{aD} + (R_{aD} + sM_{aD})sC_{aD} + 1 \right] \left[C_{aCav}M_{aO}s^2 + C_{aCav}(R_{aOS} + R_{aO})s + 1 \right] + (R_{aOS} + R_{aO} + sM_{aO})sC_{aD}} \quad (5.121)$$

For compact actuators, the cavity volume V is chosen to be small, and hence the cavity compliance is also small. Thus for operating frequencies below the Helmholtz frequency of the cavity, the cavity impedance Z_{aCav} is very high. The validity of ignoring the cavity impedance essentially depends on the relative magnitudes of the cavity impedance (Z_{aCav}) and the total slot/orifice impedance (Z_{aOS}). It should be noted that the slot/orifice impedance is not only frequency dependent but also amplitude dependent. In this work, compact cavities are chosen. Hence for all cases, $Z_{aCav} \gg Z_{aOS}$, and thus ignoring the cavity impedance is reasonable. It should be noted that at frequencies closer to the Helmholtz frequency of the cavity and slot/orifice, the cavity can no longer be ignored.

The equivalent circuit thus reduces to a single loop and the output response function in this case can then be simplified to

$$\begin{aligned}
\frac{Q_{out}}{V_{ac}} &= \frac{(G/R_{eC})}{\left[\frac{G^2}{R_{eC}} + Z_{aD} + Z_{aOS} \right]} \\
&= \frac{(G/R_{eC})}{\frac{G^2}{R_{eC}} + \left[R_{aD} + sM_{aD} + \frac{1}{sC_{aD}} \right] + (R_{aOS} + R_{aRad} + R_{aO} + sM_{aO})} \quad (5.122) \\
&= \frac{(G/R_{eC})sC_{aD}}{s^2(M_{aD} + M_{aO})C_{aD} + sC_{aD} \left(\frac{G^2}{R_{eC}} + R_{aD} + R_{aOS} + R_{aRad} + R_{aO} \right) + 1}
\end{aligned}$$

The resonant frequency of the ZNMF actuator is given by

$$f_{res} = \frac{1}{2\pi\sqrt{C_{aP}(M_{aP} + M_{aO})}}. \quad (5.123)$$

A larger compliance and total acoustic mass will result in a lower resonant frequency.

The output response function of the ZNMF actuator can be further simplified for various frequency regimes. In the low frequency region, when the operating frequency is lower than the resonant frequency of the actuator ($f \ll f_{res}$), the contribution of the acoustic compliances is dominant, and the acoustic masses can be neglected. In this case, the output response function of the actuator can be simplified to

$$\left. \frac{Q_{out}}{V_{ac}} \right|_{f \ll f_{res}} \approx (G/R_{eC})sC_{aD}. \quad (5.124)$$

This can be further simplified by substituting for the transduction coefficient G and the coil resistance R_{eC} ,

$$\left. \frac{Q_{out}}{V_{ac}} \right|_{f \ll f_{res}} \approx (G/R_{eC})sC_{aD} = \frac{BL_{coil}}{S} \frac{A_{wire}}{\frac{\rho_{wire}L_{coil}}{1/R_{eC}}} sC_{aD} = s \frac{BA_{wire}}{\rho_{wire}} \frac{C_{aD}}{S}, \quad (5.125)$$

where B is the flux density in the air gap, S is the effective area of the diaphragm, L_{coil} is the total coil length and A_{wire} and ρ_{wire} are the cross-sectional area and resistivity, respectively, of the wire. It can be seen that the output volume velocity obtained from the actuator at low

frequencies increases linearly with the frequency. Moreover, in order to obtain large volume velocity at low frequencies, large values of magnetic flux density B and large C_{ad}/S are desired. Note however, if a large acoustic compliance is chosen to maximize the low frequency performance, the resonant frequency of the actuator will be lower. Also, the largest coil cross-sectional area should be chosen to improve the low frequency response.

At the resonant frequency of the device ($f = f_{res}$), the reactive component of the overall impedance is 0. Note that the equivalent circuit of the ZNMF actuator is actually a “two-loop” circuit. Thus the reactive component may not be exactly zero but very small. Thus the output response is given by

$$\left. \frac{Q_{out}}{V_{ac}} \right|_{f=f_{res}} = \frac{(G/R_{eC})}{\frac{G^2}{R_{eC}} + R_{aP} + R_{aos} + R_{aRad} + R_{aO}}. \quad (5.126)$$

For most ZNMF actuators, the equivalent electrical damping and the non-linear slot/orifice damping are the most dominant. Thus the output response can be further simplified to

$$\left. \frac{Q_{out}}{V_{ac}} \right|_{f=f_{res}} = \frac{(G/R_{eC})}{\frac{G^2}{R_{eC}} + R_{aP} + R_{aos} + R_{aRad} + R_{aO}} \approx \frac{(G/R_{eC})}{\frac{G^2}{R_{eC}} + R_{aO}} \approx \frac{(G/R_{eC})}{\frac{G^2}{R_{eC}} + \frac{1}{2} \frac{K_D \rho_0 Q_{out}}{S_{OS}^2}}, \quad (5.127)$$

where the expression for R_{aO} presented in Chapter 3 is substituted. It can be seen that the output volume velocity at resonance is a complex function of the actuator parameters.

For frequencies greater than the resonant frequency but lesser than the Helmholtz frequency of the cavity and the slot/orifice ($f_{res} \ll f \ll f_H$), the acoustic masses dominate the overall impedance of the actuator. The output response function in this case is given by

$$\left. \frac{Q_{out}}{V_{ac}} \right|_{f \gg f_{res}} \approx \frac{(G/R_{eC})}{\frac{G^2}{R_{eC}} + [R_{aP} + sM_{aD}] + (R_{aos} + R_{aRad} + R_{aO} + sM_{aO})} \approx \frac{(G/R_{eC})}{s(M_{aD} + M_{aO})}. \quad (5.128)$$

It can be seen that at high frequencies the output volume velocity decreases inversely with the frequency.

It can be seen from (5.122)-(5.128) that, to maximize the output of the actuator, the ratio G/R_{eC} is an important parameter. Moreover, the low frequency performance of the actuator is dominated by the acoustic compliance of the diaphragm. The performance in various frequency regimes and the desired characteristics of the actuator are summarized in Table 5-1.

Table 5-1. Output velocity in different frequency ranges and desired actuator characteristics

Frequency range	Output volume velocity (Q)	Desired device characteristics
Low frequency ($f \ll f_{res}$)	$\frac{GsC_{aD}}{R_{eC}}$	High G , High C_{aD} Low R_{eC}
At resonance ($f = f_{res}$)	$\frac{(G/R_{eC})}{\frac{G^2}{R_{eC}} + R_{aO}}$	High G , Low R_{eC}
High frequency ($f \gg f_{res}$)	$\frac{G}{R_{eC} s(M_{aD} + M_{aO})}$	High G , Low R_{eC}

Note that this analysis has been performed by assuming that the cavity impedance is much larger than the slot/orifice impedance. This assumption is not valid for higher frequencies, where the capacitive impedance of the cavity is not very high. Figure 5-4 shows the magnitude of the cavity impedance and the total slot impedance for the actuator A2 described in Chapter 4. The cavity impedance monotonically decreases with frequency. The predominant component of the slot impedance is the non-linear dump loss resistance, which is proportional to the output volume velocity. Thus the slot impedance shows a peak at near the resonance where the output volume velocity is high. It can be seen that the cavity impedance is at least 10 times higher than the slot impedance for frequencies up to 1000 Hz. Thus the fluid in the cavity behaves almost as an incompressible fluid. At higher frequencies, the compressibility effects will be significant and

thus the cavity cannot be ignored. Thus the assumption that the cavity impedance can be ignored is valid. (Note that the slot and cavity impedances are in parallel). Similar trends are seen for actuator A1 and A3 as well.

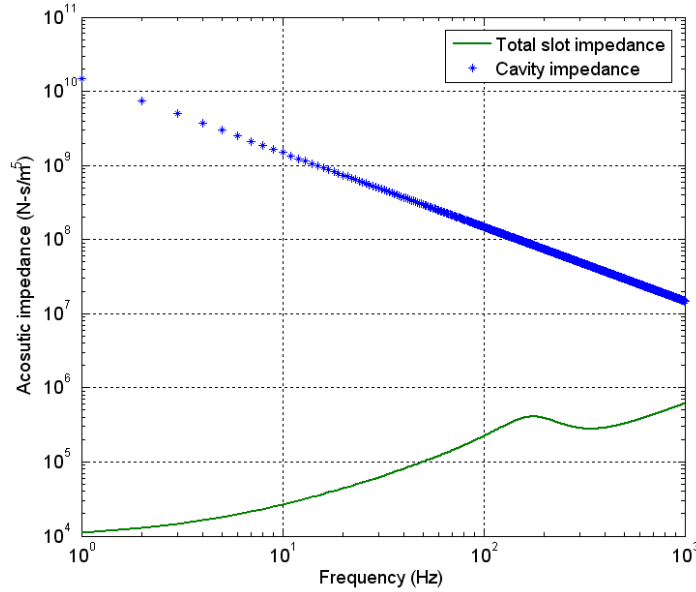


Figure 5-4. Comparison of the cavity and slot impedances for actuator A2

5.3 Design Tradeoffs for Composite Diaphragm Electrodynamic ZNMF Actuators

Chapter 4 presented the fabrication and model validation of a composite diaphragm ZNMF actuator. This section presents the general trends and tradeoffs affecting the overall performance of these actuators. The design tradeoffs for the magnetic assembly are discussed in section 5.3.1. In section 5.3.2, the variation of the lumped acoustic parameters for the composite diaphragms are first discussed, followed by discussion of the overall actuator performance.

5.3.1 Magnetic Assembly Design Tradeoffs

The magnetic assembly determines the maximum force (blocked force) produced by the actuator, as discussed in Chapter 2. The blocked force produced by the electrodynamic actuation scheme is given by

$$F_b = BL_{coil}I, \quad (5.129)$$

where B is the magnetic flux density in the coil, L_{coil} is length of the coil and I is the current through the coil. The cavity and slot impedance can be seen as the load against which the actuator has to act as shown in Figure 5-1. Thus in order to produce maximum output volume velocity, large blocked force is desired.

The 1-D magnetic circuit model to predict the magnetic flux density in the air gap was presented in section 3.3.1. The magnetic assembly with all the dimensions is shown in Figure 5-5. The magnetic flux density in the air gap is given by

$$B = \frac{H_c h_m}{\left(\frac{h_m A_{eff}}{\mu_0 \mu_{magnet} A_m} + \frac{l_g}{\mu_0} \right)}, \quad (5.130)$$

where H_c is the coercivity of the hard magnet, and A_m and A_{eff} are the area of the magnet and the effective area of the air gap.

Since neodymium-iron-boron magnets are used in this work, $\mu_{magnet} \approx 1$. Thus the magnetic flux density can be further simplified to

$$B = \frac{\mu_0 H_c}{\left(\frac{A_{eff}}{A_m} + \frac{l_g}{h_m} \right)} = \frac{\mu_0 H_c (A_m h_m)}{(A_{eff} h_m + A_m l_g)}. \quad (5.131)$$

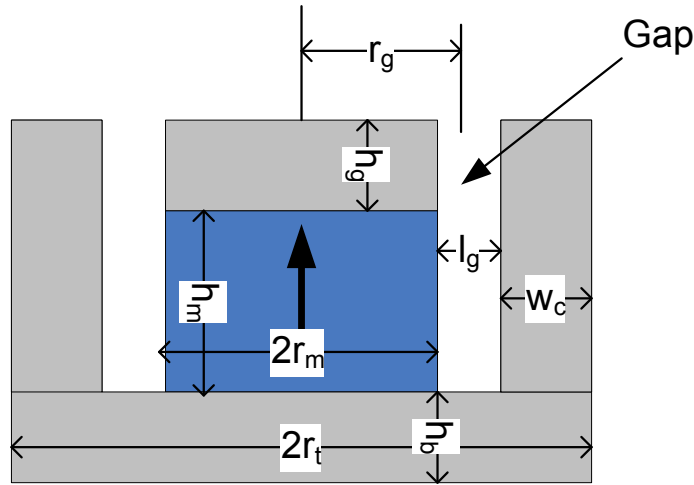


Figure 5-5. Magnetic assembly

Some interesting observations can be made based on (5.131). It can be seen that if it is desired to maximize the magnetic flux density in the air gap, the ratio of the areas of the air gap and the magnet should be minimized. In addition, the ratio of the length of the air gap to the height of the magnet should be minimized. Thus, in order to maximize the flux density, a magnet with the largest volume ($A_m h_m$) should be chosen.

By substituting (5.131) into (5.129), the blocked force is given by

$$F_b = \frac{\mu_0 H_c (A_m h_m) L_{coil} I}{(A_{eff} h_m + A_m l_g)} \quad (5.132)$$

Thus it can be seen that the blocked force is determined entirely by the magnetic assembly geometry and the length of the coil L_{coil} . The coil resides in the air gap of the magnetic assembly. Thus the length of the coil is not completely independent of the magnetic assembly geometry.

The relationship between the length of the coil and the gap geometry can be investigated by considering a multilayer coil winding as described in Chapter 4. The schematic of the coil configuration is shown in Figure 5-6. The diameter of the copper wire is d_{wire} , and the overall diameter of the wire with the insulation is d_{ins} .

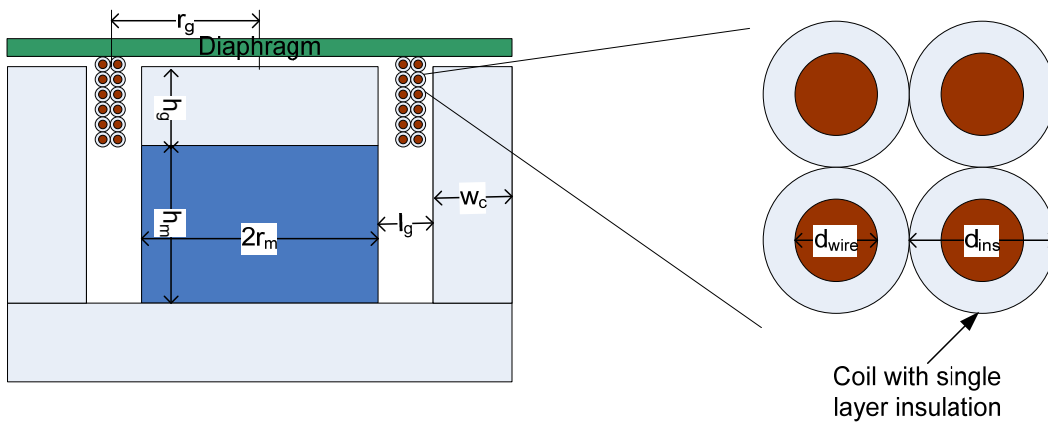


Figure 5-6. Coil configuration using a multiple layers of bondable copper wire

The length of coil is a function of the magnet assembly geometry and the number of turns.

The average length of each turn L_{turn} is given by

$$L_{turn} = 2\pi r_g = 2\pi (r_m + 0.5l_g). \quad (5.133)$$

Thus the total length of the coil with N_l layers and N_t turns per layer is given by

$$L_{coil} = N_l N_t L_{turn} = 2\pi N_l N_t (r_m + 0.5l_g). \quad (5.134)$$

The number of layers and the number of turns are also dependent on the magnetic assembly geometry. The maximum thickness and height of the coil are limited by the length of the gap l_g and height of the gap h_g , respectively. Thus the maximum limits on N_l and N_t are given by

$$N_l \leq \frac{l_g}{d_{ins}}, \quad (5.135)$$

and

$$N_t \leq \frac{h_g}{d_{ins}}. \quad (5.136)$$

The actual values of N_l and N_t are chosen to be the closest integer values smaller than the limits indicated above. Thus it can be seen that the gap size determines the coil configuration. The interaction between the coil configuration and the magnetic assembly design can thus be seen.

The wire cross-section diameter corresponds to its wire gauge (*AWG*) and can be chosen as one of the design variables. The empirical relationship between the wire gauge and the diameter of the wire (d_{wire} in mm) is given by [59]

$$d_{wire} = 0.127 * 92^{\frac{36-AWG}{39}} \quad (\text{in mm}). \quad (5.137)$$

The insulation thickness is usually dependent on the gauge of the wire chose. For this work, the coil wire gauge is restricted to be between 34 AWG and 40 AWG. For this range, the insulation thickness is 0.0076 mm [53]. Thus the overall diameter of the insulated wire is given by

$$d_{ins} = d_{coil} + 0.015 \quad (\text{in mm}). \quad (5.138)$$

The maximum length of the coil L_{coil} is given by

$$L_{coil} = N_t N_l (2\pi r_g) \leq \frac{l_g}{d_{ins}} \frac{h_g}{d_{ins}} (2\pi (r_m + 0.5l_g)). \quad (5.139)$$

Thus from (5.132) and (5.139), it can be seen that maximizing blocked force involves a coupled optimization of coil design and magnetic assembly design. If a very small gap is chosen, higher flux density can be achieved in the gap, but the length of the coil will be smaller and vice versa.

5.3.1.1: Optimization of the magnetic assembly to maximize the blocked force

As discussed in the previous section, there are conflicting design variables for maximizing the blocked force. This section presents the formulation of the optimization problem to maximize the blocked force. All the dimensions of the magnetic assembly and the wire gauge are chosen to be design variables as listed below

- Magnet radius (r_m)
- Magnet height (h_m)
- Height of the gap (h_g)
- Length of the gap (l_g)
- Wire gauge (AWG)

The design variable vector is thus mathematically represented as

$$\vec{X} = \{r_m, h_m, h_g, l_g, AWG\}. \quad (5.140)$$

The constraints used are

- Upper bounds on all geometrical dimensions to limit the size of the device to 30 mm diameter, 30 mm tall cylinder.
- Lower bounds on all geometrical dimensions to ensure that manufacturing limits are not violated.
- The length of the gap is constrained to be 50 % of the magnet height to ensure that the 1-D circuit model is valid.
- The power consumed in the coil is constrained.
- The overall mass of the magnetic assembly is also constrained.

Each of the design variables is bounded by upper and lower bounds. This can be mathematically stated as

$$\vec{L} \leq \vec{X} \leq \vec{U} \quad (5.141)$$

These bounds are defined in Table 5-2.

Table 5-2. Lower and upper bounds on the magnetic assembly design variables

Design variable	Lower bound (L)	Upper bound (U)
Magnet radius (r_m) (mm)	0.47	9.4
Magnet height (h_m) (mm)	0.635	12.7
Height of the gap (h_g) (mm)	1.6	9.6
Length of the gap (l_g) (mm)	1	8.5
AWG (gauge of the coil wire)	34	40

The magnetic permeability of the soft magnetic core material is very high and is ignored in the optimization as discussed in Chapter 3. The current density in the coil is assumed to constant and is limited by the maximum allowable Joule heating in the coil. The width of the annular soft magnetic piece (w_c) and the height of the bottom piece (h_b) are held constant at 5 mm. These dimensions mainly affect the weight of the device. However, making these dimensions too small may result in the saturation of the soft magnetic core. Finite element simulations of some typical magnet assembly geometry show that there is no saturation for these dimensions of the soft magnetic core. The details of the finite element simulations are included in Appendix A. All the constants used are summarized in Table 5-3.

Table 5-3. Constants used in the optimization formulation

Parameter	Value
Remnant magnetization of the hard magnet	1.2 T
Permeability of free space	1.25×10^{-6} H/m
Resistivity of copper	17.2×10^{-9} Ω m
Current density in the coil	4×10^7 A/m ²
Density of the hard magnetic material	7500 kg/m ³
Density of the soft magnetic material [40]	8180 kg/m ³
Height of the bottom soft magnetic piece	3.2 mm
Width of the annular soft magnetic piece	3.2 mm

The objective function is to maximize the blocked force. The *fmincon* function from the MATLAB optimization toolbox is used to implement this problem. As this optimization routine is set up to minimize a given objective function, the objective function is stated mathematically as follows

$$\text{Minimize: } f_{obj}(\vec{X}) = -F_b. \quad (5.142)$$

The optimization was first carried out with no power or mass constraints. In this case, the optimal design required the largest possible magnet and largest gap height to maximize the number of coil turns. The length of the gap was limited to 50 % of the magnet height as per the modeling constraint described above. The optimal design also required the largest wire cross-section (smallest *AWG*). The maximum blocked force obtained in this case was 5.84 N with power consumption of 20.8 W and mass of 208 g. Clearly, the power and mass limits in a practical actuator would likely be much smaller than these. Hence the optimal designs for various power and mass restrictions were studied.

Figure 5-7 shows the maximum achievable blocked force for various power constraints. The blue curve indicates maximum achievable blocked force when only the power is constrained and the magnetic assembly is not constrained. Table 5-4 shows the optimized designs for this case. The parameters that are at the upper or lower bound are indicated in bold. It was seen that as the maximum power consumption in the coil was reduced, the optimal design resulted in a magnetic assembly that had the largest allowable magnet (r_m and h_m). The length and the height of the gap (l_g and h_g) reduced with reduced power consumption. Thus for lower power consumption, the optimal design had a smaller coil. However, when the maximum allowable power was set to very small value (< 0.15 W), the resulting optimal design was different from these trends. It can be seen from Table 5-4 that for very low power constraints (0.08 W, 0.1 W,

0.15 W) the optimal design required the smallest possible gap dimensions (l_g and h_g).

Consequently small wire cross-section is necessary in order to fit sufficient coil in the gap.

The relationship between the maximum achievable blocked force and maximum allowable power can be deduced from the slope of the line in the log-log scale as follows

$$F_b \propto P^{\frac{1}{3}}. \quad (5.143)$$

The details of the optimized designs with mass constraints are included in Appendix C.

Table 5-4. Optimized designs for maximum blocked force for various power constraints and no mass constraint (active constraints indicated in bold)

r_m (mm)	h_m (mm)	h_g (mm)	l_g (mm)	<i>AWG</i>	P (W)	F_b (N)	<i>Mass</i> (g)
4.7	12.7	1.6	1	40	0.05	0.095	52
6	12.7	1.6	1	40	0.1	0.15	65
9.2	12.7	1.6	1	40	0.15	0.36	105
9.4	12.7	1.6	1	34	0.2	0.48	108
9.4	12.7	1.6	1.2	34	0.3	0.65	110
9.4	12.7	1.6	1.6	34	0.5	0.9	113
9.4	12.7	2	1.9	34	0.8	1.18	117
9.4	12.7	2.2	2.1	34	1	1.33	120
9.4	12.7	2.7	2.4	34	1.5	1.66	125
9.4	12.7	3.2	2.6	34	2	1.93	130
9.4	12.7	4.5	3.4	34	4	2.74	144
9.4	12.7	5.4	3.9	34	6	3.34	156
9.4	12.7	6.3	4.4	34	8	3.83	165
9.4	12.7	7	4.7	34	10	4.24	174
9.4	12.7	7.6	5.1	34	12	4.62	181
9.4	12.7	8.5	5.5	34	15	5.1	192
9.4	12.7	9.3	5.9	34	18	5.54	202
9.4	12.7	9.6	6.3	34	21	5.85	209

When mass constraints were included in addition to the power constraints, maximum achievable blocked force was reduced. Figure 5-7 shows the maximum achievable blocked force for various power constraints and three different mass constraints. Two distinct regions can be observed in the optimal designs. When the maximum allowable power is small, the optimal blocked force is limited by the geometry parameters of the actuator. This can be considered the “geometry limited” regime of the actuators. Similarly, the flatter regions in plot are “mass

limited”. As the maximum allowable mass is increased, the mass limited region becomes smaller. For extremely small maximum allowable power (few cases shown here 0.08 W, 0.1 W, 0.15 W), the optimal design is limited only by the input maximum power allowed.

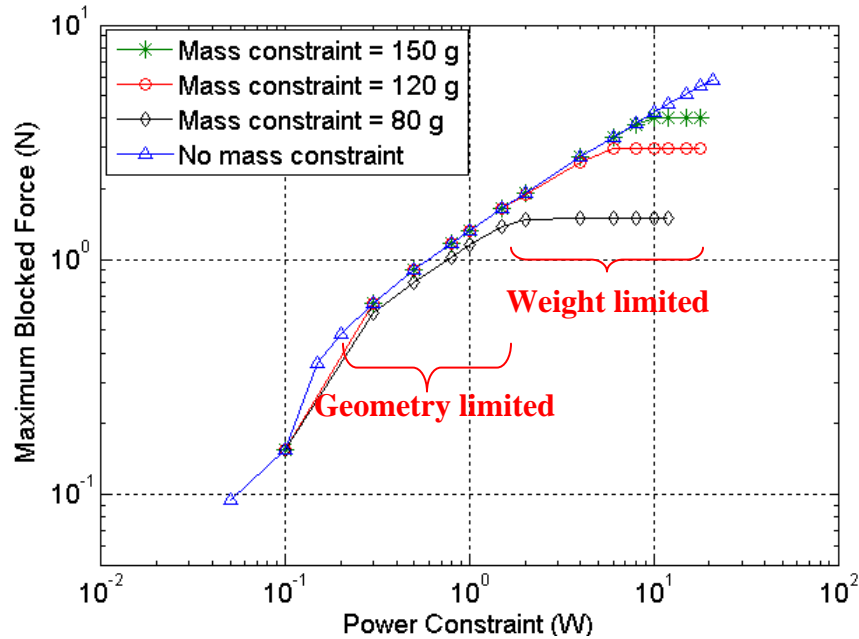


Figure 5-7. Optimization results for maximizing blocked force for various power and mass constraints

The optimal designs of the magnetic assembly in order to achieve maximum blocked force indicate that for a given power and mass constraint, the largest magnet should be chosen. The geometry, power and mass constraints have a very large impact on the maximum blocked force. Depending on which of the two constraints is more restrictive, the device may be in a “geometry limited” or “mass limited” regime as indicated before. Note that in each of these regions, the power constraint is also active. However, for extremely small power constraints, the optimal design performance is limited only by the power as indicated.

5.3.2 Composite Diaphragm Design Tradeoffs

The magnetic assembly and the coil configuration determine the blocked force achievable by the ZNMF actuator. In contrast, the composite diaphragm largely controls the dynamics of the

actuator. For compact actuators, where the cavity is small, the Helmholtz frequency of the cavity and the slot/orifice is much higher than the diaphragm resonant frequency. Thus the overall actuator resonant frequency is determined primarily by the diaphragm resonance. The acoustic model for this composite diaphragm was introduced in section 3.4.2 and all the detailed derivations are included in Appendix B. This section will study the variation of diaphragm lumped parameters as a function of the geometry of the diaphragm.

5.3.2.1 Effective area (S)

The concept of effective area was first introduced in section 3.4.2. The effective area of the PDMS diaphragm can be calculated by equating the total volume it displaces to that displaced by a rigid piston. This effective area is used to calculate the electroacoustic gyrator ratio G . Thus the diaphragm effective area is determined by calculating the total change in volume $|\Delta V|$ and dividing it by the center displacement $w(0)$. Thus the effective area is

$$S = \frac{|\Delta V|}{w(0)} \quad (5.144)$$

As the central boss is assumed to be rigid, the effective area is given by

$$S = \frac{\pi \left[a^6 - 3b^2a^4 + 3a^2b^4 - b^6 \right]}{3a^4 + 12a^2b^2 \ln\left(\frac{b}{a}\right) - 3b^4} = \frac{\frac{\pi a^2}{3} \left[1 - 3\left(\frac{b}{a}\right)^2 + 3\left(\frac{b}{a}\right)^4 - \left(\frac{b}{a}\right)^6 \right]}{\left(1 + 4\left(\frac{b}{a}\right)^2 \ln\left(\frac{b}{a}\right) - \left(\frac{b}{a}\right)^4 \right)}. \quad (5.145)$$

Note that when $b/a \rightarrow 0$, the effective area is 1/3 of the physical area of the diaphragm. When $b/a \rightarrow 1$, the effective area approaches the physical area of the diaphragm, since the diaphragm is assumed to be rigid. The variation of the effective area of the diaphragm is shown in Figure 5-8. The effective area is normalized by the physical area of the diaphragm (πa^2). It can be seen that the effective area of the diaphragm increases monotonically as a function of the solidity ratio. The two limiting cases ($b/a = 0$ and $b/a = 1$) can also be seen clearly in the figure.

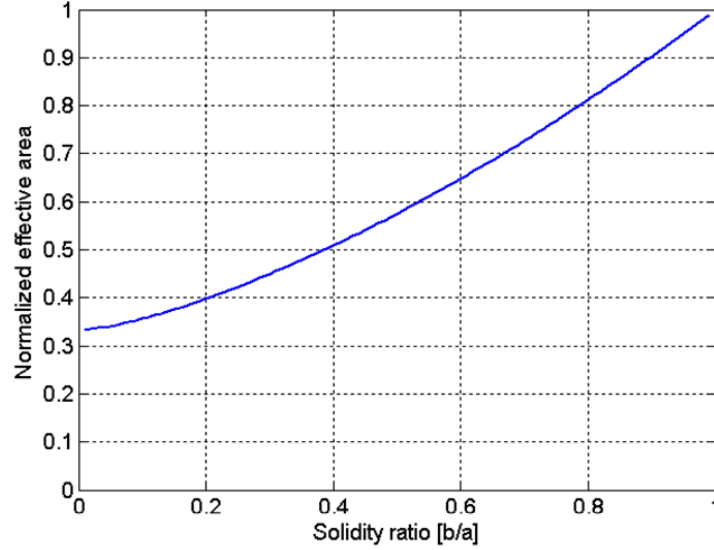


Figure 5-8. Normalized effective area as a function of the solidity ratio

5.3.2.2 Acoustic compliance (C_{aD})

The acoustic compliance of the diaphragm is defined as the volume displaced by the diaphragm under unit pressure loading, when the electrical excitation is zero. The expression for the acoustic compliance of the composite diaphragm was presented in section 3.4.2 and is repeated here

$$C_{aD} = \frac{\pi(1-\nu_2^2)}{16E_2h^3} [-a^6 + 3b^2a^4 - 3a^2b^4 - b^6] = \underbrace{\frac{\pi(1-\nu_2^2)a^6}{16E_2h^3}}_{C_{aD0}} \left[1 - 3\left(\frac{b}{a}\right)^2 + 3\left(\frac{b}{a}\right)^4 - \left(\frac{b}{a}\right)^6 \right]. \quad (5.146)$$

The acoustic compliance is only a function of the solidity ratio b/a , the diaphragm thickness and the material properties of the annular region for a rigid central region. The compliance of the diaphragm is the largest when the solidity ratio is zero (C_{aD0} i.e., when there is no inner circular boss and the diaphragm is homogenous, $b=0$). As the solidity ratio increases, the diaphragm becomes stiffer, and the compliance reduces. For the case when the solidity ratio is 1, ($b=a$), the acoustic compliance is zero, because the central boss is assumed to be rigid and the boundary condition at $r=a$ specifies zero displacement.

Figure 5-9 shows the variation of the normalized acoustic compliance as a function of the solidity ratio. The compliance is normalized by the corresponding maximum compliance at a solidity ratio of 0 (C_{aD0}). Note that this normalization produces a single curve that is solely a function of b/a . The plot indicates that the compliance becomes smaller as the solidity ratio increases in accordance with (5.146). The values of typical geometrical parameters and material properties are provided in Table 5-5.

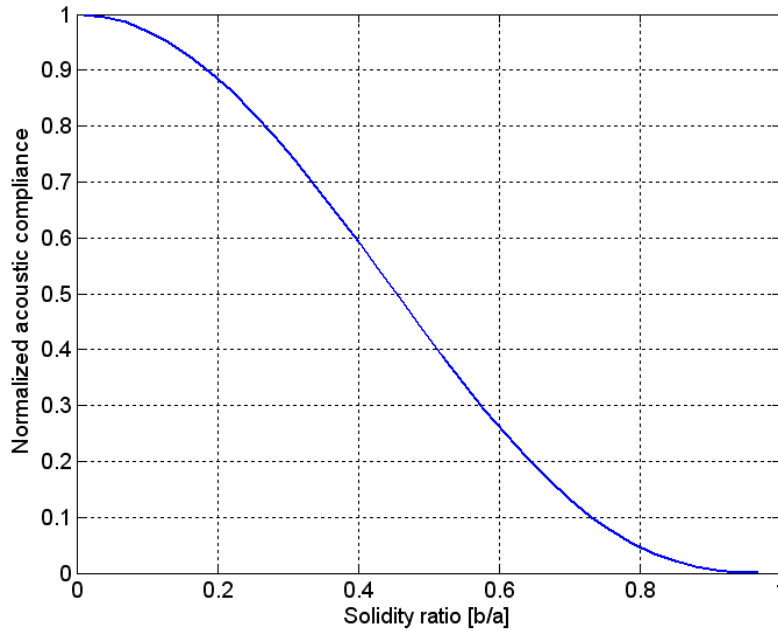


Figure 5-9. Acoustic compliance variation with the solidity ratio ($h/a = 0.08$)

It was seen from (5.125) that the low frequency performance of the electrodynamic ZNMF actuator depends on the ratio C_{aD}/S . This ratio can be derived from (5.145) and (5.146) and is given by

$$\frac{C_{aD}}{S} = \frac{3(1-\nu_2^2)a^4}{16E_2h^3} \left(1 + 4\left(\frac{b}{a}\right)^2 \ln\left(\frac{b}{a}\right) - \left(\frac{b}{a}\right)^4 \right). \quad (5.147)$$

It was discussed before that in order to maximize the low frequency output volume velocity of the ZNMF actuator, the ratio C_{aD}/S needs to be maximized. It can be seen from

(5.147) that this can be achieved by choosing a diaphragm with large radius (a). However, it can also be seen that the ratio C_{ad}/S reduces monotonically as the solidity ratio b/a increases. Thus the smallest possible solidity ratio should be chosen. However, it will be shown further in this section that the resonant frequency and hence the bandwidth of the ZNMF actuator increases with the solidity ratio. Thus there is inherent tradeoff between the low frequency performance of the ZNMF actuator and its bandwidth.

Table 5-5. Diaphragm material properties and geometry

Parameter	Value
Outer radius a	12.7 mm
Inner radius b	Variable
Thickness h	Variable
Young's modulus of the annular portion E_2	360 kPa
Poisson's ratio of the annular portion ν_2	0.33
Density of the annular portion ρ_2	970 kg/m ³
Young's modulus of the central portion E_1	20 GPa
Poisson's ratio of the central portion ν_1	0.33
Density of the central portion ρ_1	1190 kg/m ³
Mass of the coil M_{coil}	0.31 g

5.3.2.3 Acoustic mass (M_{ad})

The effective mass of the diaphragm is calculated by computing the total kinetic energy of the diaphragm and lumping it to that of an equivalent mass moving with the center velocity, $\dot{w}(0) = j\omega w(0)$ as discussed in section 3.4.2. The attached coil also contributes to the total mass of the diaphragm assembly. The overall acoustic mass of the diaphragm is given by

$$M_{ad} = \frac{M_{rigid}}{S^2} + 2\pi\rho_2 h \int_b^a \left(\frac{w(r)}{\nabla} \right)^2 r dr + \frac{M_{coil}}{S^2} \quad (5.148)$$

where M_{rigid} and M_{coil} are the mass of the rigid central boss and the mass of the coil respectively.

Figure 5-10 shows the normalized acoustic mass of the diaphragm for various solidity ratios. The total acoustic mass is normalized by the corresponding value of the total acoustic

mass with $b/a = 0$. Again, this normalization procedure collapses the parametric dependence on b/a to a single curve. As b/a increases, the effective mass of the diaphragm decreases.

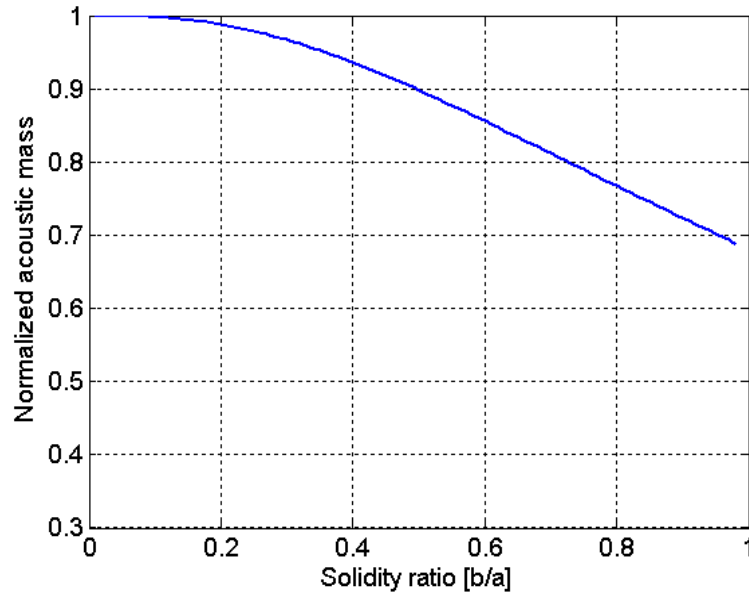


Figure 5-10. Acoustic mass variation with the solidity ratio ($h/a = 0.08$)

5.3.2.4 Resonant frequency (f_{res})

The resonant frequency of the diaphragm can be calculated once the diaphragm's total acoustic mass and acoustic compliance are known. The resonant frequency is given by

$$f_{res} = \frac{1}{2\pi\sqrt{M_{aD}C_{aD}}} \quad (5.149)$$

Figure 5-11 shows the variation of the resonant frequency with b/a . The diaphragm geometry and material properties used are indicated in Table 5-5. The thickness of the diaphragm is fixed at 1 mm. It can be seen that the resonant frequency increases rapidly as the solidity ratio becomes larger. This is due to the fact that both the acoustic compliance and the total acoustic mass reduce with the solidity ratio. The comparison with finite element results is also shown on the same plot. Note that at solidity ratio of 1, the resonant frequency is infinite as the compliance is zero for the solidity ratio of 1.

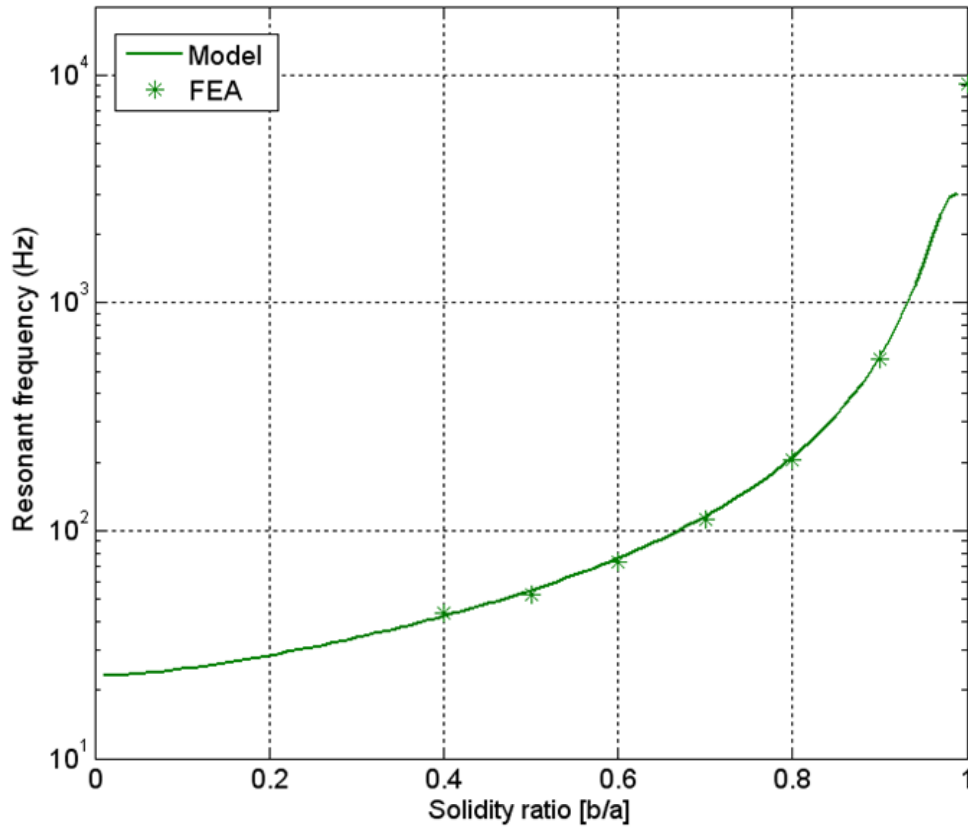


Figure 5-11. Resonant frequency of the diaphragm ($h/a = 0.08$)

5.3.3 System-level Design Tradeoffs

The two previous sections discussed the design tradeoffs involved in two major components – magnetic assembly and composite diaphragm – of the electrodynamic ZNMF actuator. The system-level design tradeoffs are discussed in this section. The electroacoustic transduction coefficient G is one of the key parameters of the actuator. The transduction coefficient G is defined as

$$G = \frac{BL_{coil}}{S} . \quad (5.150)$$

Thus, for a given magnetic assembly and coil configuration if BL_{coil} is assumed to be constant, the transduction coefficient is only a function of the diaphragm effective area S . From (5.145) it can be seen that the effective area is a function of the solidity ratio. Figure 5-12 shows

the variation of the normalized transduction coefficient as a function of the solidity ratio. The transduction coefficient in each case is normalized by the maximum transduction coefficient (at solidity ratio 0). As the solidity ratio increases, the effective area becomes larger. As the solidity ratio approaches 1, the annular compliant region of the diaphragm becomes smaller, and the effective area approaches the physical area of the diaphragm. Hence the normalized transduction coefficient approaches 1/3. It should also be noted that the transduction coefficient is independent of the thickness of the diaphragm. Thus in order to achieve large transduction coefficient, smaller solidity ratios are preferred.

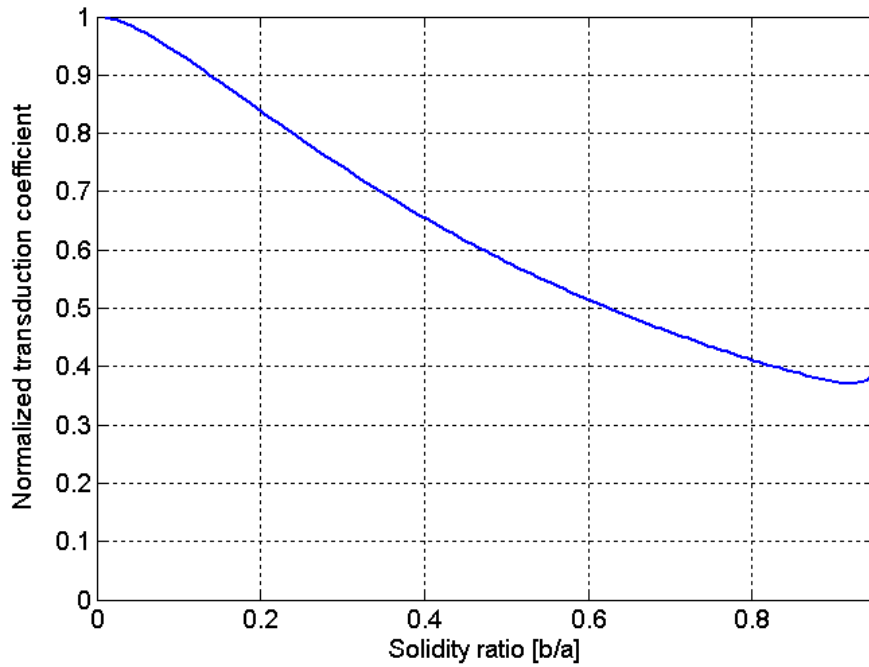


Figure 5-12. Variation of electroacoustic transduction coefficient G with solidity ratio ($h/a = 0.08$)

As indicated by (5.124) - (5.128), in addition to the transduction coefficient, the ratio G/R_{eC} is also an important factor impacting the actuator performance. The ratio is given by

$$\frac{G}{R_{eC}} = \frac{BL_{coil}}{SR_{eC}} = \frac{BL_{coil}A_{wire}}{S\rho_{wire}L_{coil}} = \frac{BA_{wire}}{S\rho_{wire}} \quad (5.151)$$

where A_{wire} is the cross-sectional area of the wire and ρ_{wire} is the resistivity of the coil material in $\Omega\cdot m$. Thus in order to maximize G/R_{eC} , a coil with small resistivity ρ_{wire} and large area A_{wire} should be chosen. The magnetic flux density in the gap B should also be maximized. Thus a “long” magnet (large h_m) with large coercivity H_c should be chosen. Note that a larger magnet will result in a heavier actuator. Thus there is a tradeoff between device performance and weight of the device.

The resonant frequency of the actuator is determined primarily by the resonant frequency of the diaphragm assembly, because the cavity is designed to have a small volume. The resonant frequency of the diaphragm increases rapidly with the solidity ratio as can be seen from Figure 5-11. Thus high resonant frequency and high bandwidth require larger solidity ratio. However, as discussed before, a large volume velocity requires a small solidity ratio. Thus there is a tradeoff involved between large output volume velocity and high bandwidth. The tradeoff between the output volume velocity and the bandwidth can be studied by investigating the overall performance of the ZNMF actuator for various solidity ratios.

Figure 5-13 shows the predicted output velocity as a function of the frequency for four different solidity ratios ($b/a = 0.5 - 0.8$). The magnetic assembly parameters are detailed in Table 5-6 and the diaphragm geometry and material properties are indicated in Table 5-5. The diaphragm damping ratio is assumed to be constant at 0.15. As the solidity ratio increases, the diaphragm becomes stiffer, thus increasing the resonant frequency and lowering the output velocity. Thus there is an inherent tradeoff between maximum velocity and bandwidth. It can be seen that the $v_{max} f_{res}$ (v_{max} is the maximum rms velocity) product increases slightly with the solidity ratio, as the resonant frequency increases faster than the drop in the maximum output velocity.

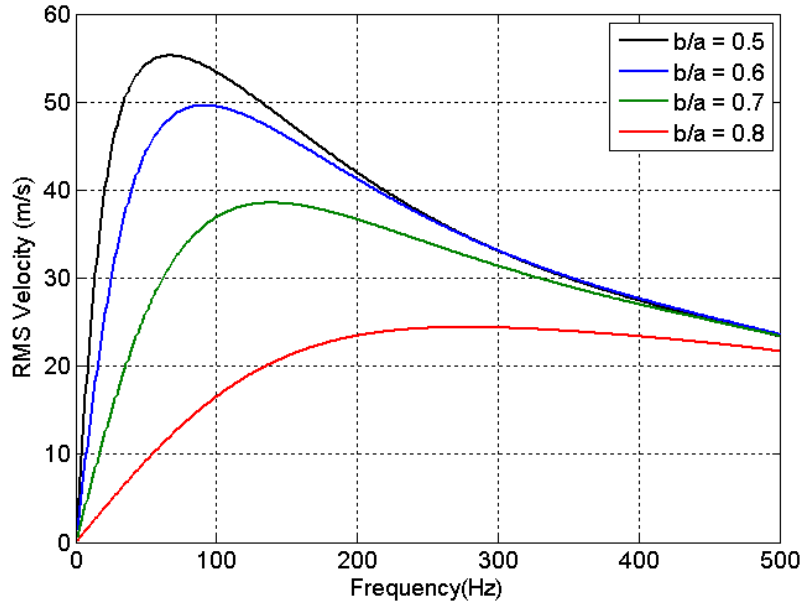


Figure 5-13. Variation of predicted output velocity with solidity ratio ($h/a = 0.08$)

Table 5-6. Parameters for the magnetic assembly

Parameter	Value
Magnet radius r_m (mm)	4.7
Magnet height h_m (mm)	6.35
Height of the air gap h_g (mm)	3.2
Width of the annular position w_c (mm)	3.2
Height of the bottom h_b (mm)	3.2
Length of the gap l_g (mm)	2.8
Total radius r_t (mm)	10
Remnant magnetic flux density B_r (T)	1.3
Relative permeability of the magnet μ_{magnet}	1.05
Predicted magnetic flux density in the gap B (T)	0.4

5.3.4 Power Considerations

The input and output power of the actuator can also be calculated using the lumped element model. Both input and output powers are a function of the frequency of operation. The input power is the total power dissipated and is defined from the lumped-model as

$$P_{in} = |Q_D|^2 \left(\frac{G^2}{R_{eC}} + R_{aP} + R_{aO} + R_{aos} \right). \quad (5.152)$$

Similarly the output power is defined as the power lost as the dump losses or the power delivered to the non-linear resistance R_{aO}

$$P_{out} = |Q_{out}|^2 (R_{aO}) \quad (5.153)$$

where both Q_D and Q_{out} are defined in section 3.6.

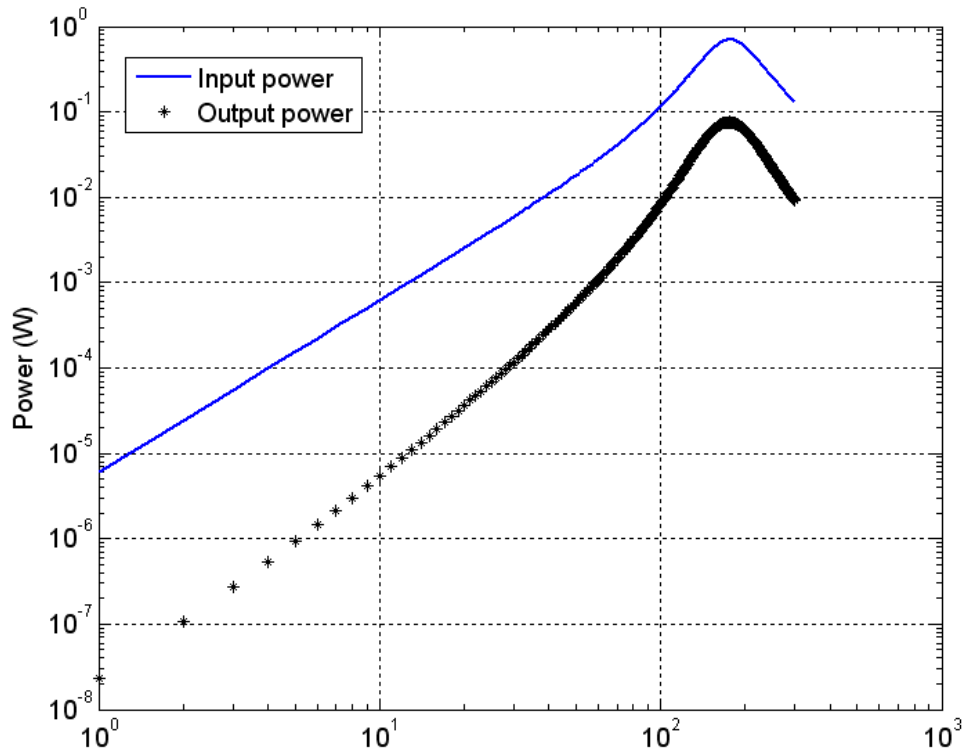


Figure 5-14. Input and output as a function of frequency for actuator A2

Figure 5-14 shows both the input and output power as a function of frequency of operation for actuator A2 discussed in Chapter 4. It can be seen that the maximum of both the input and output power occur at the resonant frequency. It can be seen that the maximum efficiency of the actuator, defined as the ratio of output power to the input power, is also a function of the frequency as seen in Figure 5-15. The maximum efficiency occurs at the resonance of the actuator.

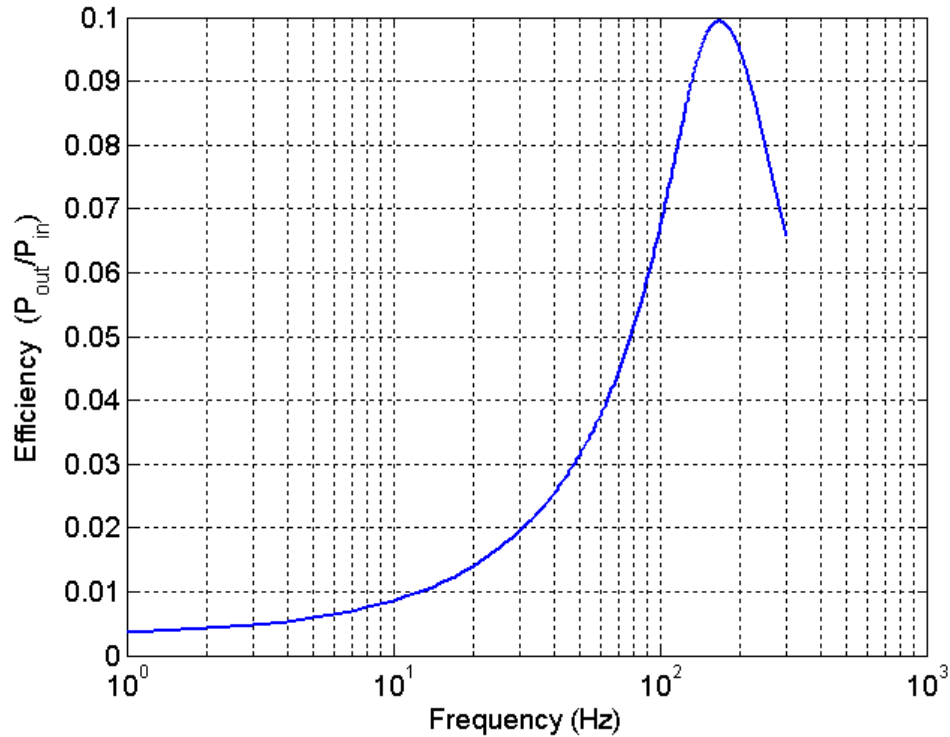


Figure 5-15. Efficiency of actuator A2

5.4 Optimization of Composite Diaphragm Electrodynamic ZNMF Actuators

This section details the coupled optimization problem that optimizes the overall ZNMF actuator including the magnetic assembly and the diaphragm. First various constraints for various components are discussed. Based on the given application, it may be desired to establish the synthetic jet through an axisymmetric orifice or a 2D slot. In Chapter 5, the optimization of an actuator with a 2D-slot is considered. The optimization routine uses the entire lumped model of the ZNMF actuator including the cavity compliance, although it was shown that the effect of the including the cavity compliance is extremely small.

The schematic of the electrodynamic ZNMF actuator with all the important dimensions is shown in Figure 4-13. The design variables chosen for the optimization problem are all the dimensions of the magnetic assembly, dimensions of the diaphragm, the cavity length and the gauge of the coil used. All the design variables are listed below

- Magnet Radius (r_m)
- Magnet Height (h_m)
- Height of the gap (h_g)
- Length of the gap (l_g)
- Diaphragm outer radius (a)
- Diaphragm inner radius (b)
- Diaphragm height (h)
- Height of the cavity (h_C)
- AWG (gauge of the coil wire)

The design vector is thus mathematically represented as

$$\vec{X} = \{r_m, h_m, h_g, l_g, a, b, h, h_C, AWG\} \quad (5.154)$$

The constraints considered are the same as those chosen for the optimization of the magnetic assembly except the power constraint. The constraints are listed below

- Upper bounds on all geometrical dimensions to limit the size of the device to 30 mm diameter, 30 mm tall cylinder. Note that these size constraints were chosen for a fair comparison with the previously investigated unoptimized prototype devices. (In general, the maximum size usually will depend entirely on the target application. The size used here is suitable for typical automotive flow control application.)
- Lower bounds on all geometrical dimensions to ensure that manufacturing limits are not violated.
- The length of the gap is constrained to be 50 % of the magnet height to ensure that the 1-D circuit model is valid.
- The maximum diaphragm deflection is restricted to be 30 % of the diaphragm thickness.
- The total input power given by (5.152) is constrained.
- The overall mass of the magnetic assembly is also constrained.

The upper and lower bounds for the magnetic assembly, diaphragm and the cavity are indicated in Table 5-7.

The mechanical damping of the diaphragm structure is not known beforehand and is usually extracted experimentally. The change in the damping ratio will affect the performance of the actuator and affect the optimal design. It was shown in Chapter 4 that the diaphragm damping is the smallest contribution to the overall damping in the actuator. The equivalent

electrical damping and the fluidic damping in the slot/orifice dominate the total damping in the actuator. However it is important to study the impact of change in mechanical damping on the actuator performance. Figure 5-16 shows the frequency response of actuator A1 for several different damping ratios (0.01-0.2).

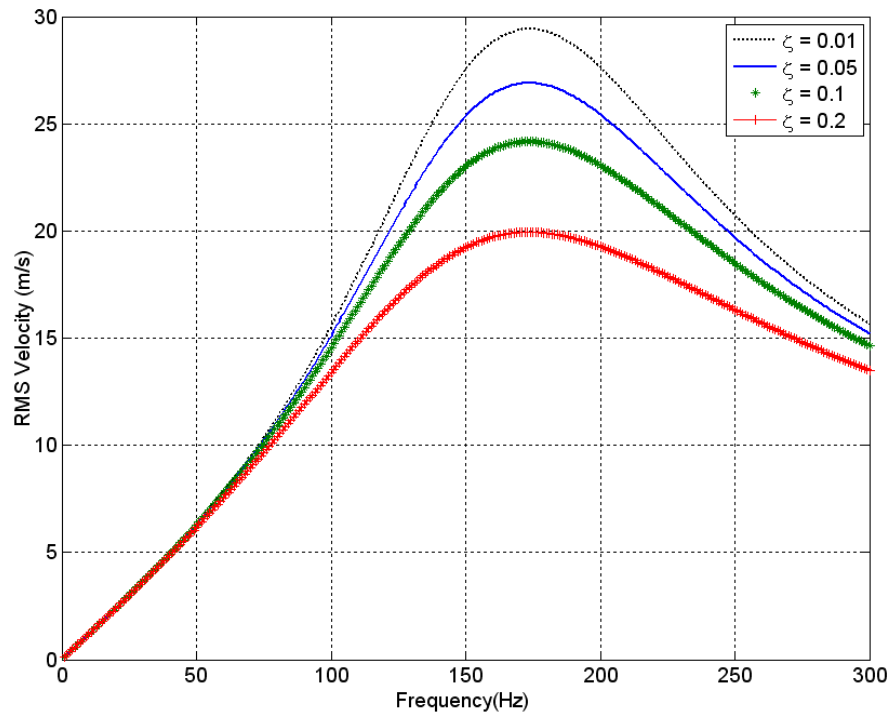


Figure 5-16. Frequency response of actuator A1 for different diaphragm damping

Table 5-7. Lower and upper bounds on design variables

Design variable	Lower bound (L)	Upper bound (U)
Magnet radius (r_m) (mm)	0.47	9.4
Magnet height (h_m) (mm)	0.635	12.7
Height of the gap (h_g) (mm)	1.6	9.6
Length of the gap (l_g) (mm)	1	8.5
AWG (gauge of the coil wire)	34	40
Diaphragm outer radius (a) (mm)	10	15
Diaphragm inner radius (b) (mm)	0.1	a
Height of the diaphragm (h) (mm)	1	3
Height of the cavity (h_c) (mm)	1	3

It can be seen that as the damping ratio increases, the frequency response of the device is “flatter”. However, even if the damping ratio increases by a factor of 20, the maximum output

velocity reduces only by about 30 %. For all the prototype actuators characterized in Chapter 4, the diaphragm damping was measured to be between 0.015 and 0.07. Thus as a conservative estimate, the diaphragm damping ratio is assumed to be 0.1 for optimization setup.

5.4.1 Choice of the Objective Function

The choice of objective function in the case of electrodynamic ZNMF actuators depend on the application based on the type of fluidic impact these actuators need to produce on the flow field. Gallas et. al [58] used the total velocity over a predefined range of frequencies as the objective function, which can be stated mathematically as

$$\text{Minimize: } f_{obj1}(\vec{X}) = - \int_0^{f_{lim}} v_{rms}(f) df . \quad (5.155)$$

Here v_{rms} is the rms centerline velocity. The frequency range chosen for this work was 0 – 300 Hz as indicated. However, several other objective functions may be used, and the resulting design may be significantly different in each case. A “gain-bandwidth” type objective function stated mathematically as

$$\text{Minimize: } f_{obj2}(\vec{X}) = -v_{max} f_{res} \quad (5.156)$$

was also investigated. Here v_{max} is the maximum rms centerline velocity, and f_{res} is the resonant frequency of the actuator. A third objective function investigated here was simply maximizing the rms centerline velocity at any given frequency. This is stated mathematically as follows

$$\text{Minimize: } f_{obj3}(\vec{X}) = -v_{max} . \quad (5.157)$$

The baseline actuator considered for the optimization is the actuator A2 described in Chapter 4. This baseline actuator was optimized with the two objective functions described above. The power and mass was not constrained in both the cases. Figure 5-17 shows the output velocity for the baseline actuator and the three optimized actuators. The first objective function (integrated frequency over a range of frequencies) shows nearly 50 % improvement in the peak

velocity as compared to the baseline device. However, the resonant frequency of the optimized device is lower (~ 85 Hz). The performance of the optimized device is slightly worse than that of the baseline device above 150 Hz. It can be seen that when the second objective function is used, the resonant frequency of the actuator is pushed very high while there is no significant improvement in the peak velocity obtained and the low frequency performance of the actuator is also poor. The use of the third objective function (maximum velocity), results in an actuator with very high peak velocity (nearly twice the baseline actuator case). However, the actuator has a very low resonant frequency. Similar trends are observed for all three objective functions when the geometry constraints are changed and/or power and mass constraints are included.

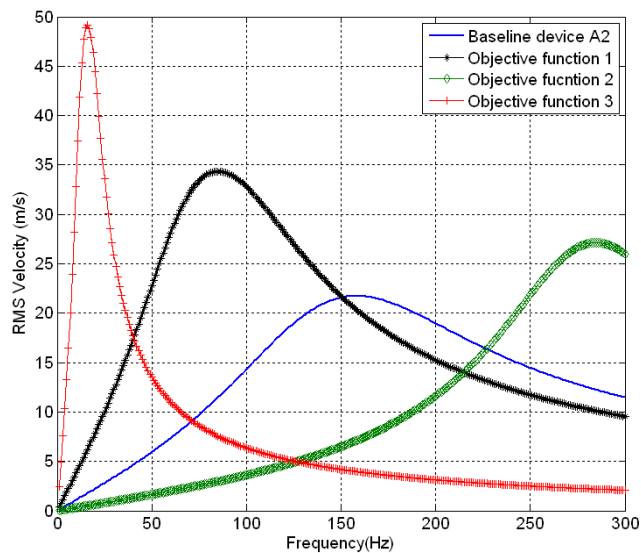


Figure 5-17. Comparison of the frequency response of the baseline device and optimized designs for the three objective functions

The optimized designs and some key performance parameters for each of the objective functions are tabulated in Table 5-8. It can be seen that each optimal design uses the maximum diaphragm radius, maximum wire size (smallest AWG), largest cavity height and smallest diaphragm thickness. Moreover, for objective function 3 (maximum $v_{\max} f_{res}$), the diaphragm inner radius is the largest, making a very stiff device. Conversely for objective function 2

(maximum v_{\max}), the optimal design has the smallest inner diaphragm radius resulting in a very compliant device. Thus the resonant frequency in this is the smallest (~ 20 Hz)

Table 5-8. Baseline actuator and optimized designs for objective functions 1-3 (active constraints indicated in bold)

<i>Case</i>	r_m (mm)	h_m (mm)	h_g (mm)	l_g (mm)	a (mm)	b (mm)	L_C (mm)	AWG	h (mm)	<i>Power</i> (W)	<i>Mass</i> (g)
Baseline actuator	4.77	9.5	3.2	2.4	12.7	9.5	3	34	1	0.8	57
Objective function 1	5.6	12.7	7.2	2.1	12.7	8	3	34	1	1.3	88
Objective function 2	3.6	12.7	9.6	4.1	12.7	1.4	3	34	1	2.716	86
Objective function 3	44.1	8.8	5.6	3.5	12.7	10.8	3	34	1	0.536	64

Table 5-9. Optimized designs for objective function 1 (maximum integrated velocity) for various power constraints (active constraints indicated in bold)

r_m (mm)	h_m (mm)	h_g (mm)	l_g (mm)	a (mm)	b (mm)	L_C (mm)	AWG	h (mm)
5.6	12.7	7.2	2.1	12.7	8	3	34	1
5.6	12.7	6.6	2.1	12.7	8.1	3	34	1
5.7	12.7	5.5	2	12.7	8.3	3	34	1
5.8	12.7	4.4	1.9	12.7	8.3	3	34	1
6.3	10.6	4.9	1.4	12.7	8	3	34	1
5.3	8.8	2	2	12.7	7.7	3	34	1
5.4	11.9	2.9	1.1	12.7	7.3	3	36	1

For this work, objective function 1 (integrated velocity over 0 – 300 Hz) is used. The slot height, width and length are usually specified for a given application and are held constant here. The constraints – upper and lower bounds set by manufacturing limits, overall size specifications and power and mass limits – have already been described. If the maximum input power to the device defined by (5.152) is now constrained, the resulting optimized devices are different. Figure 5-18 shows the variation of the peak centerline velocity as a function of the maximum allowable input power. The peak centerline velocity reduces (almost linearly) as the maximum input power is lowered, as expected. Similar behavior is also observed when the mass of the actuator is constrained. The optimized designs for the various power constraints are tabulated in

Table 5-9. The active constraints are indicated in bold. The other performance parameters of the optimized actuators are detailed in Appendix C.

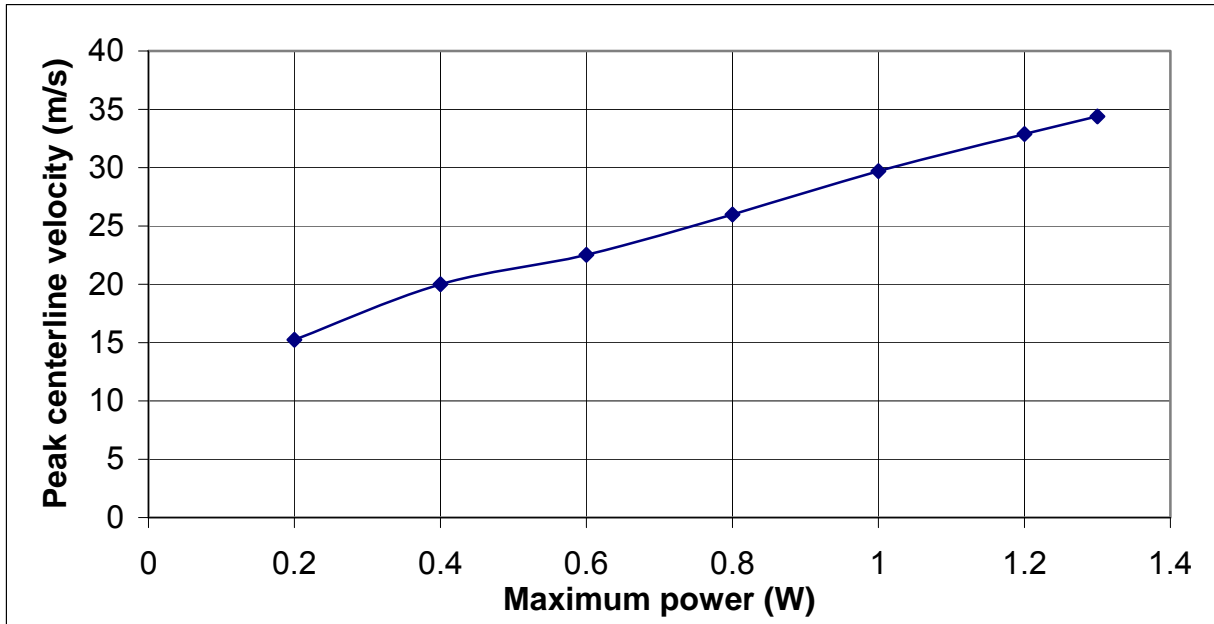


Figure 5-18. Maximum output velocity as a function of maximum allowable input power for objective function 1

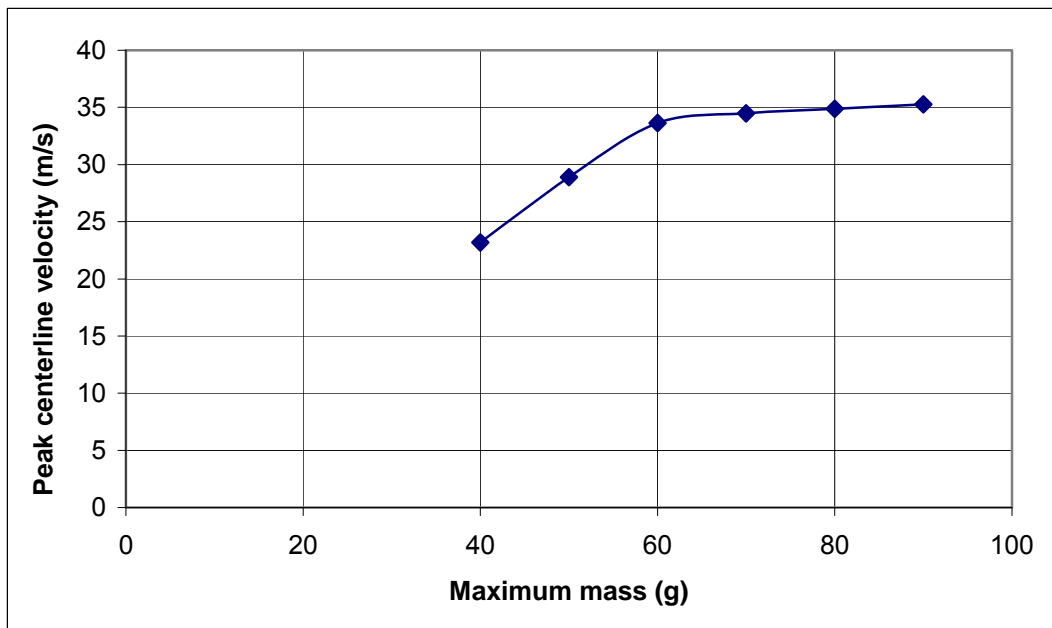


Figure 5-19. Maximum output velocity as a function of maximum allowable input mass for objective function 1

When the maximum mass of the actuator was constrained, (without any power constraint) the maximum output velocity is initially “mass limited,” as seen from the linearly increasing region of the curve in Figure 5-19. As the maximum allowable mass is increased, the maximum output velocity obtained from the actuator starts tapering off as the actuator performance is now limited by the geometry constraints.

It was seen that for the objective function 1, for any power constraint, the resulting optimized actuator had a lower resonant frequency than the baseline actuator. This can be seen from Figure 5-17 that the resonant frequency of the baseline actuator was close to 150 Hz and that of the optimized device was about 80 Hz. In most cases, it is desired that the actuator have a certain resonant frequency and bandwidth. Thus optimization was performed again by including an resonant frequency inequality constraint ($f_r \geq 120\text{Hz}$). The frequency response of the optimized device without power and mass constraints but including a resonant frequency constraint was shown in Figure 5-20. It can be seen including the resonant frequency resulted in an actuator that has better performance over all frequencies as compared to the baseline actuator. The low frequency performance is slightly lower than the case where the resonant frequency was not included. It was seen that the using objective function 3 (maximum velocity) pegged the resonant frequency to 120 Hz and maximum velocity obtained was lower than the previous case. It was seen that the resonant frequency constraint did not impact the optimized design for objective function 2 (maximum $v_{\max} f_r$).

For this work the optimized actuator for objective function 2 with a resonant frequency constraint is fabricated. The optimized design and the key performance parameters are shown in Table 5-10. The corresponding parameters for the baseline actuator are also shown. The active

constraints are indicated in bold. The value of the objective function for the optimized device was 5640 m/s^2 . This can be converted to an average velocity of 18.8 m/s .

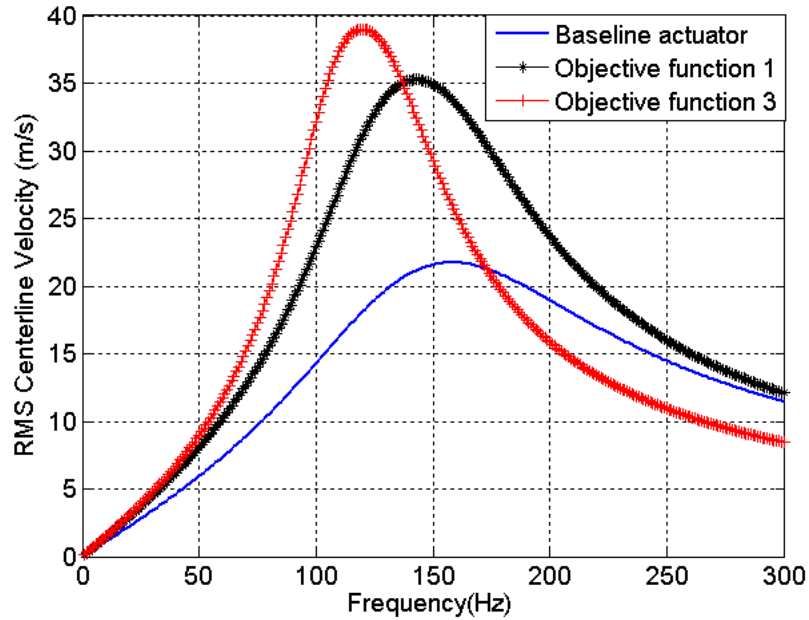


Figure 5-20. Comparison of the frequency response of the baseline device and optimized designs for the objective functions with a resonant frequency constraint

Table 5-10. Optimized and baseline actuator parameters fabricated for this work

Design Variables	Baseline Actuator	Optimized Actuator
Magnet radius (r_m) (mm)	4.7	5.5
Magnet height (h_m) (mm)	9.5	12.7
Gap height (h_g) (mm)	3.2	8.1
Gap length (l_g) (mm)	2.8	2.2
Diaphragm outer radius (a) (mm)	12.7	12.7
Diaphragm inner radius (b) (mm)	9.3	9.5
Cavity height (L_C) (mm)	3	3
Diaphragm height (h) (mm)	1	1
Coil size (AWG)	34	34
Other Parameters		
Number of coil layers	3	4
Number of turns per layer	30	30
Mass of the device (g)	80	95
Maximum input power (mW)	700	900
Predicted resonant frequency (Hz)	147	143
Predicted peak velocity (m/s)	21	35.2

5.4.2 Parameter Variation

One important consideration before fabricating the optimized device is the study the sensitivity of the optimized actuator performance to the various design variables. The linearized sensitivity of each of the design variables about the optimized point can be obtained from the optimization routine. This sensitivity is essentially the slope of the objective function vs. the design variable curve at the optimal point. It can be seen that the optimal design is most sensitive to the diaphragm outer radius a . The sensitivity of the objective function to the gap height (h_g) and the cavity height (L_C) is very small. However, the optimization problem is nonlinear and the linearized sensitivity cannot be extrapolated to predict the objective function for large variation in the design variables.

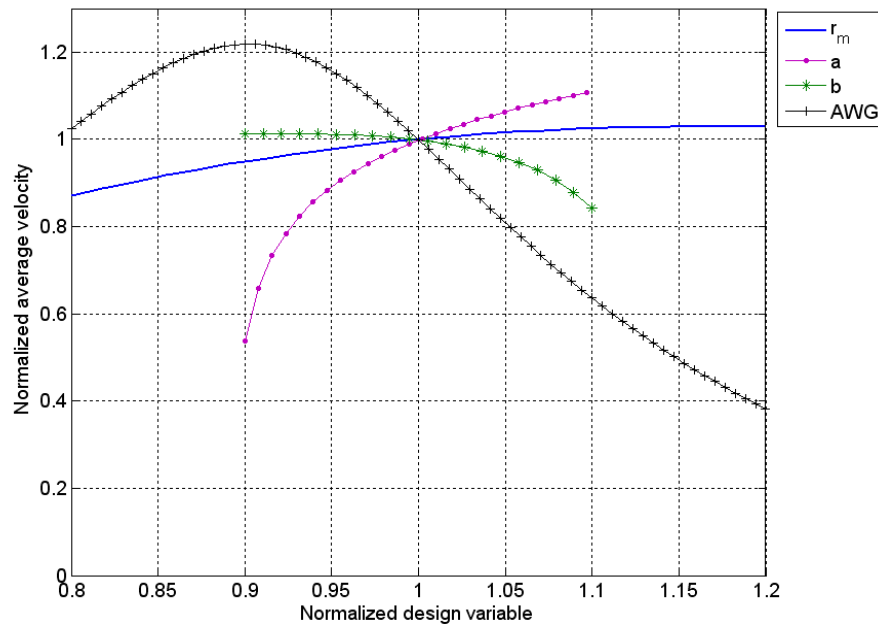


Figure 5-21. Variation of the average velocity from 0 – 300 Hz with the change in the design variables

Figure 5-21 shows the variation of the normalized average velocity generated by the actuators as the design variables are varied individually. Only four design variables are shown

here (magnet radius, diaphragm outer radius, inner radius and wire gauge). The variation in the objective function when the other design variables are changed is relatively small as compared to these four variables. It can be seen that as the magnet radius (r_m) is reduced by 20 %, the actuator performance also reduces. However, the increase in the magnet radius (r_m) by 20 % does not produce similar increase in the objective functions. The objective function reduces significantly when the diaphragm radius (a) is reduced. It can also be seen that smaller wire gauge (larger coil diameter) is always desired.

5.5 Characterization of the Optimized Electrodynamic Actuator

The actuator corresponding to the optimized design presented in the previous section (Table 5-10) was fabricated using the techniques described in Chapter 4. This section presents the characterization of the optimized actuator. The fabrication and characterization procedure followed is the same as that described for the prototype actuators described in Chapter 4.

The magnetic flux density for the optimized magnetic assembly predicted by the 1-D magnetic circuit model was 0.24 T. The average magnetic flux density in the gap predicted by finite element analysis was 0.27 T. The radial magnetic flux density in the gap was also measured using a Lakeshore 475 DSP Gaussmeter with a Lakeshore hall probe HMNT-4E04-VR. The average measured magnetic flux density in the air gap (B) was 0.25 T.

The average coil diameter was measured to be 11.8 mm. The total length of the coil was calculated to be 5.1 m. The electrical impedance of the coil from 40 Hz – 2000 Hz was also measured using the Agilent 4249A precision impedance analyzer. The results of the impedance measurements are shown in Figure 5-22. The dc resistance of the coil was measured to be 4.7 Ω . The inductance of the coil was measured to be 0.15 mH. The inductive reactance at 500 Hz (maximum frequency interest), was 0.47 Ω . Thus the coil inductance was ignored.

The damping was measured using the impulse response test as described in section 4.1.1 b. The results for the damping measurements are shown in Figure 5-23. The damping ratio and the resonant frequency were extracted using the log-decrement method described in Chapter 4. The extracted damping ratio and resonant frequency were 0.053 and 154 Hz respectively. The corresponding diaphragm acoustic resistance R_{aD} is $1.26 \times 10^5 \text{ N-s/m}^5$. The model predicted resonant frequency of the diaphragm is 143 Hz.

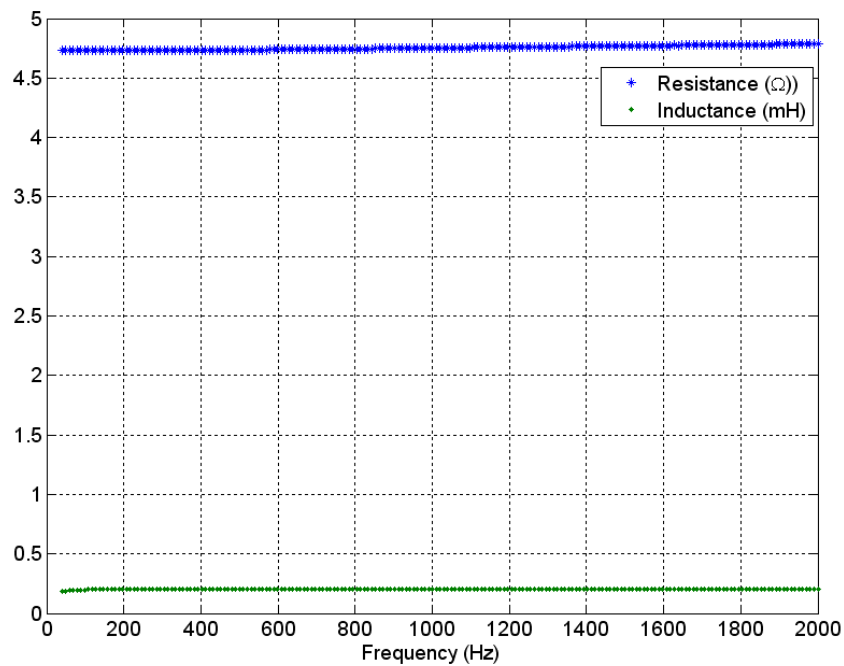


Figure 5-22. Impedance measurement results for the optimized actuator

The output centerline velocity from the actuator was measured using hotwire anemometry. The experimental setup and calibration procedure are detailed in Chapter 4. The hotwire results for the optimized actuator and the corresponding model predictions are shown in Figure 5-24. The baseline actuator results are also shown on the same plot. It can be seen that the maximum velocity from the optimized actuator nearly 50 % more than that from the baseline actuator. Moreover, the optimized actuator generates higher output velocities from 100 Hz – 200 Hz.

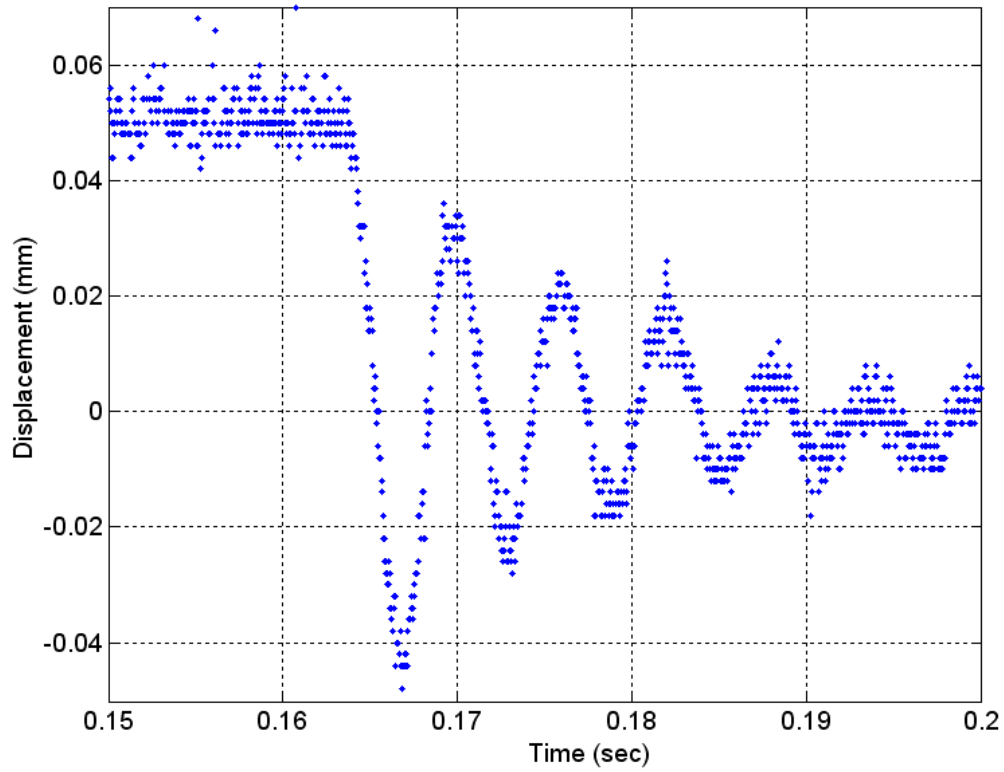


Figure 5-23. Damping measurement results for the optimized actuator

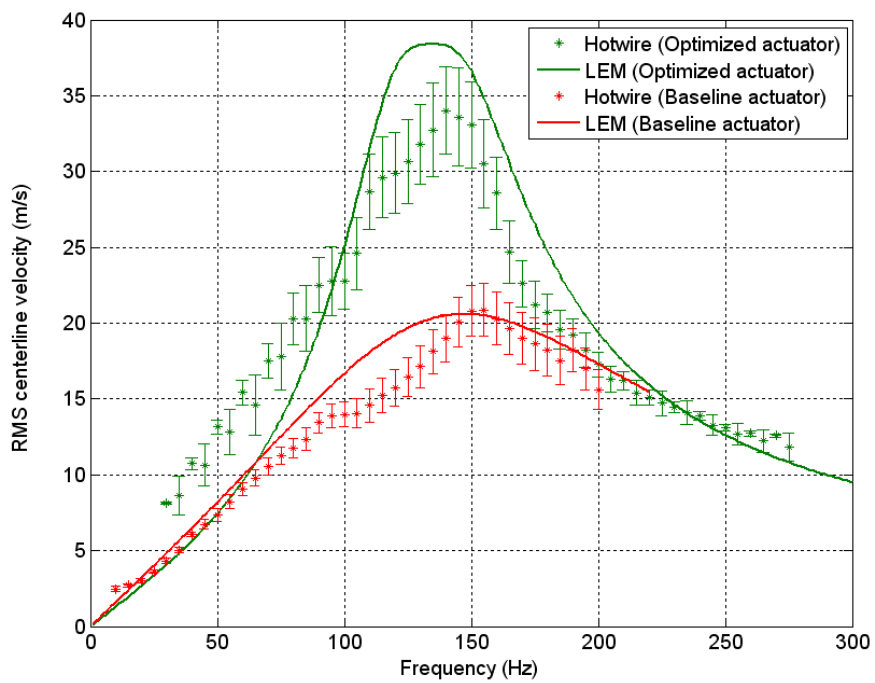


Figure 5-24. Optimized and baseline actuator hotwire and LEM comparisons

Thus it can be seen that the optimization strategies developed in Chapter 5 can be used to achieve better performance from these actuators. Even before trying to optimize the overall actuators, the inherent limitations based on size, power weight constraints can be deduced from the model.

CHAPTER 6 SUMMARY AND FUTURE WORK

The overall research goals of this work and the key contributions are summarized in Chapter 6. Several suggestions for improving and extending this work and possible avenues for further research are also identified.

6.1 Summary

Active flow control is an expanding research area with applications ranging from separation control in automotive and aerospace industry to thermal management and fluidic mixing. One of the most important components of any active flow control scheme is the actuator itself. ZNMF actuators have been used for both open and closed loop flow control schemes. Thus understanding the behavior of the actuators and intelligently designing them forms a significant portion of the flow control efforts. Most ZNMF actuators available in the literature have used piezoelectric transduction schemes. There have been fewer efforts using electrodynamic actuation schemes. However, no systematic modeling and design tools have been reported. Thus this work aimed to present a detailed, first-principles-based, low-order model to predict the performance of electrodynamic ZNMF actuators and provide an effective tool for design and optimization of these actuators.

An axisymmetric magnetic assembly with a central cylindrical magnet was chosen for this work. The magnetic assembly was modeled using the classical 1-D circuit approach to predict the magnetic flux density in the air gap. A circular clamped plate with a central rigid region and an annular region was chosen as the mechanical driver. This mechanical driver was modeled as an annular plate. The overall energetic interactions in the system were modeled using the lumped element modeling approach. Note that the model developed here is specific to the actuator

topology chosen. However, the general modeling approach can be adapted to any actuator configuration.

In order to validate the model, several prototype actuators were built. A unique, flexible hybrid fabrication method was developed to realize these actuators. The magnetic assembly was built using traditional machining techniques. The annular compliant portion of the mechanical driver was manufactured using an elastomer material (PDMS). The elastomer material provided the advantages of very large compliance, ease, flexibility and repeatability in manufacturing.

The overall validity of lumped element modeling approach was established by characterization of speaker-driven ZNMF actuators. Detailed characterization experiments on three different prototype PDMS diaphragm devices were performed to validate the individual component models and the overall behavior of the actuator. The model predicted the output velocity of several actuator configurations with maximum error of 10 %.

The validated model was then used to investigate several design trends and tradeoffs impacting the actuator performance. These tradeoffs can provide a first level design tool to achieve target actuator specifications without performing a full-blown constrained optimization. Based on the model, a complete constrained optimization for three different objective functions was also performed. One optimized actuator was built and characterized. It was observed that the optimized device generated 50 % higher output velocity as compared to the baseline actuator.

Thus the overall objective of the work—to model, validate and optimize low-cost, compact, low power electrodynamic ZNMF actuators—was reached. The optimized electrodynamic actuator had total volume of 15 cm³, total mass of 90 g, maximum input power consumption of 900 mW and generated a maximum output velocity of about 35 m/s.

6.2 Suggested Future Work

There are several different directions that can be pursued in order to improve and extend this work. Firstly, the model and design tradeoffs presented in this work are specific to the actuator topology used. However, the overall approach is generic and can be extended to many different actuator topologies. Some possible actuator configurations may include rectangular or elliptical actuator configurations. Rectangular or elliptical topologies may be able achieve comparable actuator performance for smaller volume as they conform more to the 2D slot configurations. The biggest challenge in this case would be to develop and validate the appropriate models for the mechanical driver.

The mass of electrodynamic actuators is usually more than comparable-sized piezoelectric ZNMF actuators. The biggest contribution towards the mass of the electrodynamic ZNMF actuator is the magnetic assembly. A detailed investigation of the magnetic assembly design particularly the soft magnetic core can provide several ways to reduce the mass.

The other important improvement on this work will be the detailed investigation of scaling these actuators. Some preliminary model-based scaling analysis was presented in [60]. However, the fabrication methodology presented in this work will not be applicable for very small actuators. The most fabrication of the mechanical driver is probably the most restrictive for realizing smaller actuators. Some possible alternative manufacturing techniques for the mechanical driver can include spin-coating of the elastomer material. The magnetic assembly fabrication for smaller size may include polymer or wax bonded hard magnets and electroplated soft magnetic materials. The fabrication of solenoidal coils will also present significant challenges at smaller size. Ribbon conductors may be used for very small gaps. Electroplating coils in preformed molds may be another possible option. However, beyond a certain size, conventional fabrication methods will be no longer applicable and the use of some surface and

bulk micromachining techniques using for the fabrication of MEMS (MicroElectroMechanicalSystems) will be necessary. These techniques can provide tremendous flexibility in the manufacturing and possible geometries of small electrodynamic ZNMF actuators.

Finally, one of the most relevant extensions of this work will include the characterization of fluidic impact of these actuators in actual flow conditions and identifying the key actuator requirements. This synergy between in actuator design and application requirements will be significant step towards taking these actuators from bench-top laboratory setting to real world application.

APPENDIX A MAGNETIC CIRCUIT MODEL

The 1-D circuit approach was used in Section 3.3.1 to model the magnetic assembly and predict the magnetic flux density in the air gap of the magnetic assembly. The inherent assumptions in this approach are that all the flux is flowing in the closed path defined by the magnetic circuit. The hard magnet acts as the “source” of the magnetic flux. Each of the components of the magnetic circuit has “reluctance” associated with it. The reluctance is based on the geometry and the material properties of the component and is a measure of the resistance the component offers to the flow the magnetic flux.

The magnetic assembly and the 1-D circuit model are shown in Figure A-1.

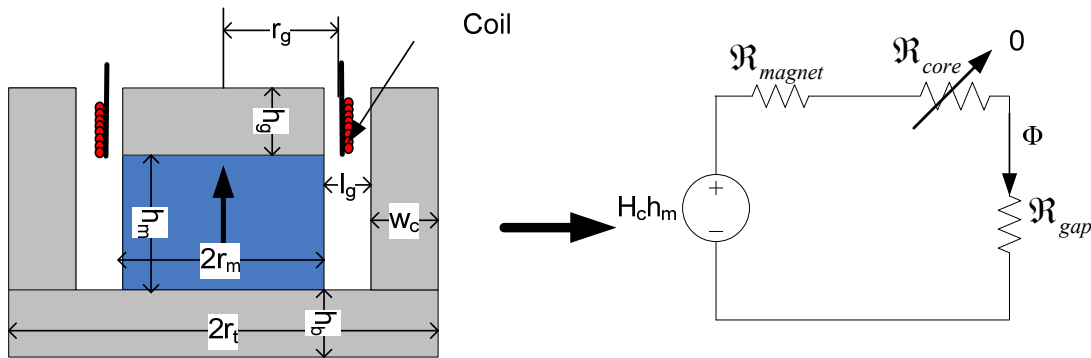


Figure A-1. Magnetic assembly and the 1-D circuit model

The reluctances of the magnet and air gap were detailed in (3.24) and (3.26) respectively. The reluctance of the core was divided into three parts – top, bottom and annular (3.27)-(3.29). The details of the core reluctance calculation are now detailed. The magnetic flux distribution in the magnetic assembly is shown in Figure A-2. It can be seen that the magnetic flux turns around the corner in the soft magnetic pieces. Thus to define the reluctance of the core pieces, certain assumptions are required.

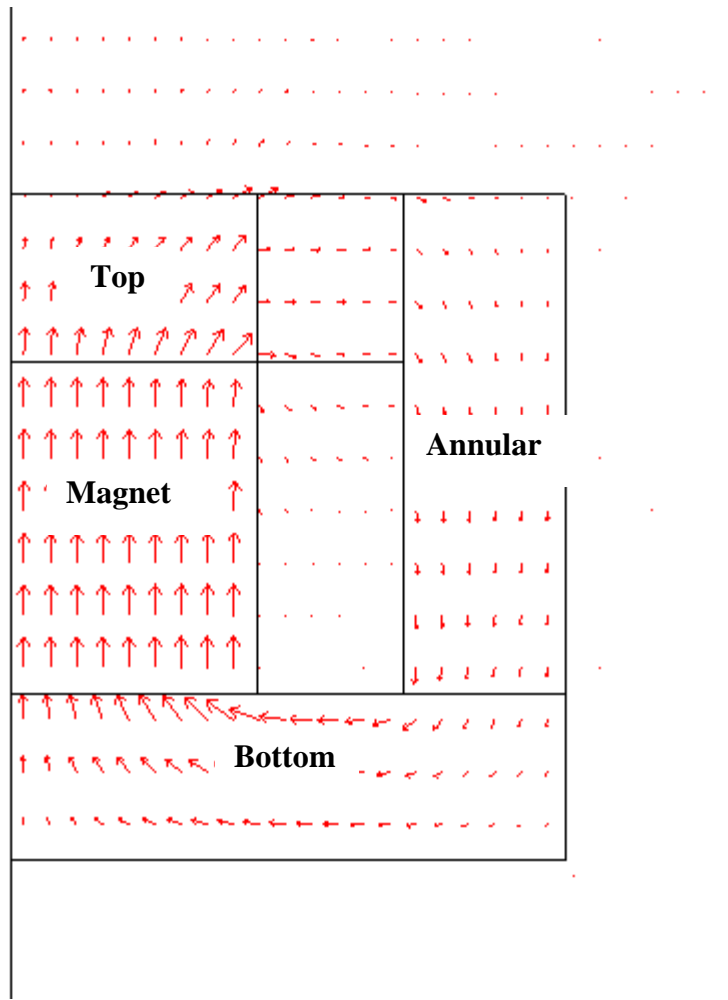


Figure A-2. Arrow plot of magnetic flux density in the magnetic assembly

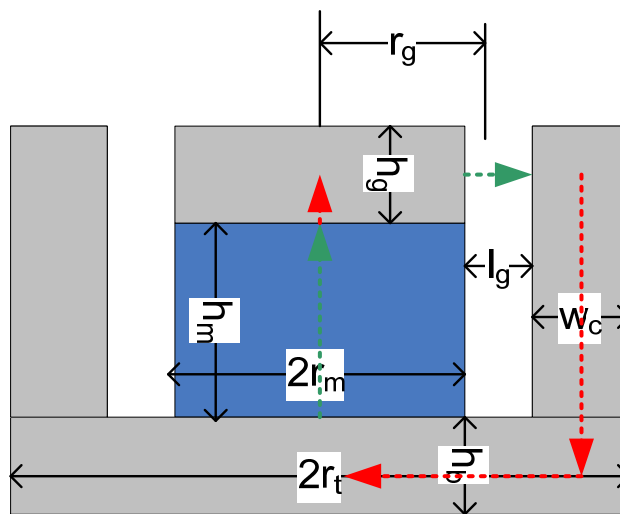


Figure A-3. Reluctance components of the magnetic assembly

Figure A-3 shows the reluctance components of the magnetic path. The green arrows indicate the reluctances of the magnet and the air gap discussed in Chapter 3. The red arrows represent the “average” flux path in the soft magnetic core and are used to define the reluctances of the top, bottom and the annular piece of the core.

It was observed that the EFI 50 nickel-iron alloy used for the soft magnetic core had lower relative permeability than the 100,000 specified in the datasheet. Machining of this material and lack of high temperature anneal after machining resulted in relative permeability of about 100. However even with this lower permeability, the core reluctance is still much smaller than the air gap and the magnet reluctance and the average flux density in the air gap is nearly the same. The core reluctance is thus ignored in the calculations. This can be justified by looking at the relative magnitudes of the reluctances of the core, the air gap and the magnet. Figure A-4 shows the magnitudes of reluctances for the magnet, core and the air gap for various values of the air gap. The magnet and the core reluctance are independent of the air gap length. It can be seen that even for very small air gaps ($\sim 100 - 200 \mu\text{m}$) the air gap reluctance is the same order of magnitude as the core reluctance. However, due to manufacturing constraints the gaps considered will be at least a few millimeters and at these values of gap, the air gap reluctance is nearly 100 times the core reluctance. Thus it is justified to ignore the core reluctance in the magnetic flux density calculations.

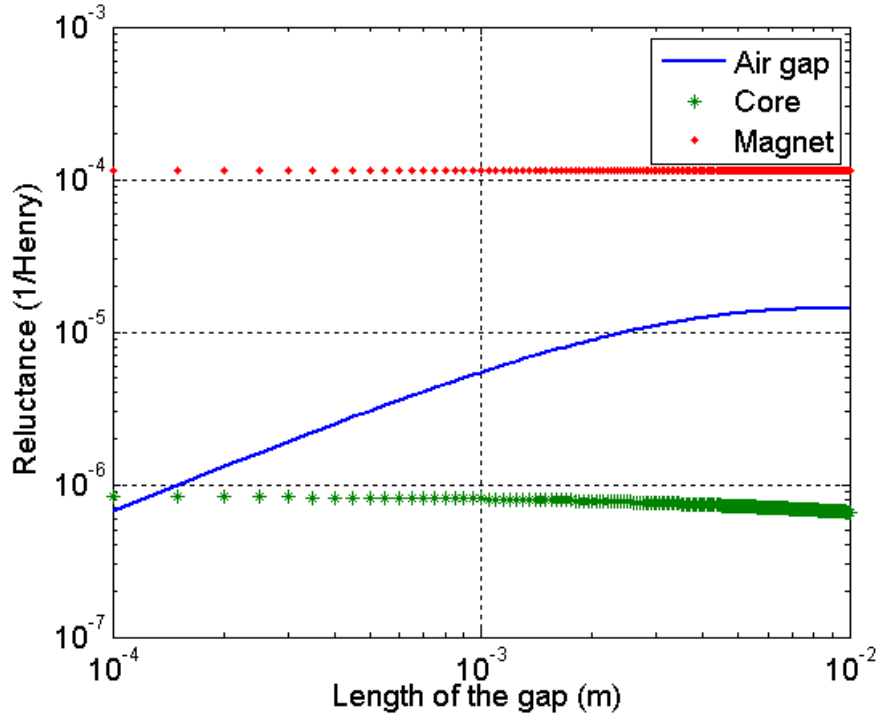


Figure A-4. Relative values of the reluctances of the magnet, core and air gap

A.1 Non-idealities in the Soft Magnet

The magnetic flux density (B) created in a soft magnetic material is directly proportional to the external applied field (H) and the relative permeability (μ_{core}) as shown by Figure A-1. At some applied field, however, all of the domains in the soft magnetic material are aligned to the external magnetic field, and any increase in the external field does not lead to an increase in the magnetic flux density (Figure A-5). This maximum magnetic flux density achievable in the soft magnetic material is called the saturation magnetic flux density B_s . The saturation flux density for EFI50 is specified to be 1.45 T [40]. It is always advisable to avoid saturation in the soft magnetic core in order to reduce losses, non-linearities etc.

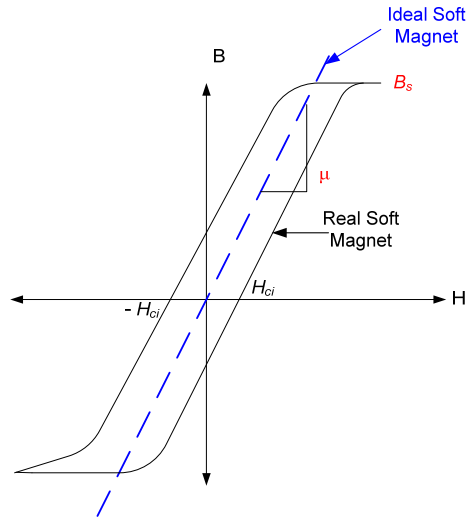


Figure A-5. B-H curve for an ideal and typical soft magnetic material

In the magnetic assembly chosen for this design, the corners where the flux lines have to turn sharply are most susceptible to high flux densities and hence saturation of the soft magnetic core.

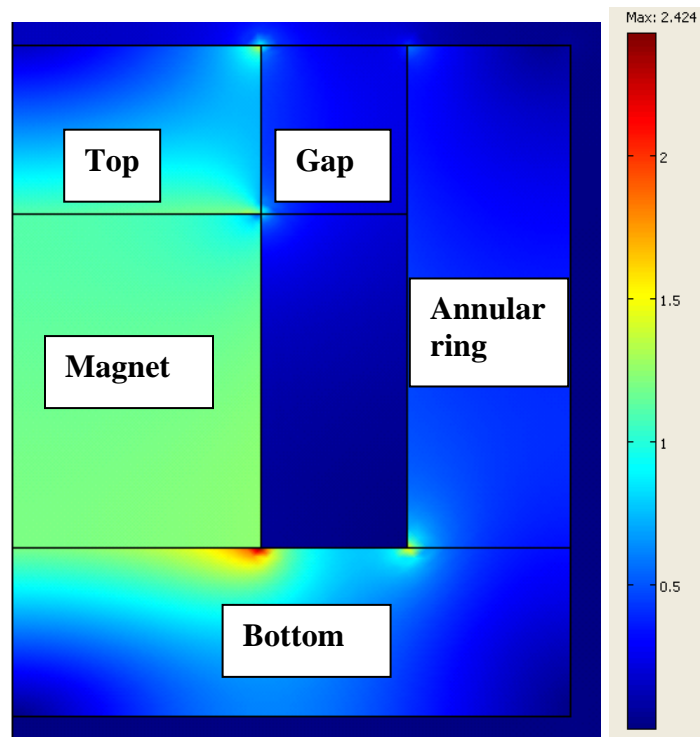


Figure A-6. Results from the COMSOL model – total magnetic flux density (Tesla)

Figure A-6 shows the total magnetic flux density (in Tesla) in the magnetic assembly. It can be seen that at one of the corners the magnetic flux density is high and can lead to magnetic saturation. If the thickness of the magnetic core material is chosen to be very small, the saturation problem will be more severe. In this case the thickness of the soft magnetic core (the thickness of top and bottom pieces and the thickness of the annular ring) is set to be 3.2 mm. Thicker core pieces will ensure no saturation, however the overall weight of the magnetic assembly will increase. The average magnetic flux density in the magnetic assembly is calculated to be 1.32 T.

A.2 Magnetic Assembly for the Optimized Actuator

The dimensions of the magnetic assembly for the optimized actuator are tabulated in Table 5-10. COMSOL Multiphysics was also used to verify the magnetic flux density in the air gap and ensure that the soft magnetic core does not have saturation. Figure A-7 shows the radial magnetic flux density in the magnetic assembly. The average radial magnetic flux density in the air gap was calculated to be 0.26 T. The 1-D magnetic circuit model predicted the flux density in the air gap to be 0.24 T.

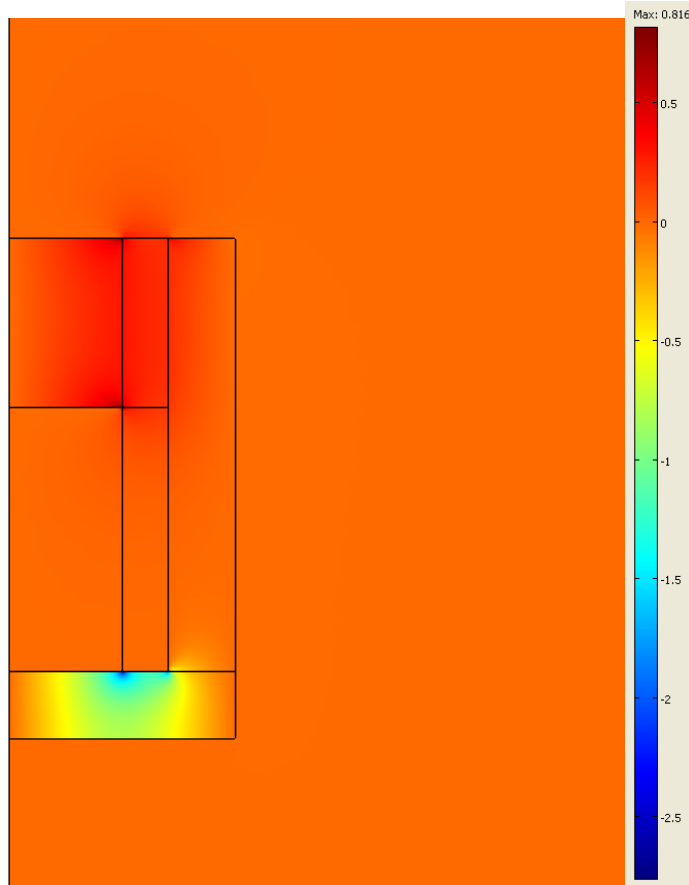


Figure A-7. Radial magnetic flux density in the magnetic assembly of the optimized actuator

The total magnetic flux density in magnetic assembly is shown in Figure A-8. It can be seen that near the corners of the total flux density is high. However, the average flux density in the soft magnetic core is 1.2 T which is lower than the saturation magnetic flux density of 1.45 T.

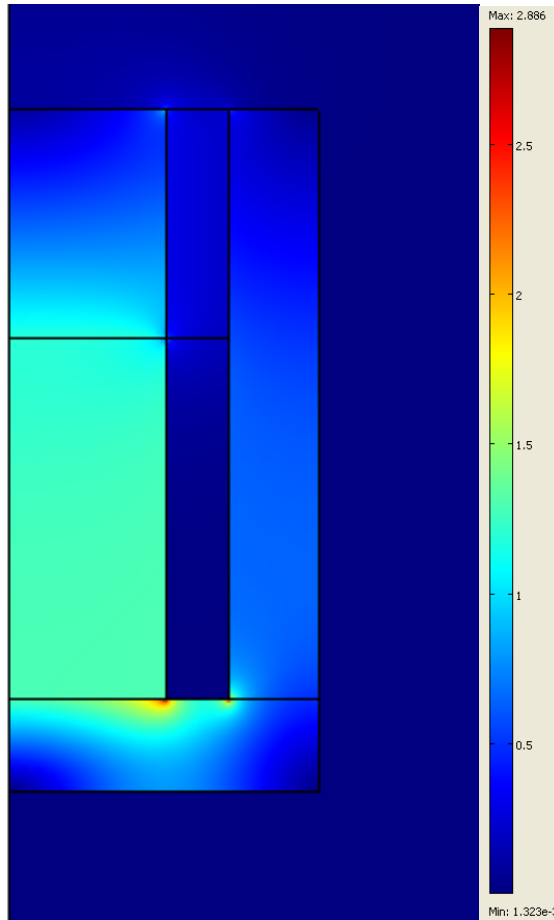


Figure A-8. Total magnetic flux density

A.3 Force Non-linearities

The most generic expression for the Lorentz force on the coil is given by

$$F = \int_V (\vec{J} \times \vec{B}) dV = \int_V J_\phi B_r dV \quad (\text{A.158})$$

where \vec{J} is the current density through the coil and \vec{B} is the magnetic flux density. For the axisymmetric magnetic assembly topology chosen here, the current is in the angular direction (ϕ) and thus only the radial magnetic flux density (B_r) generates a force in the axial direction. The assumption of constant current density in the coil is reasonable particularly for low frequencies. If the radial flux density linking with the coil is also assumed to be constant, the classical Lorentz force equation ($F = BL_{coil}I$) is obtained (section 3.3). However, the radial flux

density is a function of both the axial and radial position. Moreover, when the coil moves during the device operation the flux density linking with the coil changes. This will result in an inherent directional non-linearity in the device operation. Figure A-9 shows the force calculated from COMSOL Multiphysics for various coil positions during the device operation for the optimized actuator. The range of motion chosen here (± 0.3 mm) is the maximum range of motion in actual device. It can be seen that the maximum deviation from the constant force assumption is about 8 %.

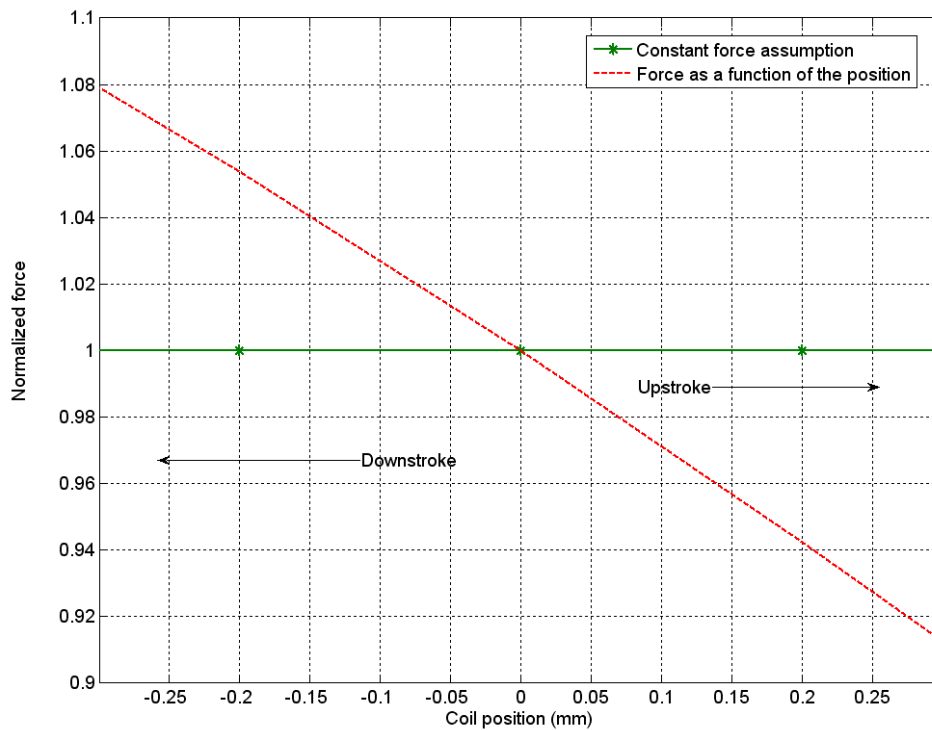


Figure A-9. Non-linearity due to spatial variation of the flux density

APPENDIX B
DERIVATION OF LUMPED MODEL PARAMETERS OF A CLAMPED ANNULAR PLATE

The mechanical driver of the electrodynamic ZNMF actuators consists of rigid center boss of radius b and annular compliant region with outer radius a . The coil of mass M_{coil} is attached to the rigid portion of the driver. The schematic and the material properties of the two regions (Region 1 = rigid central boss, Region 2 = annular compliant region) are shown in Figure B-1. The central boss is assumed to be perfectly rigid and the coil is assumed to add an additional mass. The mechanical driver is thus modeled as an annular plate. The assumptions involved in the model are as follows

- The annular portion has uniform thickness and is isotropic.
- The maximum transverse deflection (w) is small (not more than 30 % of the thickness of the diaphragm i.e. $w(r) \leq 0.3h$). Note that this constraint also depends on the solidity ratio (b/a) [61]. A curve-fit may be used to obtain a solidity ratio dependent constraint on the maximum deflection. The detailed investigation of this dependence is beyond the scope of this work. For moderate solidity ratios considered here (0.5 – 0.8), this assumption seems reasonable.
- All forces are normal to the plane of the diaphragm.
- The diaphragm thickness is small ($h \leq 0.1a$).

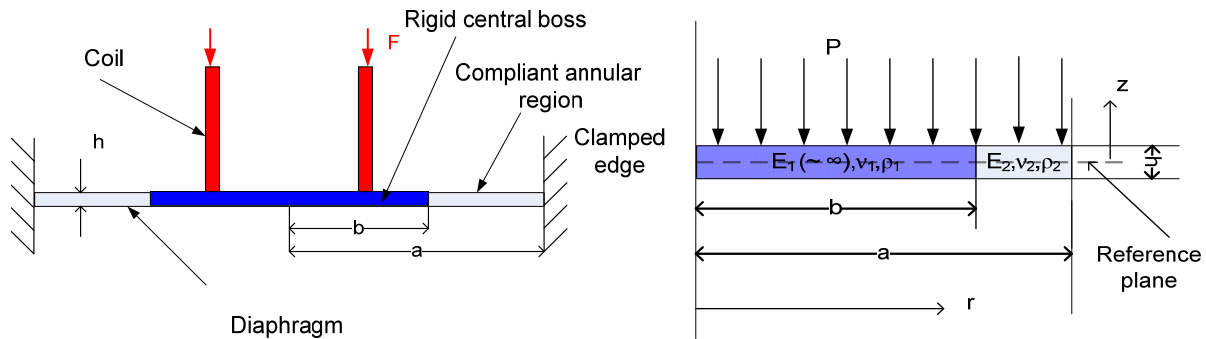


Figure B-1. Schematic for the mechanical driver and the simplified annular plate model

Note that additional constraints to prevent buckling of the annular diaphragm may also be included in the optimization formulation. Based on these assumptions, the transverse displacements in the two regions are defined as

$$\begin{aligned} w(r) &= w_1(r) \text{ for } 0 \leq r < b \\ &= w_2(r) \text{ for } b \leq r \leq a \end{aligned} \quad (\text{B.159})$$

The outer edge $r = a$, is clamped and the boundary conditions can be stated mathematically as

$$w(a) = 0, \quad \left. \frac{dw}{dr} \right|_{r=a} = 0 \quad (\text{B.160})$$

The boundary conditions at the center require finite values of the displacement and slope as given by

$$w(0) < \infty, \quad \left. \frac{dw}{dr} \right|_{r=0} < \infty \quad (\text{B.161})$$

In addition, matching conditions are necessary at the interface between the inner circular portion and the annular outer region at $r = b$. The displacement and slope matching conditions at the interface are given by

$$w_1(b) = w_2(b), \quad \left. \frac{dw_1}{dr} \right|_{r=b} = \left. \frac{dw_2}{dr} \right|_{r=b} \quad (\text{B.162})$$

From these boundary conditions and matching conditions, the displacement of the diaphragm is calculated under a uniform pressure load p [62] as

$$w(0) = w(b) = \frac{3p(1-\nu_2^2)a^4}{16E_2h^3} \left[1 + 4\left(\frac{b}{a}\right)^2 \ln\left(\frac{b}{a}\right) - \left(\frac{b}{a}\right)^4 \right] \quad (\text{B.163})$$

and

$$w(r)|_{b < r < a} = \frac{3p(1-\nu_2^2)}{16E_2h^3} \left[1 + 4\left(\frac{b}{a}\right)^2 \ln\left(\frac{r}{a}\right) - 2\left(\frac{r}{a}\right)^2 + 2\left(\frac{b}{a}\right)^2 - 2\frac{b^2r^2}{a^4} + \left(\frac{r}{a}\right)^4 \right]. \quad (\text{B.164})$$

The typical displacement profile for 10 Pa uniform pressure load is shown in Figure B-2.

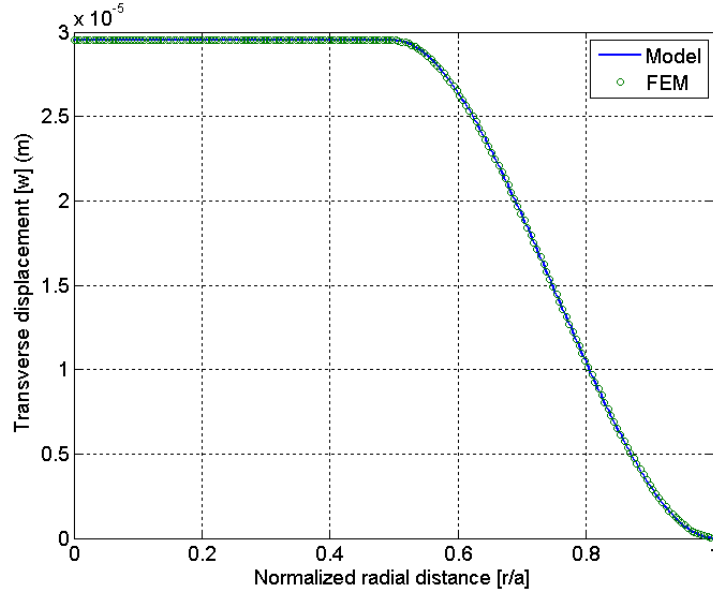


Figure B-2. Transverse displacement – Model & FEM results ($b/a = 0.5$, $h/a = 0.08$, $a = 12.7 \times 10^{-3}$, $E_2 = 360$ kPa, $\nu_2 = 0.33$).

The acoustic compliance accounts for the change in volume (∇) for a unit of applied pressure, when the electrical voltage to the coil is zero ($V = 0$). The change in volume is calculated by integrating the displacement of the diaphragm over the entire diaphragm. Thus the lumped acoustic compliance C_{aD} is given by

$$C_{aD} = \frac{|\nabla|}{p} \Big|_{V=0} = \frac{\int_0^a w(r) 2\pi r dr}{p} = \frac{\int_0^b w_1(r) 2\pi r dr + \int_b^a w_2(r) 2\pi r dr}{p}. \quad (\text{B.165})$$

Using the displacement profile described previously, the acoustic compliance is given by

$$C_{aD} = \frac{\pi(1-\nu_2^2)a^6}{16E_2h^3} \left[1 - 3\left(\frac{b}{a}\right)^2 + 3\left(\frac{b}{a}\right)^4 - \left(\frac{b}{a}\right)^6 \right]. \quad (\text{B.166})$$

The effective mass of the diaphragm is calculated by computing the total kinetic energy of the diaphragm and lumping it to the center velocity. Harmonic motion of the diaphragm is assumed. Since the coil is attached to the central boss of the diaphragm assembly, it also contributes to the total mass of the diaphragm. The acoustic mass of the diaphragm is given by

[42]

$$M_{ad} = 2\pi \int_0^a \rho h \left(\frac{w(r)}{\nabla} \right)^2 r dr + \frac{M_{coil}}{S^2} \quad (\text{B.167})$$

where S is the effective area of the diaphragm defined in Chapter 3. This can be simplified to

$$M_{ad} = \underbrace{2\pi\rho_1 h \int_0^b \left(\frac{w_1(r)}{\nabla} \right)^2 r dr}_{M_{rigid}} + \underbrace{2\pi\rho_2 h \int_b^a \left(\frac{w_2(r)}{\nabla} \right)^2 r dr}_{M_{annular}} + \frac{M_{coil}}{S^2}, \quad (\text{B.168})$$

where M_{rigid} and $M_{annular}$ are the contributions of the rigid central boss and the annular compliant region respectively. These are given by

$$M_{rigid} = \frac{9b^2 h \rho_1 \left(1 - 8 \left(\frac{b}{a} \right)^6 \ln \left(\frac{b}{a} \right) + 16 \left(\frac{b}{a} \right)^4 \left(\ln \left(\frac{b}{a} \right) \right)^2 + \left(\frac{b}{a} \right)^8 + 8 \left(\frac{b}{a} \right)^2 \ln \left(\frac{b}{a} \right) - 2 \left(\frac{b}{a} \right)^4 \right)}{a^4 \left(-20 \left(\frac{b}{a} \right)^6 + 15 \left(\frac{b}{a} \right)^8 - 6 \left(\frac{b}{a} \right)^{10} + \left(\frac{b}{a} \right)^2 + 1 - 6 \left(\frac{b}{a} \right)^2 + 15 \left(\frac{b}{a} \right)^4 \right)} \quad (\text{B.169})$$

and

$$M_{annular} = \frac{\rho_2 h}{5a^2} \frac{120 \left(\frac{b}{a} \right)^4 \ln \left(\frac{b}{a} \right) \left[3 \left(\frac{b}{a} \right)^2 + 2 \left(\frac{b}{a} \right)^4 - 3 - 6 \left(\frac{b}{a} \right)^2 \ln \left(\frac{b}{a} \right) \right]}{-20 \left(\frac{b}{a} \right)^6 + 15 \left(\frac{b}{a} \right)^8 - 6 \left(\frac{b}{a} \right)^{10} + \left(\frac{b}{a} \right)^2 + 1 - 6 \left(\frac{b}{a} \right)^2 + 15 \left(\frac{b}{a} \right)^4} \quad (\text{B.170})$$

$$+ \frac{\left(\frac{b}{a} \right)^2 \left[-24 \left(\frac{b}{a} \right)^8 - 25 \left(\frac{b}{a} \right)^6 - 110 + 240 \left(\frac{b}{a} \right)^2 - 90 \left(\frac{b}{a} \right)^4 \right] + 9}{-20 \left(\frac{b}{a} \right)^6 + 15 \left(\frac{b}{a} \right)^8 - 6 \left(\frac{b}{a} \right)^{10} + \left(\frac{b}{a} \right)^2 + 1 - 6 \left(\frac{b}{a} \right)^2 + 15 \left(\frac{b}{a} \right)^4}$$

APPENDIX C
OPTIMIZATION DETAILS

Chapter 5 detailed the optimization problem for the magnetic assembly as well as the overall electrodynamic ZNMF actuators.

The optimization of magnetic assembly for maximum blocked force was presented in section 5.3.1. The optimized magnetic assembly designs for the mass constraint of 150 g and 120 g are tabulated in Table C-1 and Table C-2 respectively.

Table C-1. Optimized magnetic assembly designs for maximum blocked force for power constraint and mass constraint of 150 g

r_m (mm)	h_m (mm)	h_g (mm)	l_g (mm)	<i>AWG</i>	<i>P</i> (W)	F_b (N)	Mass (g)
6	12.7	1.6	1	40	0.1	0.15	65
9.4	12.7	1.6	1.2	34	0.3	0.65	110
9.4	12.7	1.6	1.6	34	0.5	0.9	113
9.4	12.7	2	1.9	34	0.8	1.18	117
9.4	12.7	2.2	2.1	34	1	1.33	120
9.4	12.7	2.7	2.4	34	1.5	1.66	125
9.4	12.7	3.2	2.6	34	2	1.93	130
9.4	12.7	4.5	3.4	34	4	2.74	144
9.4	11.8	5.4	3.9	34	6	3.32	150
9.4	10.3	6.2	4.4	34	8	3.74	150
9.4	8.7	7.9	4.3	34	10	4.05	150

Table C-2. Optimized magnetic assembly designs for maximum blocked force for power constraint and mass constraint of 120 g

r_m (mm)	h_m (mm)	h_g (mm)	l_g (mm)	<i>AWG</i>	<i>P</i> (W)	F_b (N)	Mass (g)
6	12.7	1.6	1	40	0.1	0.15	65
9.4	12.7	1.6	1.2	34	0.3	0.65	110
9.4	12.7	1.6	1.6	34	0.5	0.9	113
9.4	12.7	2	1.9	34	0.8	1.18	117
9.4	12.7	2.2	2.1	34	1	1.33	120
9.4	11.8	2.7	2.4	34	1.5	1.65	120
9.4	11	3.2	2.6	34	2	1.9	120
9.4	8.6	4.5	3.3	34	4	2.6	120
9.4	6.9	6	3.5	34	6	2.98	120
9.4	6.9	6	3.5	34	8	2.98	120

It can be seen that as the mass of the magnetic assembly becomes restrictive, the mass constraint is satisfied by making the magnet smaller.

The optimized designs for the overall electrodynamic ZNMF actuator for maximum integrated velocity over 0 – 300 Hz (objective function 1) for various mass constraints are tabulated in Table C-3.

Table C-3. Optimized designs for objective function 1 with various weight constraints

r_m (mm)	h_m (mm)	h_g (mm)	l_g (mm)	a (mm)	b (mm)	L_C (mm)	AWG (mm)	h	<i>Mass (g)</i>	<i>Average velocity (m/s)</i>
5.5	12.7	8.1	2.2	12.7	9.7	3	34	1	90	13.6
5.5	9.9	7.7	2.2	12.7	9.6	3	34	1	80	17.9
5.5	7.2	7.4	2.2	12.7	9.5	3	34	1	70	18.7
5.5	4.9	6.8	2.2	12.7	9.3	3	34	1	60	18.6
5.5	4.5	4.2	2.2	12.7	9.3	3	34	1	50	18.1
4.9	4	3.4	2	12.7	9.3	3	34	1	40	16.7

It can be seen that as in the case of the optimization of the magnetic assembly alone, the mass constraint is met by making the magnet smaller even for the optimized designs of the overall actuator.

LIST OF REFERENCES

- [1] A. Glezer and M. Amitay, "Synthetic Jets," *Annual Reviews in Fluid Mechanics*, vol. 34, no. 1, pp. 503-529, 2002.
- [2] B. L. Smith and A. Glezer, "The Formation and Evolution of Synthetic Jets," *Physics of Fluids*, vol. 10, no. 9, pp. 2281-2297, 1998.
- [3] D. C. McCormick, "Boundary Layer Separation Control with Directed Synthetic Jets " in *38th Aerospace Sciences Meeting and Exhibit Reno,NV: AIAA*, 2000.
- [4] W. Yong, Y. Guang, Y. Yong-Kyu, M. G. Allen, and S. A. Bidstrup, "Active Cooling Substrates for Thermal Management of Microelectronics," *IEEE Transactions on Components and Packaging Technologies*, vol. 28, no. 3, pp. 477- 483, 2005.
- [5] O. Cugat, J. Delamare, and G. Reyne, "Magnetic micro-actuators and systems (MAGMAS)," *IEEE Transactions on Magnetics*, vol. 39, no. 6, pp. 3607- 3612, Nov. 2003.
- [6] J. S. Agashe, M. Sheplak, D. P. Arnold, and L. N. Cattafesta, "MEMS-based Actuators for Flow-Control Applications," in *IUTAM Symposium on Flow Control and MEMS*, J. F. Morrison, Ed.: Springer, September 2006, pp. 25-32.
- [7] F. V. Hunt, *Electroacoustics: The Analysis of Transduction, and Its Historical Background*. New York: Acoustical Society of America, 1982.
- [8] J. E. Huber, N. A. Fleck, and M. F. Ashby, "The Selection of Mechanical Actuators Based on Performance Indices," *Proceedings: Mathematical, Physical and Engineering Sciences*, vol. 453, no. 1965, pp. 2185-2205, 1997.
- [9] I. J. Busch-Vishniac, "The case for magnetically driven microactuators," *The Journal of the Acoustical Society of America*, vol. 92, no. 4, pp. 2353-2354, 1992.
- [10] W. Trimmer and R. Jebens, "Actuators for micro robots," in *IEEE Conference on Robotics and Automation* Scottsdale AZ, USA, 1989, pp. 1547-1552.
- [11] O. Cugat, J. Delamare, and G. Reyne, "Magnetic micro-actuators and systems (MAGMAS)," *IEEE Transactions on Magnetics*, vol. 39, no. 6, pp. 3607-3612, Nov. 2003.
- [12] M. Rossi, *Acoustics and Electroacoustics*. Norwood, MA: Artech House, Inc., 1988.
- [13] S. D. Senturia, *Microsystem Design*. Boston: Kluwer Academic Publishing, 2001.
- [14] Q. Gallas, R. Holman, T. Nishida, B. Carroll, M. Sheplak, and L. Cattafesta, "Lumped Element Modeling of Piezoelectric-driven Synthetic Jet Actuators," *AIAA Journal*, vol. 41, no. 2, pp. 240-247, 2003.

- [15] L. D. Kral, J. F. Donovan, A. B. Cain, and A. W. Cary, "Numerical Simulation of Synthetic Jet Actuators," in *AIAA Shear Flow Control Conference SnowMass Village CO*, 1997, pp. 1824-1838.
- [16] D. P. Rizzetta, M. R. Visbal, and M. J. Stanek, "Numerical Investigation of Synthetic Jet Flow," *AIAA Journal*, vol. 37, no. 8, pp. 919–927, 1999.
- [17] Y. Utturkar, R. Mittal, P. Rampungoon, and L. Cattafesta, "Sensitivity of Synthetic Jets to the Design of the Jet Cavity," in *AIAA Aerospace Sciences Meeting and Exhibit*, Reno NV, 2002, pp. 124-128.
- [18] H. H. Woodson and J. R. Melcher, *Electromechanical Dynamics*. New York: John Wiley, 1968.
- [19] O. B. Wilson, C. Naval Sea Systems, C. Naval Electronic Systems, and S. United, *Introduction to Theory and Design of Sonar Transducers*: Peninsula Publishing, 1988.
- [20] R. K. Wangsness, *Electromagnetic Fields*, 2nd ed. New York: Wiley, 1986.
- [21] W. J. Hayt, *Engineering Electromagnetics*, 4th ed. New York: Macgraw-Hill, 1981.
- [22] P. Campbell, *Permanent Magnet Materials and Their Application*. Cambridge: Cambridge University Press, 1994.
- [23] R. M. Bozorth, *Ferromagnetism*. Piscataway, NJ: IEEE Press, 1993.
- [24] E. P. Furlani, *Permanent Magnet and Electromechanical Devices: Materials, Analysis, and Applications*: Academic Press, 2001.
- [25] J. Judy, "Microelectromechanical systems /(MEMS)/: fabrication, design and applications," *Smart Materials and Structures*, vol. 10, no. 6, pp. 1115-1134, 2001.
- [26] D. J. Coe, M. G. Allen, B. L. Smith, and A. Glezer, "Addressable Micromachined Jet Arrays," in *The 8th International Conference on Solid-State Sensors and Actuators, 1995 and Eurosensors IX. Transducers '95.*, 1995, pp. 329-332.
- [27] K. Mossi and R. Bryant, "Piezoelectric Actuators for Synthetic Jet Applications," *Materials Research Society*, vol. 785, no. 1, pp. 407-414, 2004.
- [28] B. Parviz, K. Najafi, M. Muller, L. Bernal, and P. Washabaugh, "Electrostatically driven synthetic microjet arrays as a propulsion method for micro flight," *Microsystem Technologies*, vol. 11, no. 11, pp. 1214-1222, 2005.
- [29] Y. Liang, M. Taya, and Y. Kuga, "Design of membrane actuators based on ferromagnetic shape memory alloy composite for the synthetic jet actuator," *Sensors and Actuator A*, vol. 125, no. 2, pp. 512 - 518, 2004.

- [30] Y. Liang, Y. Kuga, and M. Taya, "Design of synthetic jet actuator based on FSMA composite," *Smart Structures and Materials 2005: Industrial and Commercial Applications of Smart Structures Technologies*, vol. 5762, no. 1, pp. 179-186, 2005.
- [31] S. Lee, K. J. Kim, and H. C. Park, "Modeling of an IPMC Actuator-driven Zero-Net-Mass-Flux Pump for Flow Control," *Journal of Intelligent Material Systems and Structures*, vol. 17, no. 6, pp. 533-541, 2006.
- [32] M. Gordon, J. E. Cater, and J. Soria, "Investigation of the mean passive scalar field in zero-net-mass-flux jets in cross-flow using planar-laser-induced fluorescence," *Physics of Fluids*, vol. 16, no. 3, pp. 794-808, 2004.
- [33] S. J. Campbell, Jr., W. Z. Black, A. Glezer, and J. G. Hartley, "Thermal management of a laptop computer with synthetic air microjets," in *Thermal and Thermomechanical Phenomena in Electronic Systems, 1998. ITherm '98. The Sixth Intersociety Conference on*, 1998, pp. 43-50.
- [34] G. Hong, "Effectiveness of micro synthetic jet actuator enhanced by flow instability in controlling laminar separation caused by adverse pressure gradient," *Sensors and Actuators A: Physical*, vol. 132, no. 2, pp. 607-615, 2006.
- [35] C. Lee, G. Hong, Q. P. Ha, and S. G. Mallinson, "A piezoelectrically actuated micro synthetic jet for active flow control," *Sensors & Actuators: A. Physical*, vol. 108, no. 1-3, pp. 168-174, 2003.
- [36] S. Zhong, M. Jabbal, H. Tang, L. Garcillan, F. Guo, N. Wood, and C. Warsop, "Towards the Design of Synthetic-jet Actuators for Full-scale Flight Conditions," *Flow, Turbulence and Combustion*, vol. 78, no. 3, pp. 283-307, 2007.
- [37] W. J. Crowther, L. T. Gomes, and S. Daley, "An evaluation of the mass and power scaling of synthetic jet actuator flow control technology for civil transport aircraft applications," *Proceedings of the Institution of Mechanical Engineers, Part I: Journal of Systems and Control Engineering*, vol. 222, no. 5, pp. 357-372, 2008.
- [38] Y. Tian, Q. Song, and L. Cattafesta, "Adaptive Feedback Control of Flow Separation," *AIAA Paper*, vol. 3016, no. 2006.
- [39] F. T. Ulaby, *Fundamentals of Applied Electromagnetics*, 5th ed. Upper Saddle River, NJ: Prentice-Hall, 1999.
- [40] E. F. Inc., "Soft Magnetic Alloys," <http://www.edfagan.com/2006/products/2/>, 21 August 2008.
- [41] W.C.Young and R. G. Budynas, *Roark's Formulas for Stress and Strain*, 7th ed. New York: McGraw-Hill, 2002.

- [42] S. A. N. Prasad, Q. Gallas, S. Horowitz, B. Homeijer, B. V. Sankar, L. N. Cattafesta, and M. Sheplak, "Analytical Electroacoustic Model of a Piezoelectric Composite Circular Plate," *AIAA Journal*, vol. 44, no. 10, p. 2311, 2006.
- [43] D. T. Blackstock, *Fundamentals of Physical Acoustics*. New York: John Wiley & Sons Inc., 2000.
- [44] F. M. White, *Fluid Mechanics*. New York: McGraw-Hill, 1999.
- [45] Q. Gallas, "On The Modeling And Design Of Zero-Net Mass Flux Actuators," in *Department of Mechanical and Aerospace Engineering Gainesville FL: University of Florida*, May 2005.
- [46] E. G. Williams, *Fourier acoustics*: Academic Press.
- [47] C. Inc., "Speaker Part No. GA0701," <http://www.cui.com/pdf/files/GA0701.pdf>, 12 December, 2008.
- [48] A. Hadjian and C. Norwalk, "An Extension of the Log-decement Method," *Seismic Engineering*, no. 1987.
- [49] A. A. Hassan and D. B. Domzalski, "Jet Actuators for Aerodynamic Surfaces," USA: The Boeing Company, 2002.
- [50] H. H. Bruun, *Hot-wire anemometry- Principles and signal analysis*. New York, NY: Oxford University Press, 1995.
- [51] R. L. Panton, *Incompressible Flow*, 1996.
- [52] J. S. Bendat and A. G. Piersol, *Random Data Analysis and Measurement Procedures*. New York, NY: John Wiley & Sons Inc., 2000.
- [53] "MWS Wire Industries," <http://www.mwswire.com/bond1.htm>, 21 December, 2008.
- [54] "Sylgard 184 Silicone Elastomer Kit," <http://www2.dowcorning.com/DataFiles/090007c8801e1054.pdf>, 21 December, 2008.
- [55] D. Armani, C. Liu, and N. Aluru, "Re-configurable fluid circuits by PDMS elastomer micromachining," in *Micro Electro Mechanical Systems, 1999. MEMS '99. Twelfth IEEE International Conference on*, 1999, pp. 222-227.
- [56] K. K. Phani, S. K. Niyogi, A. K. Maitra, and M. Roychaudhury, "Strength and elastic modulus of a porous brittle solid: An acousto-ultrasonic study," *Journal of Materials Science*, vol. 21, no. 12, pp. 4335-4341, 1986.
- [57] M. Papila, M. Sheplak, and L. Cattafesta, "Optimization of clamped circular piezoelectric composite actuators," *Sensors & Actuators: A. Physical*, no. 2008.

- [58] Q. Gallas, G. Wang, M. Papila, M. Sheplak, L. Cattafesta, M. Florida Univ Gainesville, and E. Aerospace, "Optimization of Synthetic Jet Actuators," in *41st Aerospace Sciences Meeting & Exhibit* Reno, NV, 2003.
- [59] PowerStream, "American Wire Gauge Table," http://www.powerstream.com/Wire_Size.htm, 21 August, 2008.
- [60] J. S. Agashe, Sheplak, M., Arnold, D. P., and Cattafesta, L. N., "MEMS-based actuators for flow-control applications," in *IUTAM Symposium on Flow Control and MEMS*, J. F. Morrison, Ed.: Springer, pp. 25-32.
- [61] Y. H. Su, K. S. Chen, D. C. Roberts, and S. M. Spearing, "Large deflection analysis of a pre-stressed annular plate with a rigid boss under axisymmetric loading," *Journal of Micromechanics and Microengineering*, vol. 11, no. 6, pp. 645-653, 2001.
- [62] R. J. Roark, "Formulas for stress and strain," *New York: McGraw-Hill, 1965, 4th ed.*, no. 1965.

BIOGRAPHICAL SKETCH

Ms. Janhavi Agashe received her bachelor's degree in electrical engineering from Veermata Jijabai Technological Institute in August 2000. She got her Master of Science in electrical engineering from Iowa State University in August 2003. She started the Ph.D. program in the Department of Electrical and Computer Engineering at the University of Florida in August 2004. She received her Ph.D. from the University of Florida in the spring of 2009